2013-12-13

A Study of Internal Solitary Waves in Satellite Images of the Mid-Atlantic Bight

Jingshuang Xue
University of Miami, jingshuangxue@gmail.com

UNIVERSITY OF MIAMI

A STUDY OF INTERNAL SOLITARY WAVES IN SATELLITE IMAGES OF THE MID-ATLANTIC BIGHT

By

Jingshuang Xue

A DISSERTATION

Submitted to the Faculty
of the University of Miami
in partial fulfillment of the requirements for
the degree of Doctor of Philosophy

Coral Gables, Florida

December 2013

UNIVERSITY OF MIAMI

A dissertation submitted in partial fulfillment of
the requirements for the degree of
Doctor of Philosophy

A STUDY OF INTERNAL SOLITARY WAVES IN SATELLITE IMAGES OF THE MID-ATLANTIC BIGHT

Jingshuang Xue

Approved:

_____
Hans C. Graber, Sc.D.
Professor of Applied Marine Physics

_____
Michael G. Brown, Ph.D.
Professor of Applied Marine Physics

_____
Roland Romeiser, Dr.rer.nat.
Associate Professor of
Applied Marine Physic

_____
M. Brian Blake, Ph.D.
Dean of the Graduate School

_____
Karl R. Helfrich, Ph.D.
Senior Scientist of Physical Oceanography
Woods Hole Oceanographic Institution
Woods Hole, Massachusetts

XUE, JINGSHUANG (Ph.D., Applied Marine Physics)

A Study of Internal Solitary Waves in Satellite Images of the Mid-Atlantic Bight (December 2013)

Abstract of a dissertation at the University of Miami.

Dissertation supervised by Professor Hans C. Graber.
No. of pages in text. (111)

Satellite imagery has been widely used to study internal solitary wave (ISW) generation mechanisms, evolution, and properties. The Nonlinear Internal Wave Initiative/Shallow Water 2006 (SW06) experiment in the Mid-Atlantic Bight (MAB) provided a unique dataset to study the vertical structure from their surface manifestation in the images, which can improve our understanding of ISW evolution, energy dissipation, and mixing processes. This thesis has two parts. First, the applicability of various weakly nonlinear theories including the Korteweg-de Vries (KdV), Intermediate Long Wave (ILW), Benjamin-Ono (BO), and higher-order KdV models is tested to describe large amplitude ISWs in the MAB. Based on a simple theoretical radar imaging model, a method is developed to estimate large ISW amplitudes from distances between the positive and negative peaks of ISW signatures in radar images and a selection rule from the two possible amplitude solutions is proposed. Two groups of ISWs with large amplitudes, determined from the temperature records from nearby moorings, are observed in a RADARSAT-1 synthetic-aperture-radar (SAR) image and in marine X-band radar data collected during the experiment. The proposed method is validated by using the ISW signatures taken from these two cases. The estimated amplitudes using the

higher-order KdV model are found to agree well with those determined from the moorings. All other models give amplitude estimates that are far too small. Second, the characteristics of the observed interaction patterns in the satellite images such as wave phase shifts and amplitude changes are analyzed. Comparing these patterns with existing analytical and numerical models for a two-soliton interaction, these patterns are categorized into four different types: Mach interaction; regular interaction with prominent positive phase shifts and an amplitude decrease in the interaction zone; regular interaction with prominent negative phase shifts and an amplitude increase in the interaction zone; and wave interactions without phase shifts. One important result from this study is that the patterns alone can be used to deduce how the amplitude changes in the potentially hazardous interaction zone, which demonstrates that high-resolution satellite images can provide a useful and efficient means of studying internal wave interaction.

ACKNOWLEDGMENT

This work would not have been possible without the support and encouragement of my advisor, Dr. Hans C. Graber. He gave me the freedom to do the research I am interested in, cheered me up whenever I got frustrated and struggled, and bolstered my confidence and belief in my abilities. I am also very grateful for the continuous guidance of Dr. Roland Romeiser. He was always there when I needed scientific discussion and always come up with valuable suggestions. I learned a lot from his rigorous attitude and passion for scientific research. I thank my committee member Drs. Karl Helfrich and Michael Brown for their patience and guidance when I encountered difficulties related to my research.

I wish to thank Neil Williams, Mike Caruso, and Rafael Ramos for their help in data preparation, technical support, and guidance when I started my research. I also would like to acknowledge Bjorn Lund, the co-author of my two publications, for his friendship and helpful contribution to these papers. I am also grateful to the AMP division's faculty and staff for an excellent work environment.

I am having a great time at RSMAS and feel very lucky to have had the opportunity to pursue my Ph.D. here and to be a member of the RSMAS community. I want to thank all my friends at RSMAS. Without them, my life in Miami would not have been so nice and fun. Finally I wish to thank my family for their continuous love, support, and encouragement.

This work is supported by ONR under Grant N000140510758. Thanks go to Dr. J. Lynch and his team in Woods Hole Oceanographic Institution for providing in situ data used for comparison with the satellite and marine radar measurements.

TABLE OF CONTENTS

LIST OF FIGURES

LIST OF TABLES

CHAPTER 1 INTRODUCTION

This chapter gives definitions and importance of oceanic internal solitary waves (ISWs) in section 1.1. Background information of remote sensing of ISWs on different platforms, including synthetic aperture radar (SAR), marine X-band radar, and optical images, and ISW signature interpretation is presented in section 1.2. Thesis objectives and organization are provided in section 1.3.

1.1 Oceanic internal solitary waves

The most commonly known waves in the ocean are surface waves, which are traveling between the interface of air and water and the restoring force is gravitational force. Oceanic internal waves, as their name implies, travels interior of the ocean. These internal waves can have much larger amplitudes and propagate at a much lower speed than surface waves, as a result of a weaker gravitational restoring force from much less density difference between the upper and lower water layers than between air and water.

Tidally induced internal waves are generated in a stratified ocean, by the interaction of a tidal flow with irregular topography such as sill, canyons, and continental shelf breaks (Holloway et al., 1997). Ocean stratification is primarily determined by wind-induced mixing and solar heating exchange at the air-sea interface. The stratification is described by the buoyancy frequency (or Brunt-Vaisala frequency). The water depth of the peak of the frequency profile with a significant density change is called a pycnocline. If the stratification is vertically uniform, these waves propagate

obliquely through the ocean. If the stratification is concentrated in a thin layer, these waves move horizontally along the interfaces between neighboring water layers of different densities in the stratified oceans.

The particular type of internal waves most observed is termed a solitary wave, which presents a wave of permanent form. Solitary waves are finite-amplitude waves of permanent form which owe their existence to a balance between nonlinear wave-steepening processes and linear wave dispersion. They consist of single isolated waves, whose speeds are an increasing function of the amplitudes (Grimshaw, 2002). In the ocean, we often observe several internal waves in a packet, which change very slowly and are often rank ordered with largest waves near the front. Although these waves are not truly permanent, they have similar shapes as solitary waves and may treat them as solitary-like. The internal waves studied in the thesis are those solitary-like mode-1 internal waves traveling along the water interface, termed as internal solitary waves (ISWs). Mode-1 structure means that all isopycnals are displaced in the same direction. Mode-1 ISWs have much larger amplitudes and propagation speeds than other modes.

Internal waves have many practical reasons to be studied within the scientific and engineering communities. The large amplitudes of internal waves are potentially hazardous to sub-sea oil and gas drilling operations as the strong currents and shears associated with them may exert extreme stresses on offshore platforms and drill pipes. The temperature perturbation during internal waves' passage can cause large fluctuations in the sound speed and thus affect acoustic signal propagation in the coastal water (Apel

et al., 1997). Furthermore, the considerable speed shear of internal waves can initiate bottom sediment re-suspension (Bogucki et al., 1997; Chen and Hsu, 2005; Chen et al., 2007) and mix nutrients into the photic zone (Holligan et al., 1985), thereby fertilizing the local region and impacting the local biology system. The role of internal waves in vertical mixing of the world's ocean is also believed to be an important factor in maintaining the ocean structure and circulation (Killworth, 1998), and also in determining heat transfer between the ocean and atmosphere.

1.2 Remote sensing of ISWs

Oceanic ISWs observation can be directly made by measuring the isotherm displacement or the horizontal and vertical current induced by ISWs using *in situ* measurement. However, all the field measurements are usually limited to specific sites and time periods, which have a high temporal resolution in the expense of the spatial resolution. Not even to say, in some area, intense fishing activity inhibits comprehensive mooring measurements such as the ocean northeast of Taiwan. It is remote sensing, both radar and optical, such as SAR and the Moderate Resolution Imaging Spectroradiometer (MODIS) imagery, that has brought the realization of the widespread existence of ISWs (Figures 1.1, 1.2) (Apel and Jackson, 2004; Jackson, 2007).

1.2.1 Different remote sensing platforms

Since the penetration depth of electromagnetic waves in the sea water is very limited, most remote sensing instruments can only 'see' the surface. Information on processes below the surface (e.g. ISWs) or above the surface (e.g. wind variations) can be derived if

such processes modulate observable surface properties and we understand the modulation mechanisms.

ISWs, traveling interior the ocean, which cause almost no surface elevation, but they are accompanied by a spatially and temporally varying surface current field which interacts with the surface waves. The current induced by ISWs can modulate sea surface capillary and short gravity waves into smooth divergent and rough convergent zones. SAR image intensities are sensitive to the sea surface roughness through the Bragg scattering mechanism. As a result, depression ISW signatures are denoted by alternating brighter and darker stripes corresponding to the rougher and smoother areas on the sea surface (Alpers, 1985). For an elevation ISW, its current filed is just opposite to what a depression ISW induces and the resulting ISW signature is alternating darker and brighter stripes. Figure 1.3 shows a schematic diagram of interaction of ISWs, surface current field, and wind waves, and resultant SAR image intensity variation for both a depression ISW and an elevation ISW.

SAR is proved as an effective method of imaging the surface manifestation of oceanic ISWs and studying general ISW properties with its all-weather, all-day capability, high spatial resolution, and wide coverage. Clearly understanding all these characteristic properties of ISW signatures and their causes is very important for a correct interpretation of SAR observations, especially in those areas where no *in situ* measurements are available. An extensive collection of SAR images of ISWs around the world can be found at http://www.internalwaveatlas.com.

Past and present SAR sensors have been operated by the United States, Canada, Europe, Japan, and China. The SARs using in this thesis include those aboard European Remote-sensing Satellites-2 (ERS-2), Environmental Satellite (ENVISAT), and Canada's earth observation satellite-1 (RADARSAT-1). The SAR aboard on ERS-2 operates at a C-band (5.3 GHz), transmits and receives the radar signal at vertical polarization (VV). The range of incidence angles is from 19.5° in the near range to 26.6° in the far range, centered at 23.0°. ERS-2 SAR images have a 100 km swath and a resolution of 25 m. ENVISAT advanced SAR (ASAR) operates in the C- band in a wide variety of modes: alternating polarization, image, wave, and ScanSAR modes. It combines different polarities, angles of incidence, and spatial resolutions. RADARSAT-1 SAR also operates in the C-band, transmits and receives the radar signal at horizontal polarization (HH), and can operate in several different beam modes: standard, wide, fine, ScanSAR, and extended modes, which offer different image resolutions and coverage. The specific modes of ENVISAT and RADARSAT-1 SAR images used in the thesis are discussed in details in section 2.1.

Marine X-band radar systems operating at grazing incidence are widely used on ships for navigation. They operate by transmitting microwave pulses that interact with the rough sea surface and measuring the backscattered signal at the instrument. The radar echo is primarily dependent on small-scale ripple waves due to Bragg scattering (Valenzuela, 1978). The use of marine radar for scientific purposes has been limited to the collection of surface wave data until recently. It has the similar imaging mechanism

of SAR to detect ISWs' signatures by observing modulations in the surface roughness associated with currents induced by the ISWs.

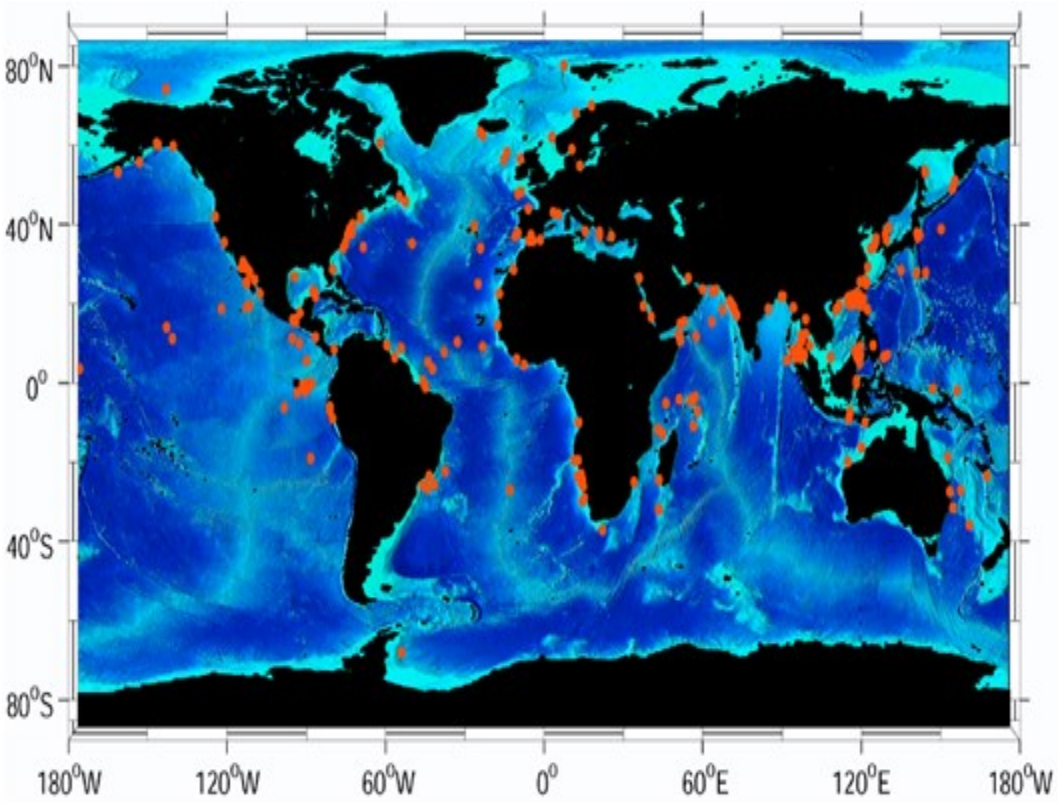

Figure 1.1. Locations of observed ISW occurrences around the world. Most locations were detected in satellite SAR imagery. As additional data and imagery are collected, the number of noted occurrence locations will certainly increase (Apel and Jackson, 2004).

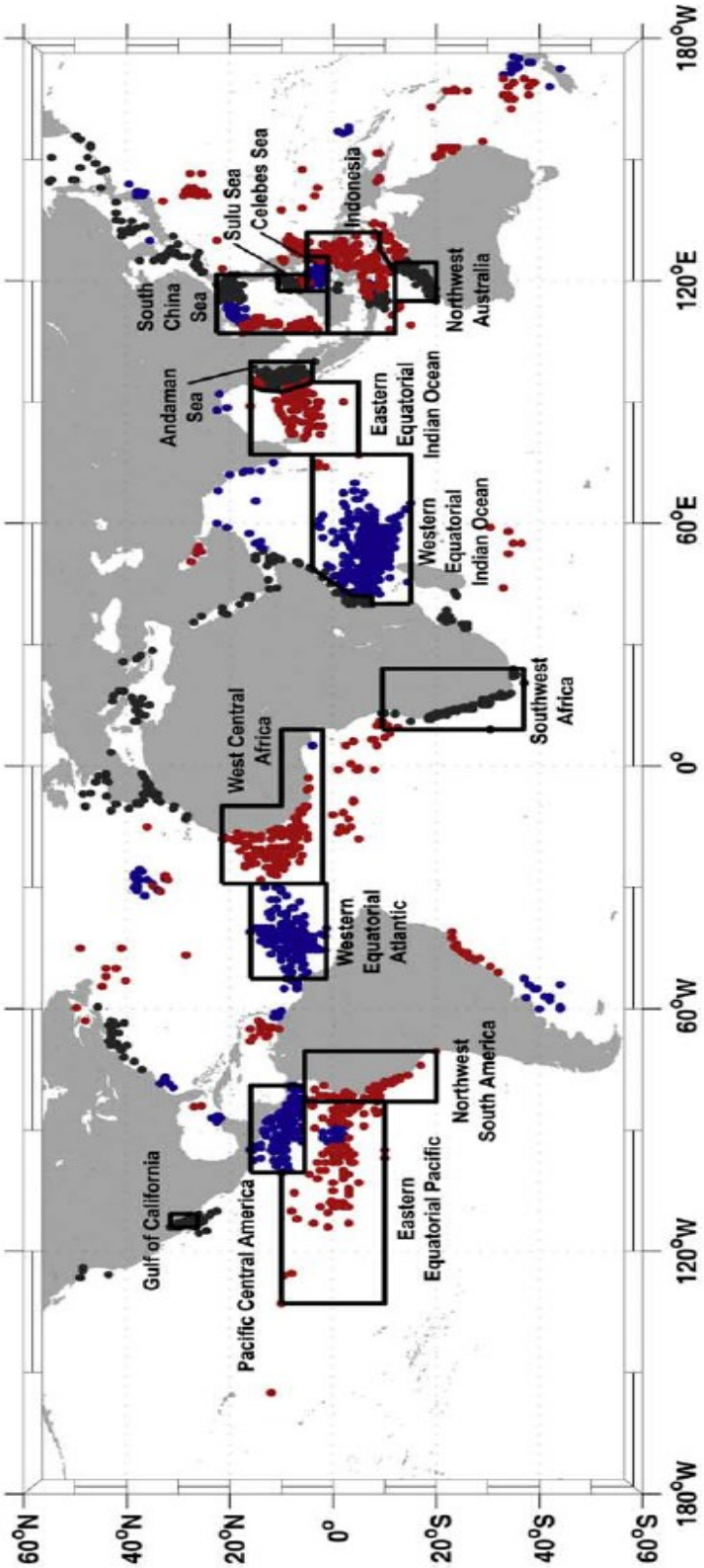

Figure 1.2. Location of ISWs observed in MODIS imagery from August 2002 through May 2004 (Jackson, 2007).

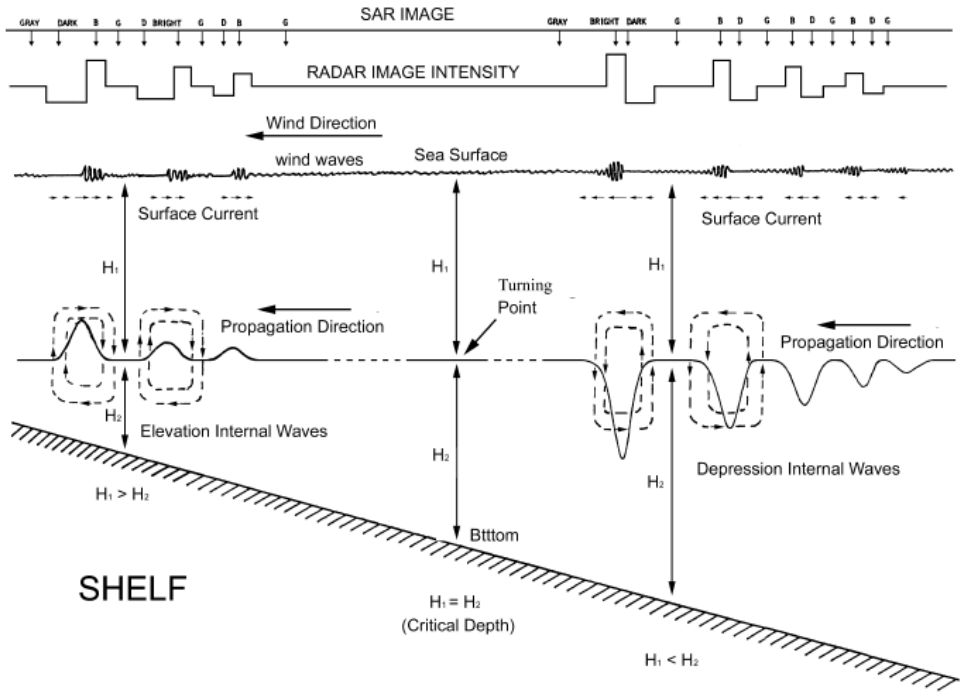

Figure 1.3. Schematic diagram of interaction of ISWs, surface current field, and wind waves, and resultant SAR image intensity variation (Liu et al., 1998).

Marine X-band radar data have a high temporal resolution but a relatively small coverage. They can provide a more complete view than a single satellite image because the ship can follow individual ISWs for some period of time and therefore permit studies of ISW evolution. Watson and Robinson (1990) first used marine radar data to study the evolution of ISWs at the Strait of Gibraltar using screen photographs of the marine radar, and Orr and Mignerey (2003) used marine radar data to track ISWs in the South China Sea (SCS). Chang et al. (2008) showed that the marine radar backscatter intensity can be used to estimate ISW induced horizontal velocity convergence and amplitude. However, these studies used original marine radar data manually with low temporal resolution and the weak signals can have significant errors caused by ambient noise, the backscatter

ramp, platform moving, and ISWs moving and result in poor interpretation of ISW properties without further corrections. Ramos et al. (2009) developed a methodology based on Radon transform techniques to enhance the signatures and detect ISW-related features from radar backscatter image sequences. It allows us to compute the following ISW properties: direction of propagation, wave speed, distance between solitons, and number of solitons per packet. Zha et al. (2012) adopted the method to estimate the force exerted by ISWs on a cylindrical pile and show ISWs' huge impact on underwater structures. Lund et al. (2013) developed a new fully automated tool to retrieve ISW signatures from image sequences. These signatures are ship-motion corrected, ramp-removed, normalized, and ISW-enhanced. This marine radar signature analysis tool provides a good method of studying spatio-temporal evolution of ISWs as they propagate.

The optical imagery is primarily applied in land remote sensing, however, it can also be used to study ISWs in the ocean when cloudfree or partially cloudfree conditions are encountered. Imaging ISWs by optical sensors is also closely associated with the variation of sea surface roughness (Mitnik et al., 2000; Jackson, 2007; Jackson and Alpers, 2007). However, one has to distinguish whether the sea surface manifestation of the ISWs lie inside, outside the sunglint area, or in the transition zone. In the sunglint area, ISWs become visible because the sunglitter radiance depends on the slope distribution of the surface waves, which is modulated by the surface current associated with ISWs. In the non-sunglint area, ISWs become visible because the diffuse reflection

of sunglint depends also on the slope distribution of the surface waves. Take a depression ISW for an example, in SAR images, radar signature has a bright line in front followed by a dark line corresponding to a rougher sea surface followed by a smoother sea surface, while in optical images the front line is imaged as a bright line when the imaged area lies outside the sunglint area and as a dark line when it lies inside of the sunglint area (Figure 1.4).

MODIS sensors onboard NASA's Earth Observing System satellites Terra and Aqua collect data in a continuous systematic manner at 250 m and 1 km resolution dependent on the collection wavelength on a 2300 km swath providing near-global daily coverage. Systeme Pour I'Observation de la Terre (SPOT) has a much smaller swath width of 60 km at a much higher resolution (2.5-20 m) and covers only a smaller portion of the world on a daily basis. Mitnik et al. (2000) discussed the similarities and differences of ISW signatures between ERS SAR images and sunglint images from SPOT. Jackson (2007) presented a survey that detected 3581 ISWs using MODIS imagery and discusses the ways of MODIS imagery can be used to improve ISWs study. Jackson and Alpers (2007) introduced the concept of a critical sensor viewing angle in brightness reversals on sunglint images of the sea surface. The ability to use optical imagery, particularly in combination with SAR sensors, has important applications in studying ISWs.

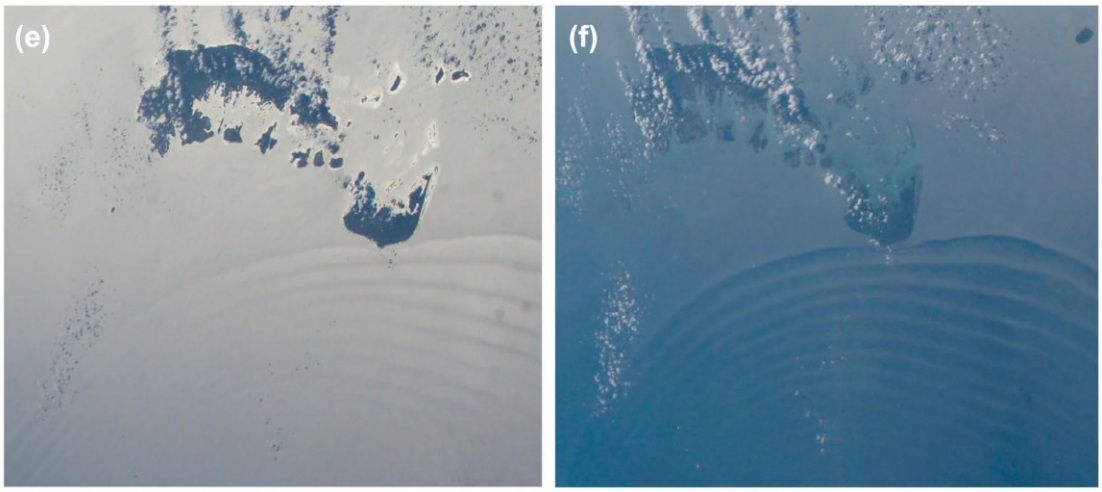

Figure 1.4. Astronaut photographs showing the brightness reversals of ocean surface signatures. (e) ISS009-E-7788 and (f) ISS009-E-7792 of a high frequency ISW packet in the Bali Sea near the Indonesian island Kepulauan acquired on May 18, 2004 (Jackson and Alpers, 2007).

1.2.2 ISW signatures interpretation

ISW signatures in optical imagery are essentially related to the sea surface roughness, just like those signatures in radar imagery. As a result, I mainly focus on ISW signatures interpretation from the most widely used SAR imagery in this section. ISW signatures interpretation can be divided into three general categories: optimal observation conditions for ISW imaging and the causes of different ISW signature types; ISW generation mechanisms and distribution maps; ISW-related parameters estimation.

ISW signatures captured by SAR, which depend on many parameters, are not the distribution of ISWs in the ocean directly. For example, if a wind speed exceeds 10 m/s, ISW signatures are hardly to be observed. There are many other factors affecting ISW signatures in SAR images such as radar parameters and ISW-related parameters. Yang et al. (2001) examined the relationship between modulation depths of ISW signatures and

these factors using a simulation model based on a simple bragg imaging model of ISWs. The modulation depths are stronger and weaker backscatter relative to the background corresponding to the rougher and smoother areas on the sea surface. The simulation results are shown in Figure 1.5. $\Delta\sigma^0$ denotes the deviation from its mean normalized radar cross section (NRCS) value. We can see that a thinner pyconline depth, larger density variation of the pycnocline, smaller radar frequency, and smaller incidence angle result in the largest modulation depth and strongest ISW signatures in SAR images. In addition, 0° and 180° are optimal directions for the angle between the radar look direction and ISW propagation direction, for SAR observation. ISW signatures in radar images depend not only on the dynamic characteristics of the interior ocean and radar parameters, but also on phenomena taking place at the air-sea interface such as surface roughness variability. The study by Brandt et al. (1999) suggested that ISW signatures had dependence on the wind direction relative to the ISW propagation direction and the wind speed by using numerical simulations of NRCS variations with an advanced radar imaging model (composite surface model). Ouyang et al. (2011) also used the same model to comprehensively examine the effects of radar parameters and wind conditions on the modulation depths of ISW signatures.

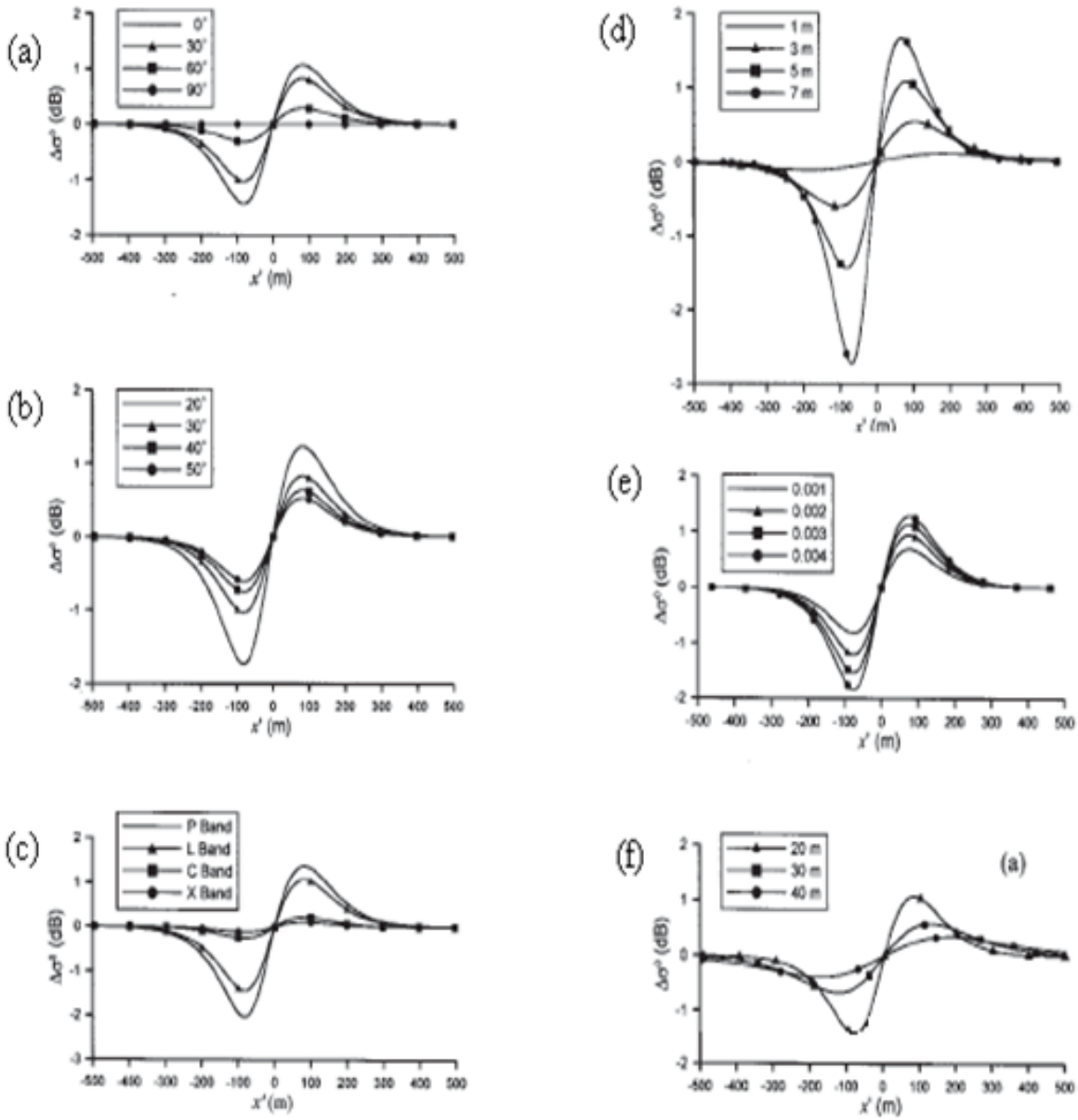

Figure 1.5. (a) $\Delta\sigma^0$ under different radar look directions (b) $\Delta\sigma^0$ under different radar incidence angles (c) $\Delta\sigma^0$ under different radar bands (d) $\Delta\sigma^0$ under different ISW amplitudes (e) $\Delta\sigma^0$ under different density variations of pycnocline (f) $\Delta\sigma^0$ under different pyconcline depths for a depression ISW (Yang et al., 2001).

da Silva et al. (1998) first summarized three different types of ISW signatures in SAR images on the continental shelf region of the western Iberian (the west of Portugal). These types include: (1) positive and negative backscatter variations from the mean background level (designated by brighter-darker double-signed signatures), (2) predominant negative variations relative to the mean (single-negative), and (3) redominant positive variations departing from the background (single-positive). These three different types were first explained by the role of surface films. Araujo et al. (2002) examined the role of wind direction on ISW signature types in the western Iberian shelf and draw a conclusion that the wind played very important in ISW signature types in SAR images. Xue (2010) focused on the statistics of ISW signature types in the Mid-Atlantic Bight (MAB) and assessed the role of wind condition on ISW signature types in the MAB and explained the statistics result by using the radar backscattering model used in Brandt et al. (1999). The model simulation results indicate that ISW amplitude plays an important role in ISW signature types besides wind conditions. Therefore, accurately estimating the ISW amplitudes from SAR is very necessary to fully understand different types of ISW signatures.

Satellite images, with their wide coverage and frequent revisiting times, are very useful to study ISW generation mechanisms and distributions maps. Zheng et al. (1993) presented a statistical and dynamical analysis of ISWs in the MAB from two space shuttle photographs and confirmed the tides were a dominant generation force for ISWs. Dokken et al. (2001) obtained geometric and radiometric signature statistics of ISWs

along the coast of Norway and identified four “hot-spot” areas with distinctive characteristics. Hsu et al. (2000) used ERS-1/2 SAR images to study ISWs distributions in the East and South China Sea and suggested the influence of the tide and the upwelling induced by the Kuroshio to be the generation mechanism. New and da Silva (2002) provided remote sensing evidence for the local generation in the central Bay of Biscay by the surfacing of a beam of internal tidal energy originating from the shelf break. Azevedo et al. (2006) investigated available SAR images to reveal the southern Bay of Biscay was also a “hot-spot” for ISWs and da Silva et al. (2007) studied the local generation of ISWs in this area. da Silva and Helfrich (2008) studied two dimensional propagation characteristics of ISWs in Massachusetts Bay using SAR images and inferred the likely generation mechanism from flow passage through resonance. da Silva et al. (2009) interpreted ISWs observed in the Mozambique Channel and investigated seasonal differences in the wave patterns. da Silva et al. (2011) first showed the full two dimensional spatial structures of ISWs around the Mascarene Plateau in the western Indian Ocean by SAR images and also confirmed the existence of second mode ISWs in this area. Zhao et al. (2004) showed ISWs distribution in the northeastern SCS from 1995-2001 from SAR images and provided the evidence for their baroclinic tide origin instead of lee-wave mechanism. Zheng et al. (2007) used the same 7 year satellite images for the statistical analysis of ISW occurrence in the northern SCS, and used filed experiments of wind, sea state, temperature to analyze ISW generation and SAR imaging

conditions. Li et al. (2008) studied the characteristics of ISWs in the northwestern SCS and suggested these ISWs originate from tide-topography interactions in the Luzon Strait.

Basic horizontal ISW parameters can be determined directly from a single or a series of satellite images. They include the propagation direction, crest length, wavelength, phase speed, and the number of solitons in a packet. ISW wavelength is very straightforward to estimate, defined as the distance between successive peaks along a radar intensity profile. Figure 1.6 shows a schematic of ISW features in both horizontal plan and profile views. The rightmost wave crest is just generated by offshore tide flow at the shelf break, whereas the leftmost one is the result of a previous semidiurnal tide. C_r, 2η and λ_0 are the wave crest length, amplitude and wavelength, respectively. $c_o T$ is the distance between packet centroids, and $V_{\max} T$ is the internal tidal wavelength.

Moreover, in order to understand more details about ISW properties and ocean environment parameters from ISW signatures in the images, we need a solitary wave theory that describes the evolution of nonlinear ISWs. Weakly nonlinear KdV-type theories are widely used in satellite-related ISWs study because these theories can describe the essential features of ISWs with a reduced wave equation (Helfrich and Melville, 2006). Depending on the ratio of ISW wavelength to the water depth below or above the interface, there are three theoretical regimes that describe the behavior of ISWs: the Korteweg-de Vries (KdV) equation (shallow water case), the Intermediate Long Wave (ILW) equation (intermediate–depth case), and the Benjamin-Ono (BO) equation (deep water case) (Benney, 1966; Benjamin, 1966; Ono, 1975; Joseph, 1977; Kubota et

al., 1978; Choi and Camassa, 1999). The details of the KdV, ILW, BO equations for a two-layer flow can be found in Appendix A. The development of extended models such as the higher-order KdV equation containing a higher-order nonlinearities is used to describe large amplitude ISWs with high nonlinearity (Ostrovsky and Stepanyants, 2005). Among all these weakly nonlinear theories, the KdV theory has a robust range of validity in successful prediction of experimental or observational ISWs, even outside of its strict assumption, while the BO or ILW theory appears not to do so (Grue et al, 1999; Small et al., 1999; Helfrich and Melville, 2006).

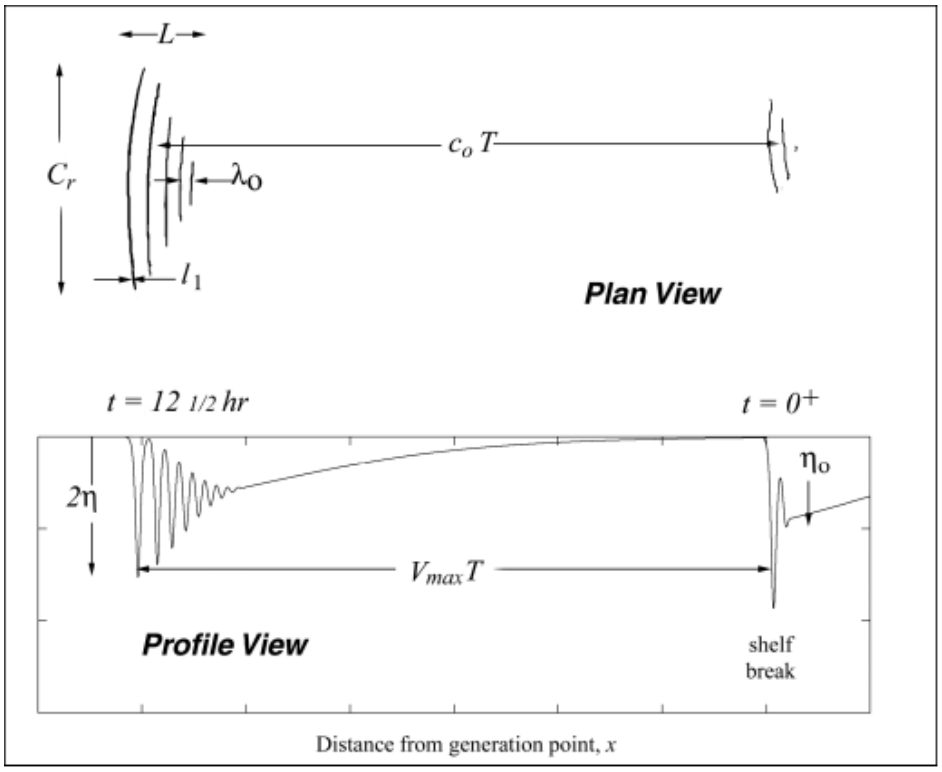

Figure 1.6. Schematic showing tidally-generated solitons on the continental shelf. $V_{\max}T$ is the internal tidal wavelength; c_oT is the distance between packet centroids (Apel and Jackson, 2004).

Liu (1988) developed the KdV equation, including effects of vertical shear, variable bottom topography, radial spreading, shoaling, and dissipation, to study ISW evolution. Porter and Thompson (1999) estimated the thickness and density of the surface layer from the dispersion relation obtained from a two-layer depth model. Li et al. (2000) estimated the upper layer depth in the MAB by matching theoretical wave speed of a two-layer depth model with ISW speeds estimated from SAR images, assuming a semidiurnal tide origin for these waves. Zhao et al. (2004) estimated ocean stratification structure in a two-layer model based on the polarity conversion of an ISW using the higher-order KdV equation. Accurate amplitude estimation from ISW signatures in radar images can improve our understanding of ISWs where no *in situ* data are available. Zheng et al. (2001) first developed a theoretical model to relate the distance between the positive peak and the adjacent negative peak (p-p distance) of ISW signatures to the soliton amplitude described by the KdV equation in a two-layer stratified ocean. Yang et al. (2003) adopted the method to estimate ISW amplitudes in the SCS and the results turned out to be reasonable estimations in the area. Stanton and Ostrovsky (1998) presented a higher-order KdV equation to reproduce the highly nonlinear ISWs observed over the continental shelf, where the KdV equation could not make a good approximation. Pan and Jay (2008) also analyzed large ISWs' dynamics using a higher-order KdV equation at the Columbia river plume and the results agreed well with *in situ* measurements. Pan et al. (2007) made the scale analyses and used finite-depth category to describe ISWs generated at the Columbia River plume. Recently, Chen et al. (2011)

derived ISW amplitude in the SCS deep basin from satellite image using the BO equation (the deep water case) and imaging model proposed by Zheng et al. (2001).

Another common and interesting yet rarely studied feature observed in satellite images is internal wave-wave interaction. Note that satellite images provide the best way to observe the complete interaction pattern, comparing with the small coverage of marine ship radar data and limited *in situ* point measurements. Understanding the mechanisms of the interaction pattern in the images plays an important role in the understanding of vertical mixing and energy redistribution. Moreover, these interactions may result in exceptionally large amplitudes in the interaction zone, which in turn pose threats to underwater structures. Hsu et al. (2000) observed the nonlinear wave-wave interaction on RADARSAT-1 ScanSAR wide images, but the study did not focus on the phase shifts or changes of ISW properties in the interaction zone. Chen et al. (2011) used the theory of resonant interaction of two ISWs based on the Kadomtsev-Petviashvili (KP) equation to explain a satellite image exhibiting special patterns, providing a mechanism for boosting ISW amplitudes. However, not many studies have been done on wave-wave interaction characteristics. Xue et al. (2012) investigated qualitatively the phase shifts and amplitude changes associated with regular interaction patterns visible in satellite images using the KP model.

1.3 Motivation and thesis organization

From July to September 2006, the Nonlinear Internal Wave Initiative/Shallow Water 2006 (SW06) experiment, a large, multi-institution, multi-investigator project, was

carried out in the MAB. This experimental campaign was designed to understand the impact of nonlinear ISWs on acoustic propagation and scattering in shallow water and was designed to combine a great variety of instruments on different platforms including acoustics and oceanographic moorings, aircraft, shore-based high frequency radar, Air-Sea Interaction Spar buoys, satellite imagery, and sampling devices on board research vessels.

The MAB area is characterized by a broad shelf and steep slope interrupted by numerous small canyons. The area has a significant continental shelf extending up to 250 km from shore and is influenced by the Gulf Stream circulation as well as short duration wind driven upwelling and estuarine exchanges. High frequency nonlinear ISWs are generated near the shelf break during stratified conditions (late spring to early fall) and tend to propagate toward the shelf (Apel et al., 1997). The semidiurnal tidal flow is dominated by the principal lunar constituent M2 (12.4 hour period), which propagates toward the shelf from the North Atlantic.

The main motivation of this thesis is to get a profound understanding of ISW signatures in satellite and marine X-band images collected during the experiment by exploiting and making full use of this comprehensive dataset. Xue (2010) showed that relating ISW signature types mainly to the wind direction is an oversimplification without considering other factors such as ISW amplitudes in the MAB. As a result, one of two primary objectives of this thesis is to choose a suitable weakly nonlinear model to describe large amplitude ISWs in the MAB and develop a method to estimate ISW

amplitudes from their signatures in the SAR and marine X-band images. We also observe many internal wave-wave interactions in the SAR and SPOT images so the second objective of the thesis is to understand these interaction patterns observed and the complex dynamics involved with different characteristics exhibited in the patterns such as phase shifts and amplitude changes due to the interaction.

The organization of this thesis is listed as follows. Chapter 2 describes all the datasets used including SAR images, marine X-band radar data, SPOT images, environmental and structure moorings, and Conductivity-Temperature-Depth (CTD) casts. Chapter 3 presents the method and validation of estimating large ISW amplitudes from p-p distances of ISW signatures in radar images by the higher-order KdV equation. This work has been published in IEEE Transactions on Geoscience and Remote Sensing (Xue et al., 2013a). Chapter 4 shows the internal wave-wave interaction patterns observed in satellite SAR and SPOT images from July to September 2006 and gives a detailed analysis of four observed interaction patterns and compares the findings with existing analytical and numerical models for two-soliton interaction. This work is in press in IEEE Transactions on Geoscience and Remote Sensing (Xue et al., 2013b). Chapter 5 is the summary of this thesis. Appendix A describes the KdV, ILW, and BO equations for a two-layer stratified ocean. Appendix B gives a detailed analytical expression for ocean ISW signature in a satellite image. Appendix C shows ten internal wave-wave interaction patterns which are not discussed in details in Chapter 4 and classifies them into the four categories as defined in Chapter 4.

CHAPTER 2 SW06 FIELD EXPERIMENT

The SW06 experiment combined a great variety of instruments on different platforms including environmental and structure moorings, aircraft, shore-based high frequency radar, satellite imagery, and sampling devices including Wave Monitoring System (WaMoS) on board research vessels.

Figure 2.1 shows the bathymetry of the study area. Contour lines indicate depths of 50 m, 100 m, 200 m, 300 m, 400 m, 500 m, and 1000 m. Blue dots show the locations of Air-Sea Interaction Spar (ASIS) buoys, and red dots are the nominal locations of the environmental moorings, which gives a general idea about the setup of the moorings in the experiment. Three of the six environmental moorings are arranged along a line in the across-shelf direction and the other three in the along-shelf direction. Marine X-band radars mounted on the research vessels are used to observe and follow the ISWs near the moorings. A more complete description of the entire experimental setting can be found in the report by Newhall et al. (2007). Besides these moorings measurements, many satellite images including ERS-2 SAR, ENVISAT ASAR, RADARSAT-1 SAR, and SPOT-2/4 were taken during the experiment period. With this unique dataset, we can pick out the cases of ISWs shown both on satellite or marine X-band radar images and the nearby moorings. The spatial distribution of the ground coverage for the satellite SAR and SPOT is shown in Figure 2.2. Our understanding of ISW signatures and ISW properties estimation can be improved by the two fold approach.

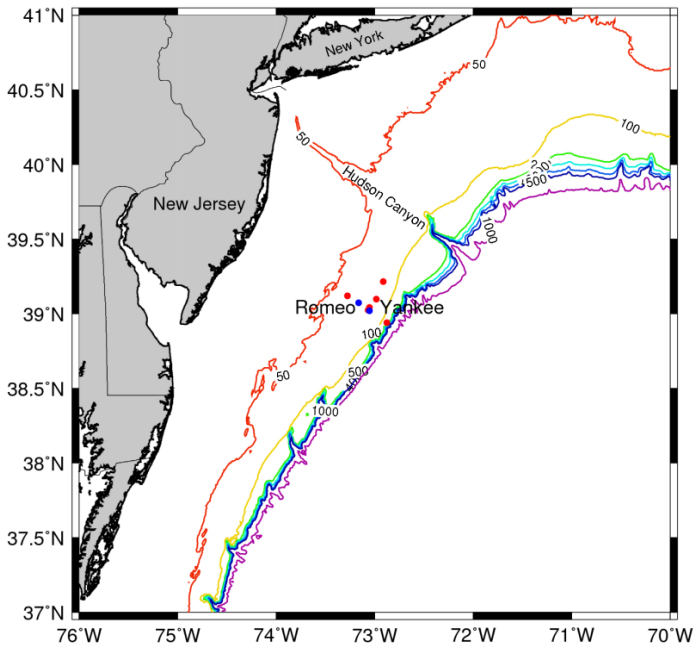

Figure 2.1. Bathymetry of the MAB. Contour lines indicate 50 m, 100 m, 200 m, 300 m, 400 m, 500 m and 1000 m. The circles show the locations of the environmental moorings (red) and ASIS buoys (blue) (Caruso and Graber, 2006).

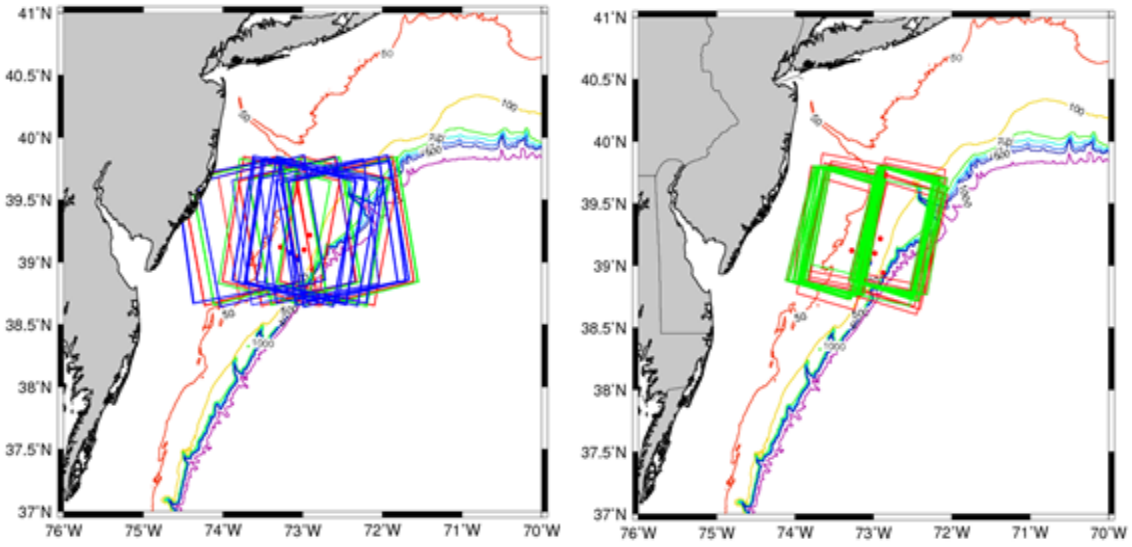

Figure 2.2. Distribution of SAR (left) and SPOT (right) footprints during the field experiment. Red, green, and blue rectangles in the left image show the ENVISAT, ERS-2, and RADARSAT-1 locations, respectively. Red and green rectangles in the right image indicate the SPOT-2 and SPOT-4 locations (Caruso and Graber, 2006).

2.1 Satellite imagery

57 SAR images were acquired over the MAB region during the experiment. There are 11 ERS-2 SAR, 12 ENVISAT ASAR and 34 RADARSAT-1 SAR images, all of which were acquired through the University of Miami's Center for Southeastern Tropical Advanced Remote Sensing (CSTARS). Table 2.1 shows a list of the collected SAR images. ENVISAT ASAR images here used the image mode at VV polarization. Different image swath (IS) modes stand for different incidence angles and swath widths. IS2 beam mode has a center incidence angle of 23°, which is the same as the one of ERS-2. RADARSAT-1 SAR images here used the standard beam mode, which allows imaging over a wide range of incidence angles acquired in seven different modes referred to as S1 to S7. The incidence angles range from 20° at the inner edge of S1 to 49° at the outer edge of S7. Figure 2.2 shows the satellite imagery coverage in the experiment. Red rectangles illustrate the ENVISAT coverage; green ones denote the ERS-2 coverage; and blue ones show the RADARSAT-1 coverage in the left of Figure 2.2.

28 SPOT-2 and 40 SPOT-4 images were acquired through the CSTARS during the experiment. These optical images, with a swath of 60 km and a spatial resolution of 10 m, are from the high resolution panchromatic (HRV-PAN) scanner, which works in one visible band (0.50-0.73 μm). Table 2.2 shows a list of the collected SPOT images and the locations of these images are shown in Figure 2.2 (right). The SPOT-2 and SPOT-4 images were taken in nearly identical locations on descending passes during the day.

Table 2.1. List of SAR images acquired during the SW06 experiment.

Date	Time	Satellite	Beam	Polarization
14-Jul-06	2:37	ENVISAT	IS2	VV
14-Jul-06	3:06	ERS-2		VV
19-Jul-06	22:33	RADARSAT-1	S1	HH
23-Jul-06	15:07	ENVISAT	IS2	VV
23-Jul-06	15:36	ERS-2		VV
25-Jul-06	22:58	RADARSAT-1	S7	HH
29-Jul-06	22:41	RADARSAT-1	S3	HH
30-Jul-06	2:35	ENVISAT	IS2	VV
30-Jul-06	3:03	ERS-2		VV
30-Jul-06	10:55	RADARSAT-1	S3	HH
1-Aug-06	22:42	RADARSAT-1	S7	HH
2-Aug-06	2:28	ENVISAT	IS2	VV
2-Aug-06	2:57	ERS-2		VV
5-Aug-06	22:37	RADARSAT-1	S1	HH
6-Aug-06	10:51	RADARSAT-1	S5	HH
8-Aug-06	15:00	ENVISAT	IS2	VV
8-Aug-06	15:28	ERS-2		VV
8-Aug-06	22:38	RADARSAT-1	S6	HH
9-Aug-06	11:03	RADARSAT-1	S1	
12-Aug-06	22:33	RADARSAT-1	S1	HH
13-Aug-06	10:47	RADARSAT-1	S6	HH
15-Aug-06	22:45	RADARSAT-1	S4	HH
16-Aug-06	10:59	RADARSAT-1	S2	HH
18-Aug-06	2:37	ENVISAT	IS2	VV
18-Aug-06	3:06	ERS-2		VV
18-Aug-06	22:58	RADARSAT-1	S7	HH
20-Aug-06	10:43	RADARSAT-1	S7	HH
22-Aug-06	22:41	RADARSAT-1	S3	HH
23-Aug-06	10:55	RADARSAT-1	S3	HH
25-Aug-06	22:54	RADARSAT-1	S7	HH
27-Aug-06	15:07	ENVISAT	IS2	VV
27-Aug-06	15:36	ERS-2		VV
29-Aug-06	22:37	RADARSAT-1	S1	HH
30-Aug-06	10:51	RADARSAT-1	S5	HH
1-Sep-06	22:50	RADARSAT-1	S6	HH
2-Sep-06	11:04	RADARSAT-1	S1	HH
3-Sep-06	2:34	ENVISAT	IS2	VV

3-Sep-06	3:03	ERS-2		VV
5-Sep-06	22:33	RADARSAT-1	S1	HH
6-Sep-06	2:40	ENVISAT	IS2	VV
6-Sep-06	3:09	ERS-2		VV
6-Sep-06	10:47	RADARSAT-1	S6	HH
9-Sep-06	10:59	RADARSAT-1	S2	HH
11-Sep-06	22:58	RADARSAT-1	S7	HH
12-Sep-06	15:04	ENVISAT	IS2	VV
12-Sep-06	15:33	ERS-2		VV
13-Sep-06	10:43	RADARSAT-1	S7	HH
15-Sep-06	22:41	RADARSAT-1	S3	HH
16-Sep-06	10:55	RADARSAT-1	S3	HH
18-Sep-06	22:54	RADARSAT-1	S7	HH
22-Sep-06	2:37	ENVISAT	IS2	VV
22-Sep-06	2:54	ERS-2		VV
22-Sep-06	22:37	RADARSAT-1	S1	HH
23-Sep-06	10:51	RADARSAT-1	S5	HH
25-Sep-06	2:43	ENVISAT	IS2	HH
25-Sep-06	22:49	RADARSAT-1	S6	HH
26-Sep-06	11:03	RADARSAT-1	S1	HH

2.2 Marine X-band radar

A surface sampling X-band HH polarized radar system installed on board R/V Knorr and Oceanus was used to track ISWs in the experiment. The marine X-band data used in this thesis are from R/V Knorr. The sampling device was a WaMoS unit and it included a 9.4 GHz marine radar with a pulse repetition frequency of 3 KHz and a sampling frequency of 20 MHz. With this configuration, the backscatter images were collected every 1.45 s and covered a maximum range of 2.04 km. The range resolution was 7.5m and the dead range (inner range of no coverage) was 120 m (Ramos et al., 2009). R/V Knorr would typically remain stationary while sampling ISWs that propagated through its

position. The marine X-band radar data used in the study are ship-motion corrected, ramp-removed, normalized, and ISW signature-enhanced (Lund et al., 2013).

Table 2.2. List of SPOT-2/4 images acquired during the SW06 experiment.

Date	Time	Satellite	Date	Time	Satellite
21-Jul-06	15:41	SPOT-4	15-Aug-06	16:00	SPOT-4
21-Jul-06	16:08	SPOT-2	16-Aug-06	15:41	SPOT-4
25-Jul-06	16:04	SPOT-4	17-Aug-06	15:49	SPOT-2
26-Jul-06	15:45	SPOT-4	20-Aug-06	16:04	SPOT-4
27-Jul-06	15:53	SPOT-2	21-Aug-06	15:45	SPOT-4
28-Jul-06	15:34	SPOT-2	23-Aug-06	15:34	SPOT-2
30-Jul-06	16:08	SPOT-4	25-Aug-06	16:08	SPOT-4
31-Jul-06	15:48	SPOT-4	26-Aug-06	15:49	SPOT-4
1-Aug-06	15:57	SPOT-2	31-Aug-06	15:53	SPOT-4
2-Aug-06	15:38	SPOT-2	6-Sep-06	15:37	SPOT-4
5-Aug-06	15:52	SPOT-4	6-Sep-06	16:05	SPOT-2
6-Aug-06	15:33	SPOT-4	7-Sep-06	15:45	SPOT-2
6-Aug-06	16:01	SPOT-2	10-Sep-06	16:00	SPOT-4
10-Aug-06	15:56	SPOT-4	11-Sep-06	15:41	SPOT-4
11-Aug-06	15:37	SPOT-4	11-Sep-06	16:09	SPOT-2
11-Aug-06	16:05	SPOT-2	17-Sep-06	15:53	SPOT-2
12-Aug-06	15:45	SPOT-2	20-Sep-06	16:08	SPOT-4

2.3 Moorings

A component of this experiment was a moored array of physical oceanographic sensors that was designed to measure the vertical and horizontal structure of ISW fields generated at the shelf break as they propagated through the acoustics array (Irish et al., 2004). The across-shelf and along-shelf component of the moorings makes up a big “T” pattern in the experiment area (Figure 2.3).

Unfortunately, most of ISW occurrences in satellite images are out of the mooring area, which means only a few cases that the ISWs observed both in the moorings and satellite images. The same situation goes to the marine X-band radar data. The data from the heavily instrumented environmental moorings SW31 and structure mooring SW19 are used to validate the amplitude estimations of two cases. One is from a RADARSAT-1 SAR image and the other is from marine X-band radar data.

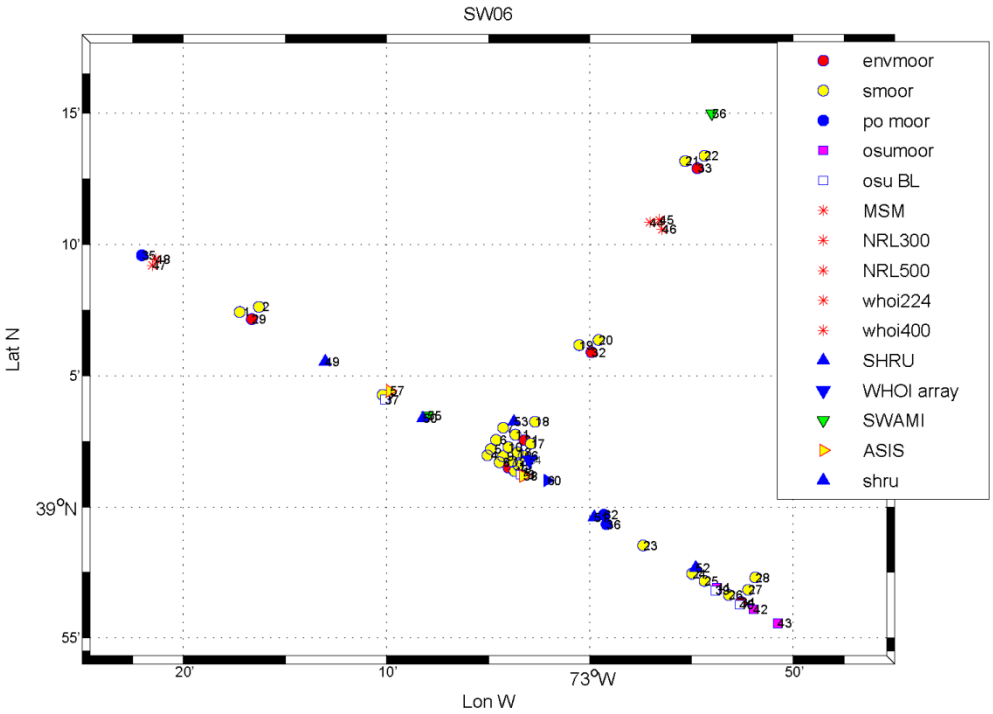

Figure 2.3. Location of the moorings in the SW06 experiment (Newhall et al., 2007).

2.3.1 Environmental moorings

Three of the six environmental moorings were aligned in the across-shelf direction and the other three in the along-shelf direction (red dots in Figure 2.3). Environmental moorings were all subsurface with a buoyancy about 12 m deep so the uppermost temperature, conductivity, pressure sensor was at about 14 m depth. The bottom package

of acoustic Doppler current profilers (ADCP) and a temperature, conductivity, pressure sensor was located just above the acoustic release about 7 m above the bottom (Irish et al., 2004).

The environmental moorings were heavily instrumented. Taking the mooring SW31 for example, it was located at 39.043° N, 73.054° W in 83 m water depth, including seven CTD recorders distributed along the water column and a temperature recorder located 1 m below the surface, which unfortunately lost its data. Table 2.2 gives details of instruments on SW31 and Figure 2.4 gives a sketch of the mooring SW31. The vertical resolution of temperature sensors was around 10 m, which is too coarse to get the accurate ISW amplitude, however, can give a good approximate estimate. SW32 also hosted a 300 kHz upward looking ADCP at the bottom measuring water column speed profiles, particularly the vertical component which is very sensitive to ISW passages. Its ensemble sampling interval was 30 seconds, which was enough to resolve the high frequency temporal variability of ISW field. The vertical resolution of the ADCP was 4 m. The ADCP on SW31 was unfortunately flooded but the ADCPs in other moorings worked well.

Overall, with these environmental moorings, we can get temperature and current profiles during ISW passage. ISW properties such as wavelength and amplitude can be estimated from these measurements directly. We can also estimate the local phase speed of ISWs passing the moorings, based on the distance and time separation between the mooring and ISW locations in the satellite images.

Table 2.2. Details of instruments on SW31 (Newhall et al., 2007).

Instrument type	Number	Depth (m)
Mini-T	290	1
SBE37	399	12
SBE39	26	21
SBE37	1134	31
SBE39	6	42
SBE37	1136	53
SBE39	8	64
SBE37	397	75
ADCP	130	75

2.3.2 Structure moorings

Two structure moorings, yellow dots in Figure 2.3, were around each of these environmental moorings. These moorings were lightly instrumented only with one CTPR and two temperature recorders. The basic sample interval was also 30 s. Table 2.3 gives details of instruments on structure mooring SW19, and Figure 2.5 shows a sketch of the mooring's structure.

Table 2.3. Details of instruments on structure mooring SW19 (Newhall et al., 2007).

Instrument type	Number	Depth(m)
SBE39	3120	14
Mini-T	2003	25
Mini-T	2004	40

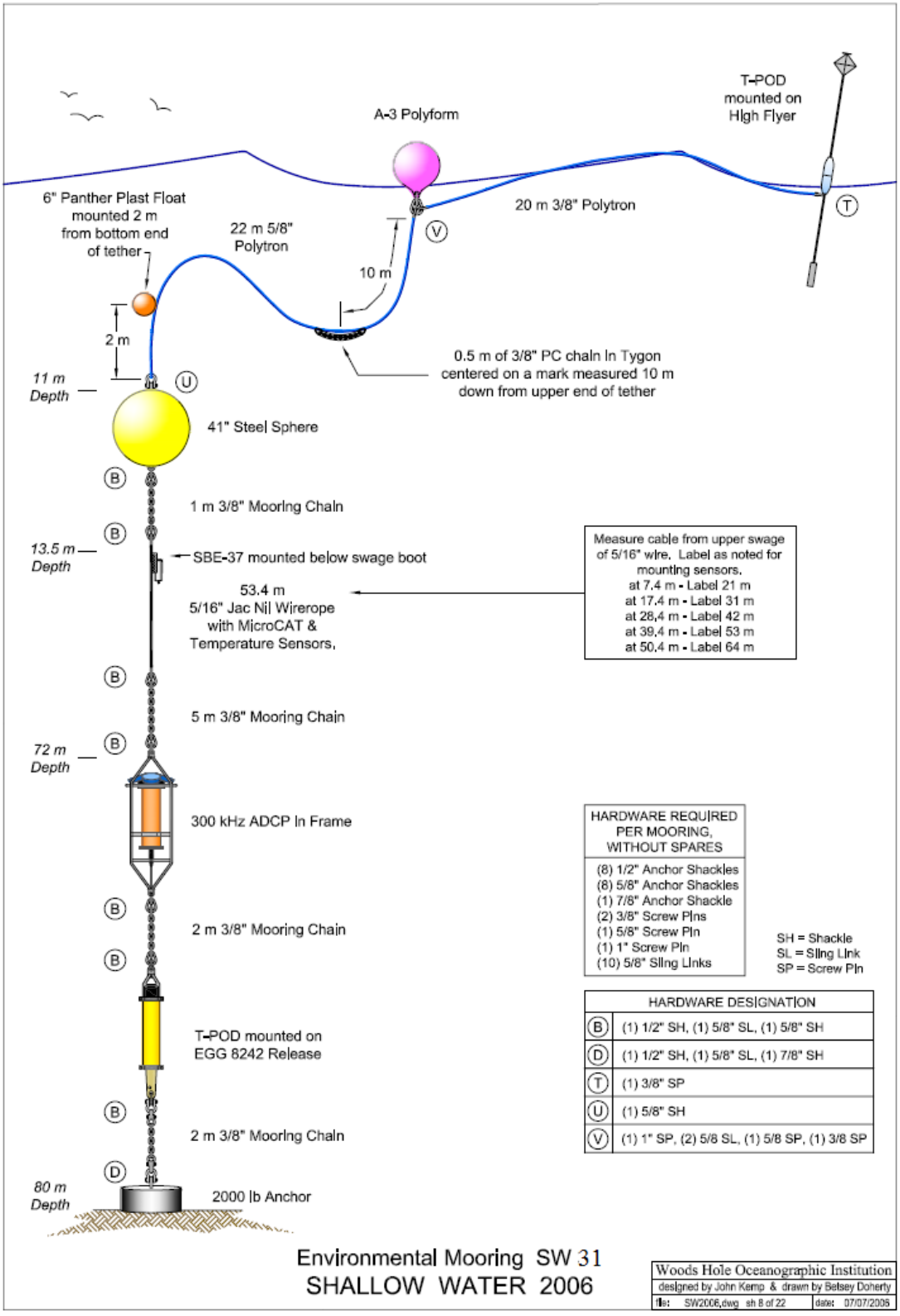

Figure 2.4. Sketch of SW31 (Newhall et al., 2007).

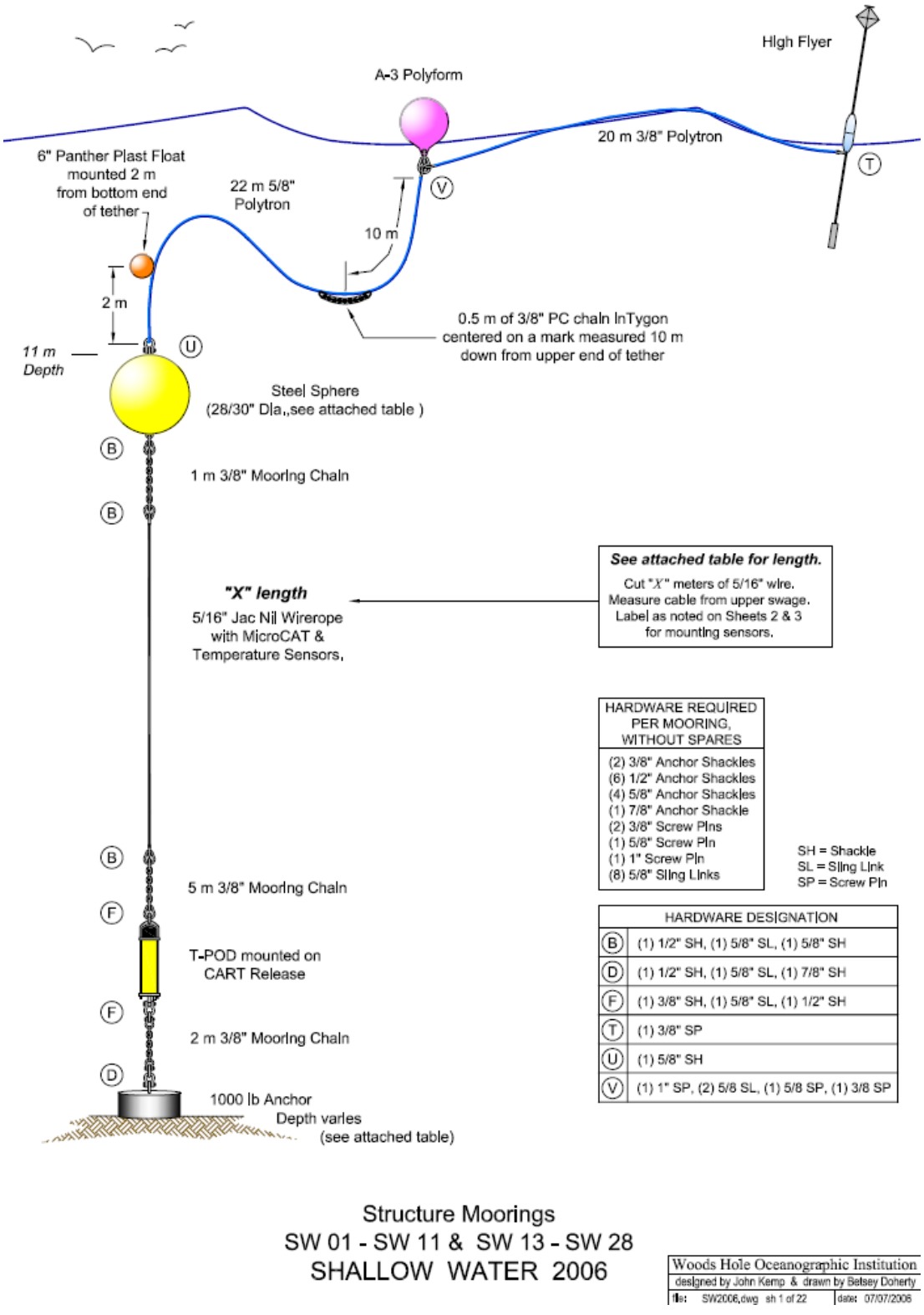

Figure 2.5. Sketch of SW19 (Newhall et al., 2007).

2.4 CTD casts

CTD casts were conducted by several research vessels at well-defined locations and times during the experiment (Figure 2.7). CTD data were recorded at a frequency of 24 Hz. Suitable CTD profiles were used to estimate environmental parameters for the description of ISW in the weakly nonlinear models.

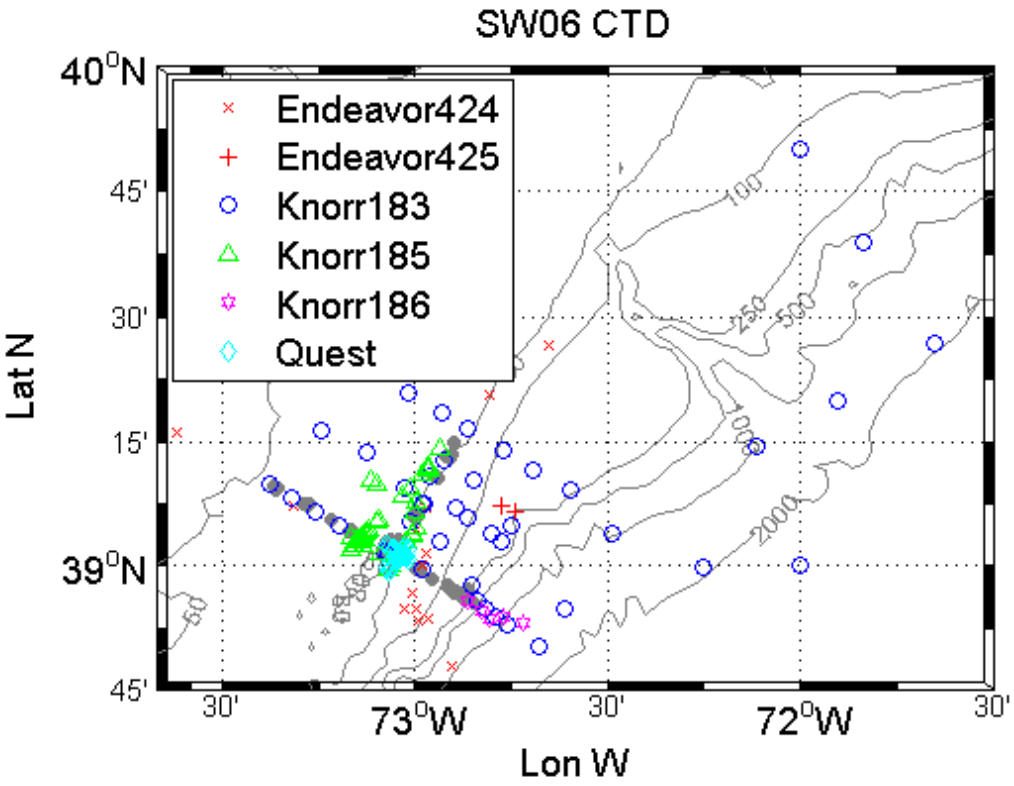

Figure 2.6. Location of CTD casts of different research vessels in the SW06 experiment (Newhall et al., 2007).

CHAPTER 3 AMPLITUDES ESTIMATION OF LARGE INTERNAL SOLITARY WAVES USING SAR AND MARINE X-BAND IMAGES

The accurate estimation of ISW amplitudes from radar images is important for understanding wave evolution, energy dissipation, and mixing processes. The *in situ* data from the SW06 experiment in the MAB show many ISWs with amplitudes of 10 m or more in a shallow water depth of 80 m or less. Therefore, the higher-order KdV equation in a two-layer stratified ocean is needed to describe these large amplitude ISWs instead of the KdV, ILW, and BO equations. Based on a simple theoretical radar imaging model, we develop a method to estimate large ISW amplitudes from distances between the positive and negative peaks of ISW signatures in radar images and a selection rule from the two resultant possible amplitude solutions. Two groups of ISWs with large amplitudes, determined from the temperature records from nearby moorings, are observed in a RADARSAT-1 SAR image and in marine X-band radar data collected during the experiment. The method is validated by using the ISW signatures taken from these two cases. The estimated amplitudes are found to agree well with those determined from the moorings. The proposed method provides a relatively simple and accurate way to estimate large ISW amplitudes from radar images.

3.1 Background

Since oceanic ISWs were first recognized on satellite SAR images in 1978, SAR has been proven to be a powerful tool for imaging surface manifestation of ISWs with its all-weather, all-day capability, high spatial resolution, and wide coverage. SAR can

monitor ISWs on a regular basis and observe the spatial distribution of ISWs. SAR images have been widely used to study ISW generation mechanisms, evolution, and properties (Liu, 1988; Porter and Thompson, 1999; Hsu et al., 2000; Li et al., 2000; Dokken et al., 2001; Zheng et al., 2001; New and da Silva, 2002; Zhao et al., 2004; Azevedo et al, 2006; da Silva et al., 2007; da Silva and Helfrich, 2008; Li et al., 2008). Shipborne marine X-band radars are also capable of detecting ISWs and methods to retrieve ISW information from marine radar data have been introduced recently (Change et al, 2008; Ramos et al., 2009; Zha et al., 2012; Lund et al., 2013). Marine radar data have a high temporal resolution but a relatively small coverage. They can provide a more complete view than a SAR image because the ship can follow individual ISWs for some period of time and therefore permit studies of ISW evolution. Field experiments with *in situ* measurements are costly and only provide point measurements. Thus, developing methods to extract accurate ISW parameters from radar images is important and can improve our understanding of ISWs where no *in situ* measurements are available.

ISW signatures in radar images depend not only on the dynamic characteristics of the interior ocean and radar parameters, but also on wind conditions at the surface (Brandt et al., 1999; Yang et al., 2001; Ouyang et al., 2011). All these parameters affect the modulation depths of ISW signatures significantly. Therefore, it is difficult to estimate ISW-related parameters from the modulation depths. However, as we will show, the p-p distance of ISW signatures is less affected by these parameters and thus can be used as a good indicator of ISW-related parameters.

ISW amplitude is defined as the maximum displacement from the undisturbed interface. Accurate amplitude estimation from ISW signatures in radar images can improve our understanding of ISWs. There are three weakly nonlinear theoretical regimes that describe ISWs: the KdV equation (shallow water case), the ILW equation (intermediate-depth case), and the BO equation (deep water case). The data from the SW06 experiment in the MAB show many ISWs with amplitudes of 10 m or greater in a shallow water depth of 80 m or less (Shroyer et al., 2009, 2011). Shroyer et al. (2011) used the background estimates of local density and shear from ship-based observations to show that the higher-order nonlinear effects become more important in shallow water in the MAB. Therefore the KdV, ILW, and BO equations are not applicable for these large amplitude ISWs and the higher-order KdV equation including a cubic nonlinearity term should be used in our study area. In this thesis, a method is developed to estimate large ISW amplitudes from radar signatures and a selection rule for the two possible amplitude results, based on a higher-order KdV equation and the theoretical radar imaging model used by Zheng et al. (2001). Two ISW cases from the SW06 experiment are used to validate the method.

This chapter is organized as follows: Section 3.1 introduces the datasets. Section 3.2 gives a theoretical description of the higher-order KdV equation and introduces the method to estimate ISW amplitudes from radar signatures. In section 3.3 we validate the method for two cases and compare the estimated amplitudes with *in situ* data. The effect of different environmental parameters on the amplitude estimations results is also

discussed. Section 3.4 summarizes our findings and concludes that the method developed in this chapter provides an easy and reliable way to estimate large ISW amplitudes from radar images. Section 3.5 discusses the limitation of the proposed method.

3.2 Datasets

The SW06 experiment combined satellite image acquisitions, an array of acoustic and oceanographic moorings, and marine radar and other sampling devices on board research vessels. It has provided a unique dataset to understand ISW signatures in radar images and study the vertical and horizontal structures of ISWs generated at the shelf break.

Two large ISW groups observed both by the moorings and in radar images have been chosen from the data collected in the experiment. A group of ISWs is observed in a RADARSAT-1 SAR image taken at 10:43 coordinated universal time (UTC) on August 20, 2006 using a standard beam mode with a resolution of 12.5 m shown in Figure 3.1. Mooring SW19 was located at 39.103°N, 73.009°W in 79 m water depth and had three temperature sensors between 14 m and 40 m water depth. A CTD cast 01 collected on August 27, 2006 was performed at 39.130°N, 72.998°W in 73 m water depth. An intensity transect across the ISWs near SW19 is marked in Figure 3.1 as AA'. In order to obtain a meaningful measurement of image intensity variations and reduce speckle to a negligible magnitude, the pixel intensities were averaged in the direction parallel to the wave crest. Only the first two solitons with clear signatures in AA' are studied and identified as A1 and A2.

The other group of ISWs is observed in the average of a 5-min-long sequence of ship-motion corrected, ramp-removed, and normalized marine radar images starting at 04:40:01 UTC August 14, 2006, shown in Figure 3.2. The marine radar data were acquired using a standard Furuno marine X-band radar operating at 9.4 GHz with HH polarization, grazing incidence angle, and short pulse length on board R/V Knorr. The radar has a pulse repetition frequency of 3 kHz with a sampling frequency of 20 MHz. The radar backscatter images were collected every 1.45 s, covering a range from 120 to 2040 m with a range resolution of 7.5 m. Mooring SW31 was located at 39.043°N, 73.054°W in 83 m water depth and had seven temperature sensors distributed between 12 m and 75 m water depth. A CTD cast 02 collected on August 27, 2006 was located at 39.026°N, 73.035°W in 75 m water depth. An intensity transect is selected across the ISWs and identified as BB' in Figure 3.2. Again, we have averaged the pixel intensities in the direction parallel to the wave crest. ISW signatures in the rear of BB' are contaminated by shadows of ship super-structures, and only the first three solitons with clear signatures are studied and marked as B1, B2, and B3.

Figure 3.3 shows the locations of the two ISW groups observed in the two radar images over the shelf, mooring SW19 (unfilled circle) and CTD 01 (unfilled triangle) near transect AA', and mooring SW31 (filled circle) and CTD 02 (filled triangle) near transect BB'.

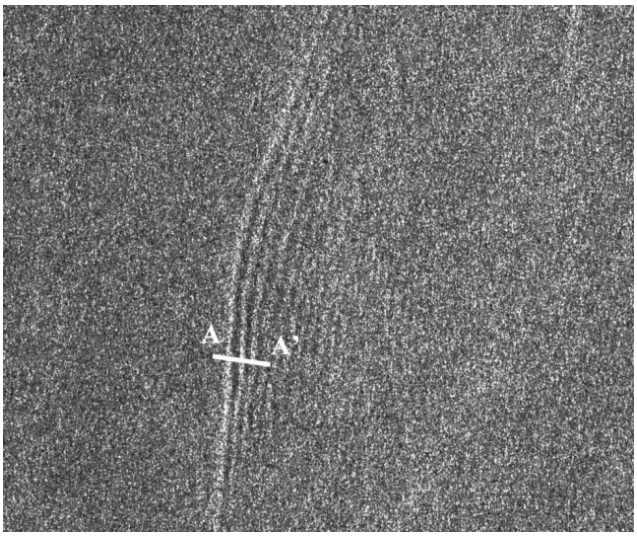

Figure 3.1. The RADARSAT-1 SAR image taken at 10:43 UTC August 20, 2006. Transect AA' is marked by a white line.

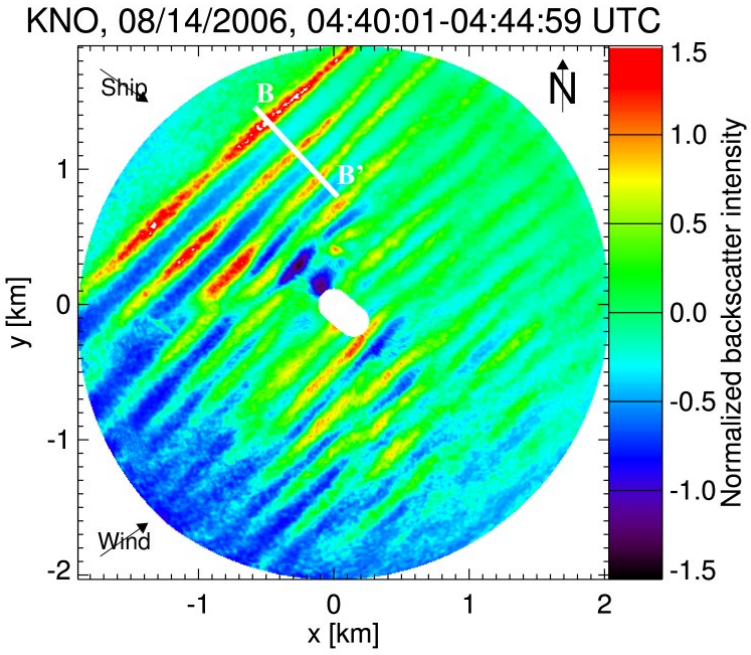

Figure 3.2. Average of 5-min sequence of backscatter power images recorded by marine radar on board R/V Knorr starting at 04:40:01 UTC August 14, 2006. Transect BB' is marked by a white line.

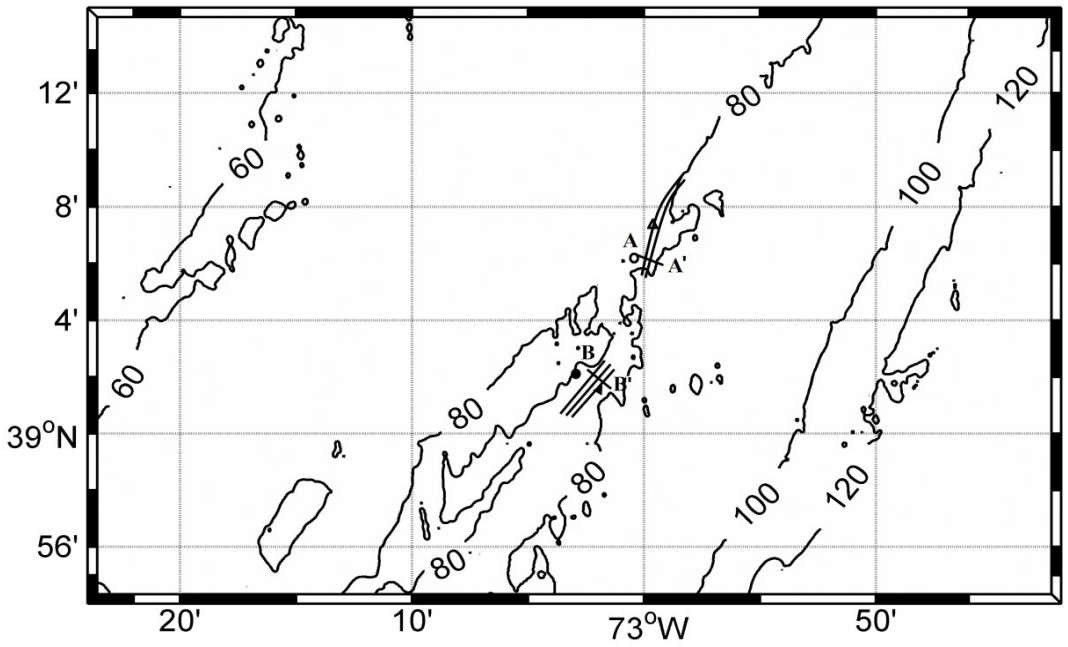

Figure 3.3. Two ISW groups over the bathymetry contours. Two intensity transects AA' and BB' are marked by solid lines. Mooring SW19 and CTD 01 near AA' are marked by an unfilled circle and an unfilled triangle, respectively. Mooring SW31 and CTD 02 near BB' are marked by a filled circle and a filled triangle, respectively.

3.3 Methodology

The higher-order KdV equation (Stanton and Ostrovsky, 1998) with a cubic nonlinearity term to describe large amplitude ISWs is given by

$$\eta_t+(c_0+\alpha\eta+\alpha_1\eta^2)\eta_x+\beta\eta_{xxx}=0. \quad (3.1)$$

where η is the vertical displacement of the interface between two layers of water. The water in the MAB can be well approximated as a two-layer stratified system with an upper layer thickness of h_1 and a lower layer thickness of h_2. h_1 is defined as the depth where the maximum buoyancy frequency (BF) is. $\Delta\rho$ and ρ are the density difference and the average density of the two layers. The parameters α, β, and α_1 in (3.1) are given by

$$\alpha = \frac{3c_0(h_1-h_2)}{2h_1h_2} \tag{3.2a}$$

$$\beta = \frac{c_0h_1h_2}{6} \tag{3.2b}$$

$$\alpha_1 = \frac{3c_0}{{h_1}^2{h_2}^2}\left[\frac{7}{8}(h_2-h_1)^2 - \left(\frac{{h_2}^3+{h_1}^3}{h_1+h_2}\right)\right] \tag{3.2c}$$

where

$$c_0 = \sqrt{\frac{g\Delta\rho}{\rho}\frac{h_1h_2}{h_1+h_2}} \tag{3.3}$$

is linear wave speed of the ISWs.

The higher-order KdV has a soliton solution:

$$\eta = -\frac{\alpha}{\alpha_1}\frac{\nu}{2}\left[\tanh\left(\frac{x-ct}{\Delta}+\delta\right) - \tanh\left(\frac{x-ct}{\Delta}-\delta\right)\right] \tag{3.4}$$

where

$$\delta(\nu) = \frac{1}{4}\ln\left(\frac{1+\nu}{1-\nu}\right) \tag{3.5a}$$

$$\Delta = \sqrt{\frac{-24\alpha_1\beta}{\alpha^2\nu^2}} \tag{3.5b}$$

$$c = c_0 - \frac{\alpha^2\nu^2}{6\alpha_1} \tag{3.5c}$$

and ν is a nonlinearity parameter in the range $0 < \nu < 1$.

Two-dimensional ISWs can be described by a stream function ψ. The stream function is a product of linear wave speed and the vertical displacement, $\psi = c_0\eta\phi(z)$, where ϕ is a normalized vertical structure function. The horizontal velocity induced by the ISWs is given by

$$u = -c_0\eta\frac{\partial\phi}{\partial z} \tag{3.6}$$

Peak locations of the ISW-induced deviations of NRCS from its equilibrium value σ_0 satisfy

$$\frac{\partial \sigma_1}{\partial x} = 0 \tag{3.7}$$

Based on the theoretical model used by Zheng et al. (2001), σ_1 is proportional to the ISW-induced current gradient. From (3.6), we can also conclude that

$$\sigma_1 \sim \frac{\partial \eta}{\partial x} \tag{3.8}$$

As a result, the p-p distance is the same as the distance between the maximum current convergence and divergence. The higher-order KdV equation does not have an explicit solution for this distance, but it can be found by using a simple numerical iteration scheme. Then a relationship between the p-p distances and ISW amplitudes can be established. We can easily determine the p-p distances from ISW signatures on radar images and estimate ISW amplitudes based on the relationship. This same method can be easily applied to the ISWs described by the KdV, ILW, or BO equations.

The radar imaging model used in Zheng et al. (2001) is a simple Bragg model. It assumes symmetric source terms for positive and negative deviations of the Bragg wave intensity from equilibrium and does not consider effects from longer waves. This results in symmetric positive and negative modulations of the image intensity over symmetric convergent and divergent regions of an ISW's surface current field. In the real world, ISW signatures on the continental shelf are known to have three types, as summarized by da Silva et al. (1998): Similar positive and negative backscatter variations, predominant negative variations, and predominant positive variations from the mean background level. Brandt et al. (1999) studied the effect of wind speed and direction on ISW signatures based on a composite surface model (Romeiser et al., 1997; Romeiser and Alpers, 1997).

We will use the same composite model to examine the effect of longer waves and of different wind directions on p-p distances.

For the model, the mandatory input files define surface current and wind fields. The optional file used in this study is frame speed. For ISW simulations, an additional input file defines the frame speed of a moving frame of reference in which the current field is quasi-stationary. This frame speed is equal to the phase velocity of the ISW. Using the frame speed file, the model integrations take place from a moving frame point of view; that is, the frame speed vector will be subtracted from each given current vector to account for the apparent mean current in the moving system. Besides the three input files, we need to specify radar frequency, radar polarization, incidence angle and radar look direction to run the radar signature simulation.

Figure 3.4a shows near-surface velocities induced by an ISW with an amplitude of 13 m, traveling in a water depth of 80 m with an upper layer depth of 20 m using (3.6). The distance between the maximum current convergence and divergence is 175 m. The radar parameters used in our model are listed as follows: The radar frequency is 5.3 GHz, the incidence angle is 45°, and the polarization is HH. The relative angle between the propagation direction of ISW and radar look direction is 0°. We run the simulation for a wind speed of 7 m/s and three relative angles between the propagation direction of ISW and wind direction 0°(solid line), 90°(dashed line), and 180°(dash-dotted line) (Figure 3.4). Simple Bragg model results, comparable to the one considered in Zheng et al. (2001), are shown in Figure 3.4b. The positive and negative modulations are of the same

magnitude, and the p-p distances for the three wind directions are all 175 m. The picture gets more complicated when we account for spatially varying effective winds at the moving water surface and corresponding asymmetries in the Bragg wave modulation, as shown in Figure 3.4c. For the wind direction of 90°, the positive and negative modulations have a similar magnitude, like in the previous case. The peaks are at the same locations as in Figure 3.4b, and the p-p distance is also 175 m. However, the negative modulation dominates when the wind direction is 0°, while positive modulation dominates when the wind direction is 180°. The peaks for both cases do not occur at the locations of the maximum convergence and divergence anymore; the p-p distances for wind directions of 0° and 180° are 165 m and 185 m. Finally, Figure 3.4d shows the full composite surface model results. Accounting for contributions of longer waves to the radar signatures, we see some phase shifts of the positive and negative signatures against the direction of propagation of the ISW, but the shapes of the signatures are still similar as in the previous case. The p-p distances for wind directions of 0°, 90°, and 180° are 185 m, 190 m, and 230 m, respectively. Except for the wind direction of 180°, the p-p distances are very close to the distance between the maximum current convergence and divergence. Based on these results, we think it is justified to use the p-p distance as a parameter for ISW amplitude estimations and to assume that the p-p distance is usually close to the distance between maximum surface current convergence and divergence.

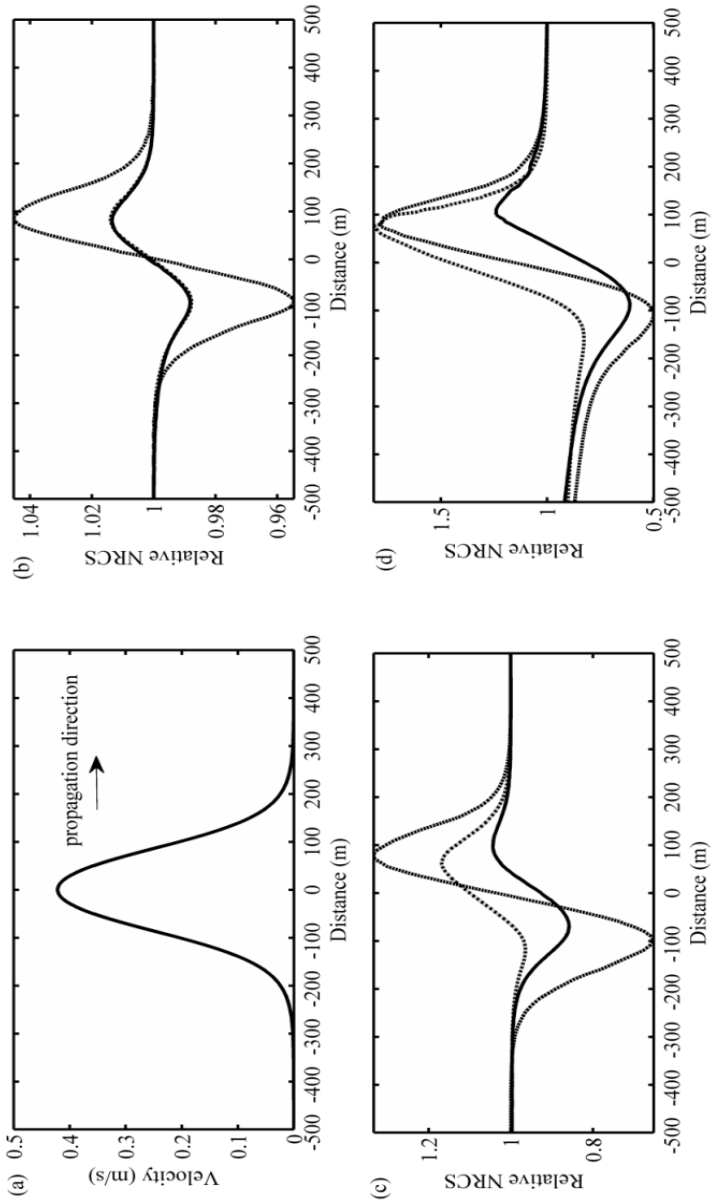

Figure 3.4. Analysis of the p-p distance as function of wind direction according to three different radar imaging models. (a) Horizontal near-surface current in wave propagation direction; (b) corresponding NRCS modulation according to a simple Bragg model with symmetric source terms for the wave-current interaction; (c) NRCS modulation according to a Bragg model with more realistic source terms; (d) NRCS modulation according to a complete composite surface model. The radar frequency is 5.3 GHz, the incidence angle is 45°, and the polarization is HH. The relative angle between the propagation direction of ISWs and radar look direction is 0°. Wind speed is 7 m/s, and relative angles between the propagation direction of ISWs and wind direction are 0°(solid line), 90°(dashed line) and 180°(dash-dotted line).

3.4 Validation

3.4.1 Environmental parameters

The BF and density profiles obtained from the two CTD casts are shown in Figure 3.5. h_1, ρ, and $\Delta\rho$ are estimated from these profiles. The upper layer depths are estimated to be 20 m for AA' and 12.5 m for BB'. The water depths are about 80 m for AA' and 75 m for BB'. All the environmental parameters listed in Table 3.1 are used in the higher-order KdV equation for a two-layer stratified system to estimate the ISW amplitudes of the two groups.

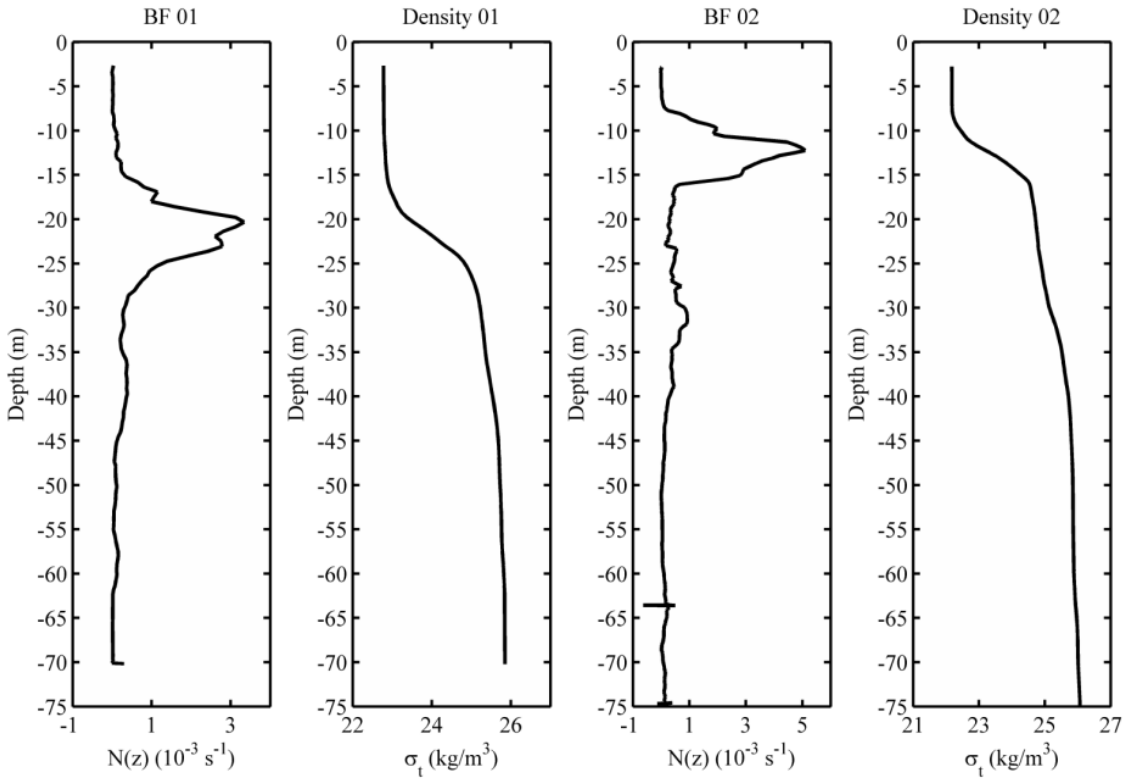

Figure 3.5. Background BF and density profiles from CTD 01 and 02.

Table 3.1. The environmental parameters used in the higher-order KdV equation in a two-layer stratified system for the two ISW groups.

Transect	h (m)	h_1 (m)	ρ (kg/m^3)	$\Delta\rho$ (kg/m^3)
AA’	80	20	1024.1	2.8
BB’	75	12.5	1023.8	3.2

3.4.2 The p-p distance versus ISW amplitude

Using the higher-order KdV equations of section 3.2 and environmental parameters listed in Table 3.1, we can solve the relationship between p-p distance and ISW amplitude numerically. The result is shown in Figure 3.6, which also includes results for the KdV, ILW, and BO equations for comparison. We can see that the amplitude estimations based on the KdV and higher-order KdV equations agree well for very small amplitudes less than 2 m, and then have a growing discrepancy for larger amplitudes. Similarly, the ILW and BO equations agree well at very small amplitudes, and then have a growing discrepancy for larger amplitudes. The KdV, ILW, and BO equations have the same trend, showing a monotonic relationship between p-p distance and ISW amplitude, which is also demonstrated by Zheng et al. (2001). ISW amplitudes increase with decreasing p-p distances. Among these three equations, the ILW equation gives the largest amplitude estimation. For the higher-order KdV equation, ISW amplitudes show a new pattern: They first increase, reach the turning point, and then decrease with decreasing p-p distances. As a result, a p-p distance corresponds to two possible amplitude estimations. One gives a small amplitude and the other gives a large amplitude.

In other words, it cannot directly tell if the amplitude is large or small based on a single observed p-p distance. A selection rule is proposed to choose from the two possibilities. ISWs usually rank in order in a group, which means the soliton amplitudes decrease from front to back. If p-p distances of ISW signatures increase across the wave group, this fits the relationship shown in the upper part of Figure 3.6a and the smaller amplitude estimation should be chosen. Conversely, if p-p distances of ISW signatures decrease across the wave group, this fits the relationship shown in the lower part of Figure 3.6a and the larger amplitude estimation should be chosen.

Intensity transects of AA' and BB' after averaging parallel to the wave crest are shown in Figure 3.7. The p-p distances for A1 and A2 are determined as 175 m and 150 m and the p-p distances for B1, B2, and B3 are determined as 143 m, 135 m, and 113 m, respectively. The p-p distances of the group of A1, A2 and the group of B1, B2, and B3 both decrease across the wave groups, such that the large amplitude estimation should be chosen based on the selection rule. The amplitudes based on the higher-order KdV equation are estimated to be –13.3 m and –10.8 m for A1 and A2, and –16.6 m, –16.3 m, and –15.2 m for B1, B2, and B3, while the conventional KdV equation gives estimations of –2.8 m and –3.8 m for A1 and A2, and –1.4 m, –1.5 m, and –2.2 m for B1, B2, and B3 (Figure 3.6). The ILW equation gives estimations of –5.1 m and –6.8 m for A1 and A2, and –4.1 m, –4.5 m, and –6.1 m for B1, B2, and B3. The BO equation gives estimations of –3.5 m and –4.1 m for A1 and A2, and –1.7 m, –1.8 m, and –2.1 m for B1, B2, and B3. The negative sign here means the ISW type is depressive.

As shown in Figure 3.8, the amplitudes estimated from the temperature records at SW19 and SW31 during the ISW passages are about –12.0 m and –11.5 m for A1 and A2, and –14.6 m, –13.5 m, and –12.7 m for B1, B2, and B3. Amplitude estimations from *in situ* measurements and theoretical predictions from the KdV, ILW, BO, and higher-order KdV equations are listed in Table 3.2. We can see that the higher-order KdV estimations agree well with the *in situ* data, while all the other equations give highly underestimated estimations.

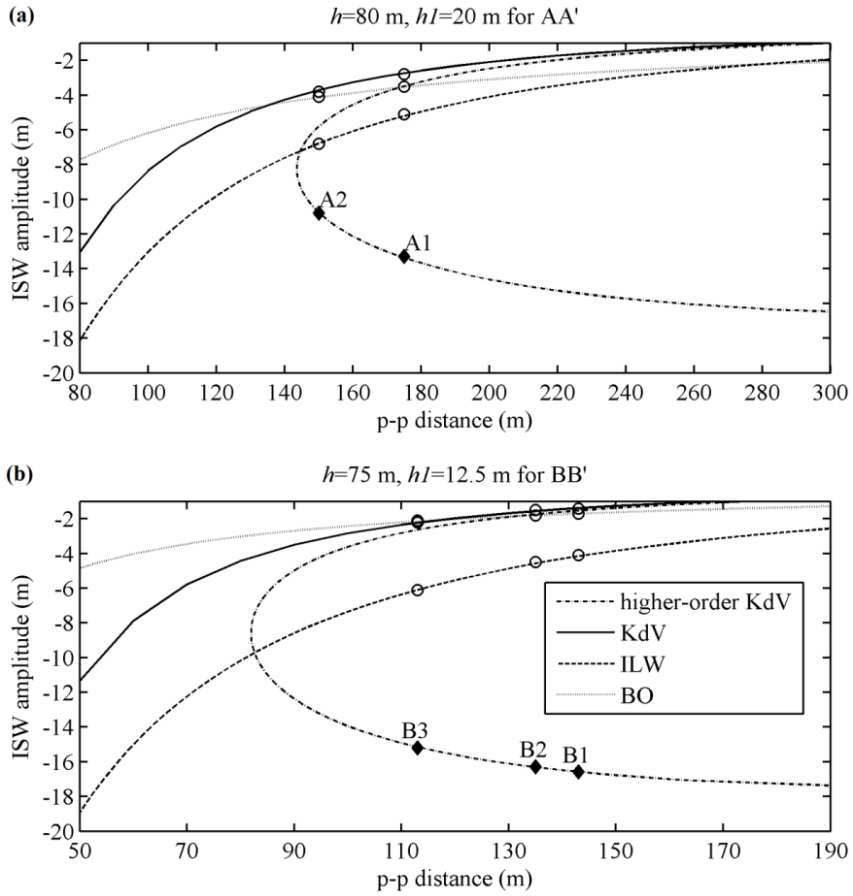

Figure 3.6. The theoretical relationship between p-p distance and ISW amplitude for the higher-order KdV equation (dash-dotted line), the KdV equation (solid line), the ILW equation (dashed line), and the BO equation (dotted line) with the environmental parameters listed in Table 3.1 for AA' (a) and BB' (b).

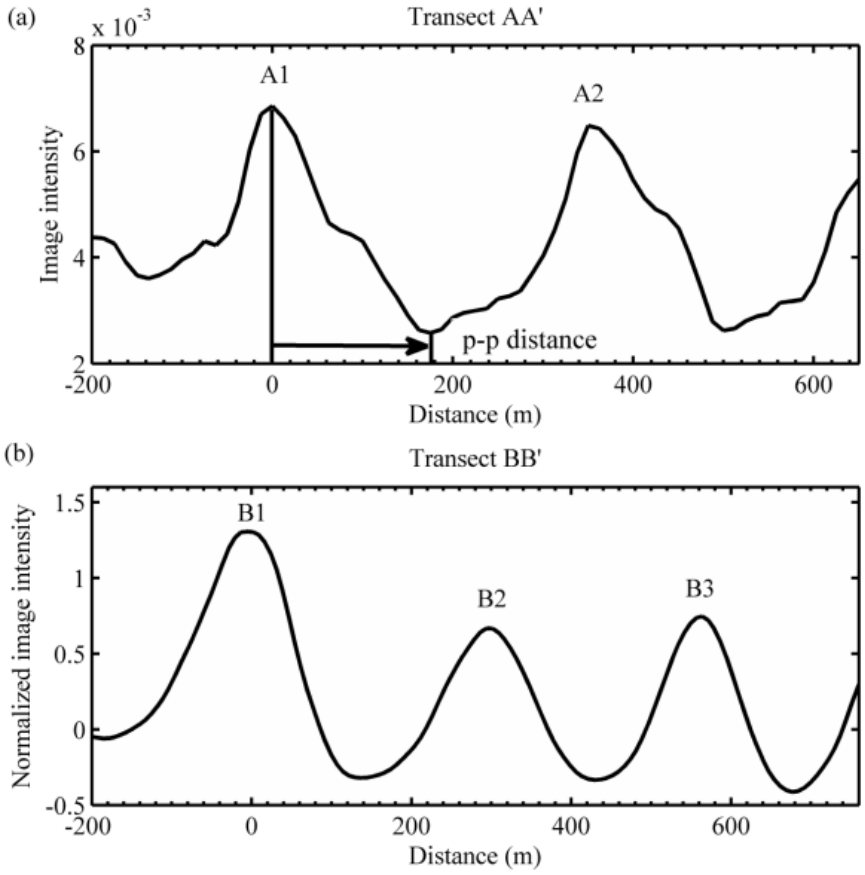

Figure 3.7. Image intensity profiles along transects AA' (a) and BB' (b). The black arrow shows the definition of the p-p distance.

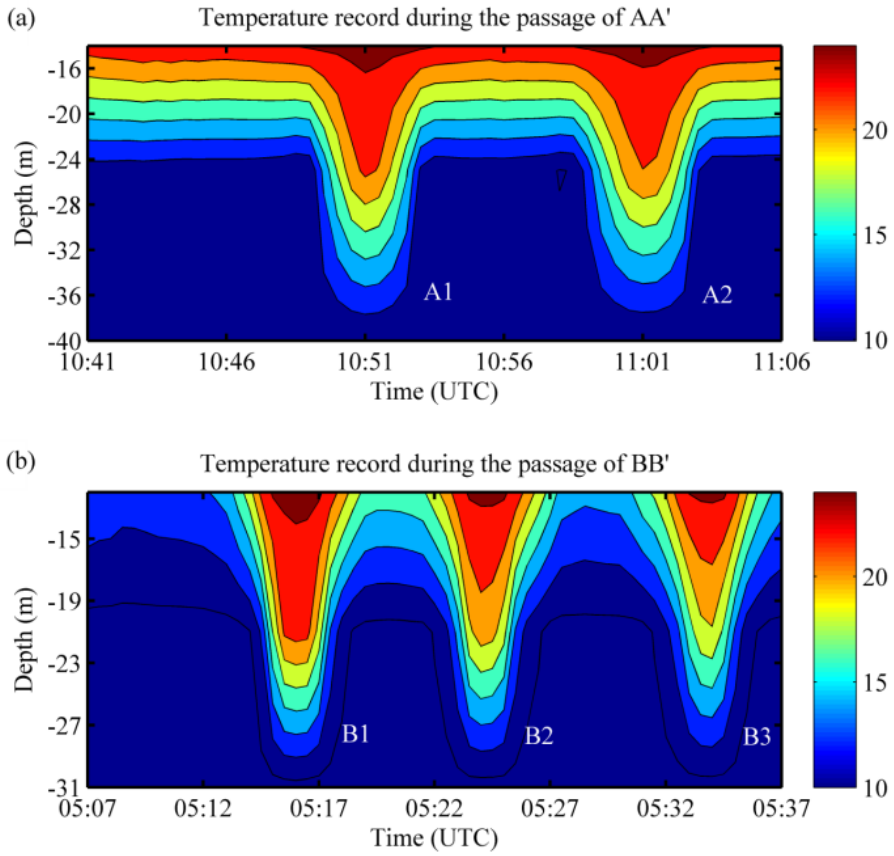

Figure 3.8. Temperature records from SW19 during the ISW passages of A1 and A2 (a) and temperature record from SW31 during the ISW passages of B1, B2, and B3 (b).

Table 3.2. Amplitude estimations from *in situ* data and theoretical predictions for the higher-order KdV, KdV, ILW, and BO equations.

ID (m)	A1	A2	B1	B2	B3
p-p distances	175	150	143	135	113
$\eta_{\text{in-situ}}$	–12.0	–11.5	–14.6	–13.5	–12.7
$\eta_{\text{higher-order KdV}}$	–13.3	–10.8	–16.6	–16.3	–15.2
η_{KdV}	–2.8	–3.8	–1.4	–1.5	–2.2
η_{ILW}	–5.1	–6.8	–4.1	–4.5	–6.1
η_{BO}	–3.5	–4.1	–1.7	–1.8	–2.1

3.4.3 Sensitivity to environmental parameters

In a two-layer stratified system, different water depths, upper layer depths, average densities and density differences can alter α, β, and α_1 in (3.1). Therefore, we need to examine the sensitivity of ISW amplitude estimations to these environmental parameters. The dependence of the relationship of p-p distances and amplitudes on the upper layer depth h_1, total water depth h, average densities ρ, and density differences $\Delta\rho$ is shown in Figure 3.9. We only show the higher-order KdV and KdV equations in Figure 3.9 because the ILW and BO equations have very similar trends with the KdV equations. Figure 3.9a shows that the estimated amplitudes change with the upper layer depth. For the higher-order KdV equation, the estimated amplitudes in the small amplitude category increase, while those in the large amplitude category decrease with increasing h_1 for a certain p-p distance. For the KdV equation, the estimated amplitudes increase with the upper layer depth. Figure 3.9b shows that the estimated amplitudes change with the total water depth as well. For the higher-order KdV, the estimated amplitudes for a given p-p distance increase with h both in the small amplitude and large amplitude category. For the KdV equation, the estimated amplitudes also increase with the upper layer depth. Average densities and density differences almost have no effect on the relationship of p-p distances and ISW amplitudes (Figure 3.9c and 3.9d). As illustrated in Figure 3.9, our amplitude estimations are sensitive to both water depth and upper layer depth. Since for AA' and BB', the water depth is known so that the following discussion focuses on the sensitivity of amplitude estimations to the upper layer depth. Figure 3.10 shows the

amplitude estimations in the large amplitude category for different upper layer depths for these two cases. We can see the greater upper layer depths give smaller amplitude estimations. When the p-p distances get closer to the turning point, amplitude estimations are more sensitive to the upper layer depth, such that 1 m change in the upper layer depth can result in amplitude change about 3 m for B3 in Figure 3.10b. If certain p-p distance does not have an intersection with the curve, the amplitude estimation of the closest point, which is actually the turning point, will be used such as A2 in Figure 3.10a. For p-p distances that are far from the turning point, amplitude estimations are much less sensitive, such that a 1 m change in the upper layer depth results in a very small amplitude change of less than 1 m (Figure 3.10). In the central MAB, the stratification increases continuously from mid-April to August. The pycnocline deepens slowly in the water column from early to late summer (Castelao et al, 2008; Castelao et al., 2010). The SAR imaging time was 7 days before CTD 01 and the marine radar data were collected 14 days before CTD 02. Considering that the pyconcline deepens slowly in the summer, the upper layer depths for AA' and BB' can be assumed to be about 1 m and 2 m less than the CTD estimations. The p-p distances of AA' are very close to the turning point and the p-p distances of BB' are a little further from it. As a result, for an upper layer depth of 19 m, the amplitude estimations for A1 and A2 become -14.4 m and -12.7 m, which is 1.1 m and 1.9 m larger than the original estimations. For B1, B2, and B3, an upper layer depth of 10.5 m yields amplitudes of -16.8 m, -16.7 m, and -15.8 m, which is only 0.2 m, 0.4 m, and 0.6 m larger than the original estimations.

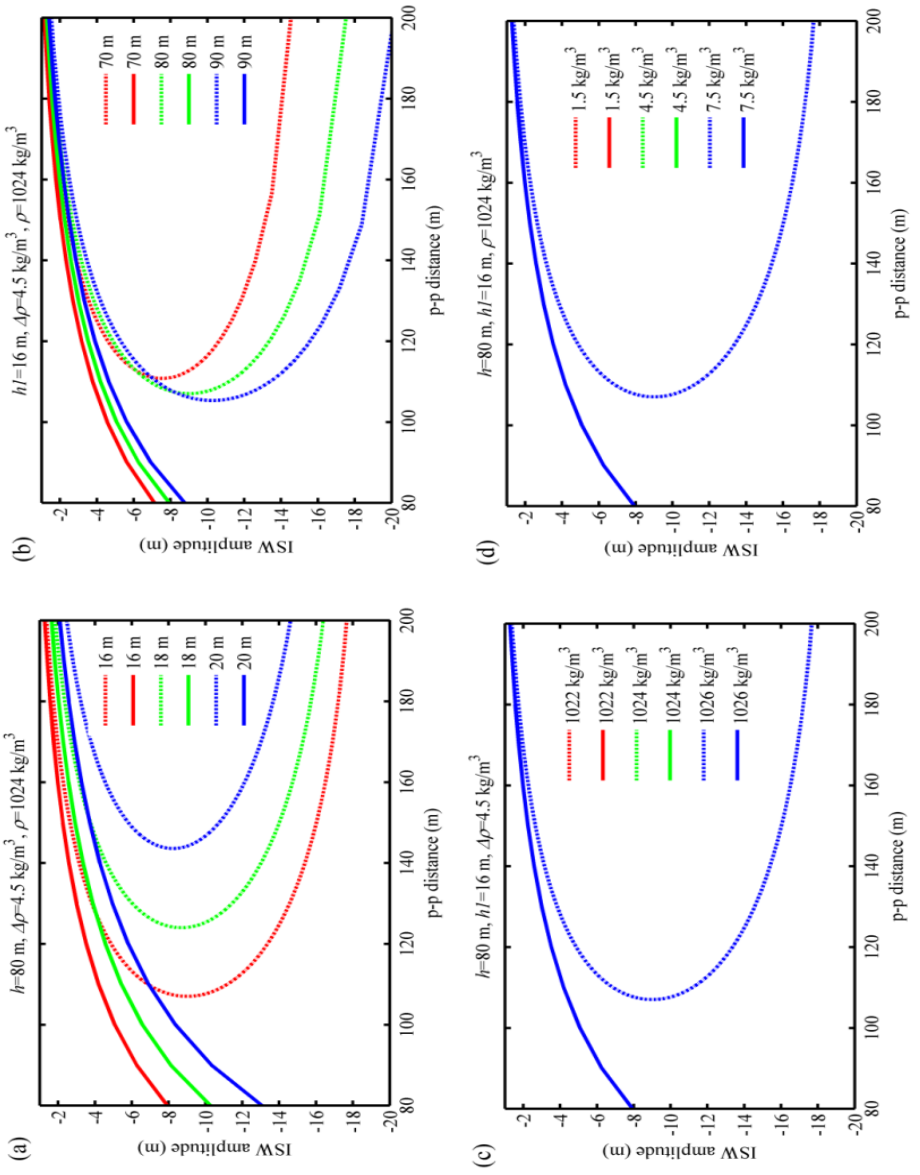

Figure 3.9. Sensitivities of the relationship between p-p distance and amplitude with different upper layer depths (a), total water depths (b), average densities (c), and density differences (d). The solid lines have been obtained with the KdV equation and the dash-dotted lines have been obtained with the higher-order KdV equation.

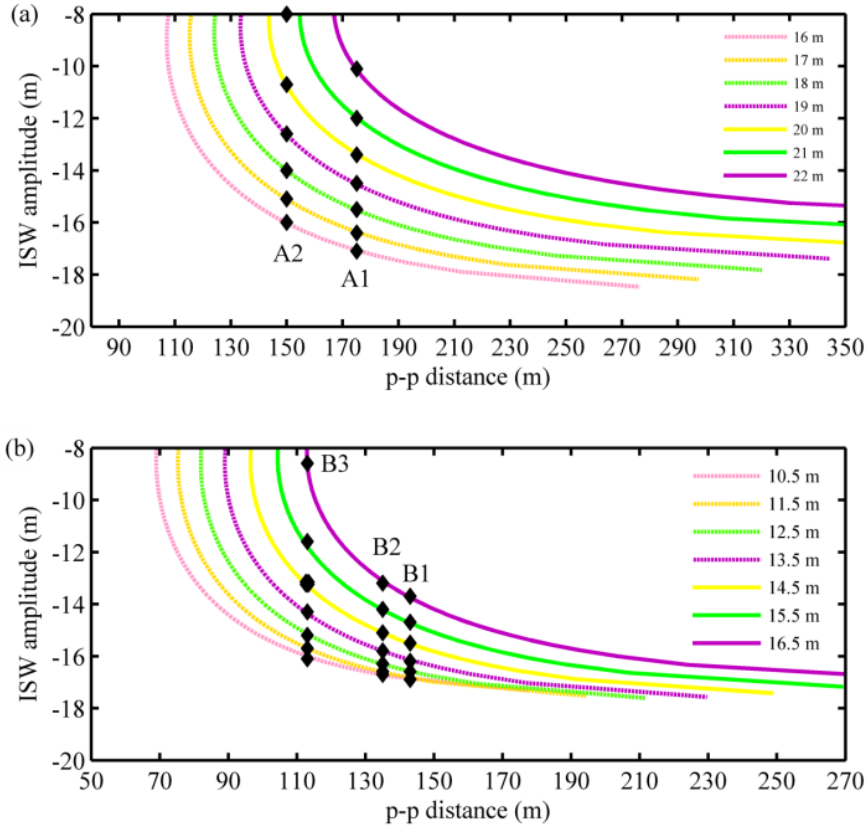

Figure 3.10. Sensitivities of the relationship between p-p distance and amplitude with different upper layer depths for A1 and A2 (a) and for B1, B2, and B3 (b). The black diamonds indicate the amplitude estimations for the five solitons for different upper layer depths.

3.5 Conclusions

The ISWs in the MAB have a wide range of amplitudes from about 2 m to over 20 m in a shallow water of 80 m depth or less. The method of estimating ISW amplitudes from observed p-p distances in radar signatures, proposed by Zheng et al. (2001), gives very small estimations for the large amplitudes in this area if the relationship according to the KdV, ILW, and BO equations is used. To obtain more realistic amplitude estimations, we have used the higher-order KdV equation for large amplitude ISWs in a two-layer

stratified system and developed a selection rule to resolve the ambiguity of the resulting ISW amplitude estimations. The amplitude estimations based on the higher-order KdV equation show a different pattern than those based on the KdV, ILW, and BO equations. ISW amplitudes first increase and then decrease with decreasing p-p distances, which results in two possible amplitude solutions for a given p-p distance. If the p-p distances of ISWs decrease across a wave group, we choose the larger amplitude estimation. Conversely, if the p-p distances of ISWs increase across the wave group, we choose the small amplitude estimation. This way we obtain the largest amplitude for the leading ISW, which is consistent with theory and observations. We have demonstrated the method and the selection rule by analyzing two ISW groups respectively observed in a SAR image and marine X-band radar data and at nearby moorings. Our amplitude estimations for both groups fall into the large-amplitude category. The results agree well with the *in situ* data. If we use the KdV, ILW, or BO equations, it gives much smaller amplitude estimations than the *in situ* data. Our method breaks the impression that a smaller p-p distance always corresponds to a larger ISW amplitude (based on the KdV equation) and establishes the new idea that a longer p-p distance can relate to a larger ISW amplitude when the amplitudes are very large. As a conclusion, the method we have developed based on the higher-order KdV equation is a relatively easy and reliable way to estimate large-amplitude ISWs in our study area. It will improve our understanding of ISW signatures in radar images.

3.6 Discussion

The presented method of relating the p-p distances measured from radar images to ISW amplitudes depends strongly on the choice of the theoretical models describing wave dynamics. Weakly nonlinear KdV-type theories have played a primary role in remote sensing study of ISWs because of their simplicity, among which the KdV equation has been demonstrated to have a wide validity to describe ISWs even out of its theoretical applicable range. However, ISW waveforms described by these KdV-type equations get narrower when wave amplitudes increase and do not fit with the observations of large amplitude ISWs from *in situ* measurements or laboratory experiments. A useful variant of the KdV equation is the higher-order KdV equation, which includes a cubic nonlinearity term. It does a good job of capturing the characteristics of the highly nonlinear ISWs, whose waveforms get broaden and develop a flat crest. We can see that, in order to get accurate amplitude estimation, it is necessary to know which weakly nonlinear model is suitable to describe ISWs in the study area, which requires *in situ* measurements of ISWs and stratification conditions. For example, in the MAB, we know that there are many ISWs with much smaller amplitudes from *in situ* measurements and such ISWs would be described well with the ILW equation. If the p-p distances increase across the wave group, we can determine that this wave group has much smaller amplitudes and estimate their wave amplitudes using the ILW equation. In this case, if we have a distribution map of ISW signatures from SAR images, the

bathymetry map, and the upper layer depth distribution map, we can easily develop an ISW amplitude distribution map in the MAB.

Among those weakly nonlinear models, there are two-layer models as well as continuously stratified models. Two-layer models are the simplest ones because they only need accurate upper layer depths to estimate the wave amplitude as we show in section 3.3.3. However, the stratifications in some areas cannot be approximated well by two-layer models and we have to use the continuously stratified models instead. In this case, we need the stratification profiles measured near the locations of ISWs in radar images to estimate wave amplitudes accurately. Besides the stratification condition, ambient velocity shear may also have great impact on nonlinear ISWs. In some area, we need to consider it otherwise ISW amplitudes and phase velocity estimation will not be accurate (Pan and Jay, 2009; Wang and Pawlowicz, 2011). In summary, we need to keep in mind that ISWs in different areas have different characteristics resulting from different weakly nonlinear model, stratification condition, and ambient shear. However, one thing is confirmed that the higher-order KdV equation have a different trend with the other KdV-type equations no matter what the environment parameters are. A longer p-p distance can relate to a larger ISW amplitude when the amplitudes are very large. One thing I need to point out here is that the cubic nonlinearity coefficient in the two-layer higher-order KdV equation is always negative while for more general stratification and ambient shear, the cubic nonlinearity coefficient can be either positive or negative, which make the solitary wave solution more complicated.

Although the higher-order KdV equation can capture the characteristics of the highly nonlinear ISWs, finite-amplitude theories are still required to describe these characteristics accurately. Miyata (1985, 1988) and Choi and Camassa (1999) each derived two-layer models with full nonlinearity while including the first-order weakly dispersion. The solitary wave solutions of the Miyata-Choi-Camassa (MCC) equations also get broaden and grow a flat crest with increasing amplitudes. Helfrich and Melville (2006) showed the comparison of the wave shape and properties of the two-layer higher-order KdV and MCC equations and the result showed they agreed quite well when the upper layer water depth is between 0.4 and 0.6 of the whole water depth and their discrepancies grew rapidly outside this range. MCC equations are in good agreement with the laboratory observations of large amplitude ISWs (Michallet and Barthelemy, 1998). Vlasenko et al. (2000) studied the structure of large amplitude ISWs using a stationary model based on the incompressible two-dimensional Euler equations in the frame of the Boussinesq approximation and the properties of large amplitude ISWs described by the Euler model have the same trend as described by the two-layer MCC model. As a result, the two-layer MCC model would be a good alternative method to the higher-order KdV model to estimate large wave amplitude from radar images.

CHAPTER 4 UNDERSTANDING INTERNAL WAVE-WAVE INTERACTION PATTERNS OBSERVED IN SATELLITE IMAGES

Many internal wave-wave interaction patterns have been observed in satellite images. However, very few studies have been made on understanding these patterns. Internal wave interactions may result in exceptionally high amplitudes in the interaction zone, which in turn pose threats to underwater structures. In this chapter, we analyze the characteristics of interaction patterns observed in satellite images of the MAB, such as internal wave phase shifts and amplitude changes. Based on these characteristics, the patterns are categorized into four different types: Mach interaction; regular interaction with prominent positive phase shifts and an amplitude decrease in the interaction zone; regular interaction with prominent negative phase shifts and an amplitude increase in the interaction zone; wave interactions without phase shifts. We provide a detailed analysis of one observed interaction pattern within each category, and compare our findings with existing analytical and numerical models for two-soliton interaction. One important result from this qualitative study of interaction patterns is that the patterns alone can be used to deduce how the amplitude changes in the potentially hazardous interaction zone. This study thus demonstrates that high resolution satellite images can provide a useful and efficient means of studying internal wave-wave interaction.

4.1 Background

Internal wave packets propagating in the ocean often interact with each other. The resulting internal wave-wave interaction pattern is a common and interesting feature

observed frequently in satellite images, both SAR and optical images in partly cloud-free condition. When internal wave trains have propagation directions that are very close to each other, they often merge to form an extended packet. When their propagation directions are not very close to each other, some interaction patterns show prominent phase shifts, while some other patterns show no phase shifts and indicate that interactions have very few effects on internal wave packets. Studying these interaction patterns is not a trivial task, not only because of the complex dynamics involved but also because of very few available geophysical observations. For example, ship radar data have been approved to be useful to follow one internal wave packet and study its evolution (Lund et al., 2013); however, in the case of an internal wave interaction, marine radar's small coverage makes it difficult to observe the complete interaction pattern. *In situ* data are very expensive and limited to point measurements, which makes it impossible to catch the phase shifts due to an interaction. As a result, satellite imagery is the best and most cost-effective data source to observe and study internal wave interaction patterns. A few satellite images show very complicated interaction patterns of three interacting wave packets or even more. In this study, for simplicity, we will focus on the interactions of two internal wave packets only.

In satellite images, we observe many internal wave interaction patterns. However, only very few studies have been made on understanding the internal wave dynamics behind these patterns. Hsu et al. (2000) observed the nonlinear internal wave-wave interaction in a RADARSAT-1 ScanSAR Wide image, but they did not focus on

analyzing the interaction characteristics. Chen et al. (2011) used the theory of resonant interaction of two internal wave packets based on the KP equation to explain special patterns exhibited in a MODIS image in the SCS, providing a mechanism for boosting internal wave amplitudes. Xue et al. (2012) investigated qualitatively the phase shifts and amplitude changes associated with regular interaction patterns visible in satellite images in the MAB using the KP model.

During the SW06 experiment, 14 interaction patterns were observed in satellite images of the MAB. We categorize them into four different types based on the characteristics the patterns exhibit: Mach interaction (1/14); regular interaction with prominent positive phase shifts and an amplitude decrease in the interaction zone (6/14); regular interaction with prominent negative phase shifts and an amplitude increase in the interaction zone (4/14); wave interactions without phase shifts (3/14). In this chapter, we analyze one interaction pattern from each category in detail. The goal is to determine the patterns' characteristics, compare them with results obtained from existing two-soliton interaction models, and identify means of relating the observed patterns to the interior ocean dynamics associated with the interactions.

This chapter is organized as follows: In section 4.2, existing theoretical studies of solitary wave interactions are presented. In section 4.3, we give satellite observations used in this study. Section 4.4 shows and analyzes four different interaction patterns we observe and compares them with the existing analytical and numerical studies.

Conclusions are presented in section 4.5. Section 4.6 discusses deep water soliton interactions and large amplitude wave interaction using the higher-order KP equation.

4.2 Theoretical background

Mode-1 internal waves can be treated as solitary-like, thus internal wave interactions can be studied as solitary wave interactions. Miles (1977 a, b) presented a comprehensive theoretical study of small-amplitude shallow water solitary wave interactions. Generally, one can distinguish between three broad types of interaction: regular interaction, Mach interaction, and resonant interaction. In the following, we introduce the relevant interaction variables and summarize Miles' criteria of distinction. In a two-layer stratified ocean, assume that the pre-interaction amplitudes of two long internal waves, normalized by the upper layer depth, are η_1 and η_2, and both are much smaller than 1.

Regular interaction is to be expected when

$$\sin^2\frac{\psi}{2} < \psi_- \text{ or } \sin^2\frac{\psi}{2} > \psi_+, \tag{4.1}$$

where ψ is the pre-interaction angle between the two internal wave propagation directions, and $\psi_\mp = \frac{3}{4}\left(\sqrt{\eta_1} \mp \sqrt{\eta_2}\right)^2$. For regular interactions, the post-interaction wave crests are parallel to the pre-interaction wave crests ($\psi = \psi_p$), and the amplitudes of the post-interaction waves are the same as the pre-interaction waves' ($\eta_{1,2} = \eta_{1p,2p}$). Note that we use a subscript "p" to denote post-interaction variables.

Mach interaction is to be expected when

$$\psi_- < \sin^2\frac{\psi}{2} < \psi_+. \tag{4.2}$$

For interactions where $\eta_1 = \eta_2$, the post-interaction angle is given by ψ_p=$2\sqrt{3\eta_{1,2}}$. It is only dependent on the incoming wave amplitudes and is usually much larger than the pre-interaction angle ψ. The length of the Mach stem, the merged front in the interaction zone, linearly increases with time. The post-interaction amplitudes, given by $\eta_{1p,2p} = (\psi / 2\sqrt{3\eta_{1,2}})^2 \eta_{1,2}$, are much smaller than those before the interaction.

Resonant interaction should occur when

$$\sin^2 \frac{\psi}{2} = \psi_- \text{ or } \sin^2 \frac{\psi}{2} = \psi_+. \tag{4.3}$$

The merged front grows infinitely and no post-interaction waves can be seen. This is essentially a three-wave interaction. In the following, we will disregard this type and only focus on two-soliton interactions.

In the real world, the normalized internal wave amplitudes sometimes do not satisfy Miles' small amplitude requirement. Tanaka (1993) examined large amplitude wave interactions with $\eta_{1,2} = 0.3$ by numerical simulation. The critical ψ for Mach interaction is 75°, which is much smaller than Miles' prediction of 108° for this amplitude. Regular interaction happens for any ψ larger than the critical value. We expect that the critical ψ for Mach interaction decreases with a larger wave amplitude. Note that Tanaka studied an obliquely incident solitary wave by a vertical wall, so that the incidence angle and the reflection angle in his paper are half of ψ and ψ_p used here, respectively. Another difference between the two studies is that Tanaka's ψ_p decreases

with ψ, while Miles' theory gives a constant angle. Also, Tanaka's $\eta_{1p,2p}$ are smaller than $\eta_{1,2}$, but larger than in Miles' theory. Finally, Tanaka's step angle (ψ_s), which is determined from a pair of imaginary lines drawn along the edges of the merged fronts, is used to describe the merged front's growth rate. It is smaller than Miles' prediction. Tanaka concludes that large amplitudes tend to prevent the Mach interaction from happening. Even when Mach interaction happens, it has characteristics of both a Mach and a regular interaction when compared with Miles' theory. The first quantitative study of oblique interactions of internal waves was carried out by Wang and Pawlowicz (2012). They used time sequences of photogrammetrically rectified oblique images obtained from a circling aircraft and simultaneous water column data of the wave structure to study internal wave interactions. The normalized amplitudes in their study area are greater than 0.75. According to that study, the likelihood of Mach interaction for waves with large amplitudes is overestimated by Miles' theory. In other words, the patterns satisfying Miles' Mach interaction criteria were observed to exhibit the characteristics of regular interactions. Their findings thus confirm Tanaka's numerical results. Therefore, if an observed interaction pattern satisfies Miles' Mach interaction criteria, but the post-interaction angle and wave amplitudes are very close to the pre-interaction ones, we treat the pattern as a regular interaction.

The KdV equation is often used to describe internal waves. However, for two obliquely interacting solitons, the 2-D KdV equation describing nonlinear dispersive internal waves, known as the KP equation, is more appropriate. Peterson and van Groesen

(2000, 2001) have explicitly studied the two-soliton interaction by decomposition into single solitons and interacting soliton using the KP equation. Peterson et al. (2003) used the KP model to study shallow water soliton interaction and suggested it as a possible model for extreme waves. Their paper provides a detailed analysis of the phase shifts and amplitude change in the interaction zone due to the interaction. Also, they provide an analytical two-soliton solution, which is a stable-stage solution for an existing interaction area. In the following, we will make use of it for studying regular interaction patterns.

The KP equation describing nonlinear dispersive internal wave is given by:

$$(\eta_t + c_0\eta_X + c_1\eta\eta_X + c_2\eta_{XXX})_X + \frac{c_0}{2}\eta_{YY} = 0 \tag{4.4}$$

Its analytical solution is usually constructed on the basis of the canonical form:

$$(u_t - 6uu_x + u)_x + 3u_{yy} = 0 \tag{4.5}$$

The two equations can be converted into each other through a coordinate transform.

In the following, we focus on (4.5) for its generality. The two-soliton solution for (4.5) reads

$$u(x, y, t) = 2\frac{\partial^2}{\partial x^2}\ln\theta \tag{4.6}$$

where $\theta = 1 + e^{\varphi_1} + e^{\varphi_2} + A_{12}e^{\varphi_1}e^{\varphi_2}$, $\varphi_{1,2} = k_{1,2}x + l_{1,2}y + \omega_{1,2}t$ are phase variables, and $\kappa_1 = (k_1, l_1)$, $\kappa_2 = (k_2, l_2)$ are the wave vectors of the incoming solitons. The "frequency" $\omega_{1,2}$ can be found from the dispersion relation of the linearized KP equation:

$$P\left(k_{1,2},\ l_{1,2},\ \omega_{1,2}\right) = k_{1,2}\omega_{1,2} + k_{1,2}^4 + 3l_{1,2}^2 = 0 \tag{4.7}$$

Upon interaction, the two solitons undergo a phase shift: $\Delta_{12} = -\ln A_{12}$. Without losing generality, we assume t=0, then

$$A_{12} = -\frac{P(k_1-k_2,l_1-l_2,\omega_1-\omega_2)}{P(k_1+k_2,l_1+l_2,\omega_1+\omega_2)} = \frac{\lambda^2-(k_1-k_2)^2}{\lambda^2-(k_1+k_2)^2} \tag{4.8}$$

where $\lambda = {l_1}/{k_1} - {l_2}/{k_2}$. For a nonzero interaction angle, the interaction may have positive or negative phase shifts (if $A_{12} > 1$ and $0 < A_{12} < 1$, respectively). The amplitudes of the two incoming solitons are given by $u_{1,2} = 1/2{k_{1,2}}^2$. The two-soliton solution can be decomposed into a sum of two incoming solitons s_1, s_2 and the interaction soliton s_{12} (Peterson and van Groesen 2000, 2001):

$$u = s_1 + s_2 + s_{12} \tag{4.9}$$

when the counterparts s_1, s_2 and s_{12} are defined as

$$s_{1,2} = \frac{A_{12}^{1/2} k_{1,2}^2 \cosh(\varphi_{2,1}+\ln A_{12}^{1/2})}{\Theta^2} \tag{4.10}$$

$$s_{12} = \frac{(k_1-k_2)^2+A_{12}(k_1+k_2)^2}{2\Theta^2} \tag{4.11}$$

with $\Theta = cosh[(\varphi_1 - \varphi_2)/2] + A_{12}^{1/2} cosh[(\varphi_1 + \varphi_2 + \ln A_{12})/2]$

Regular interactions described by the KP equation have two categories: (1) Negative phase shifts when $0 < A_{12} < 1$, which results in an amplitude increase in the interaction zone. It typically occurs for interactions between solitons with comparable amplitudes. (2) Positive phase shifts when $A_{12} > 1$, which results in an amplitude decrease in the interaction zone. It typically occurs for interactions between solitons with large amplitude differences. The two categories show different patterns. The first one has a merged front in the interaction zone and thus looks similar to Mach interaction. The second one differs

in that it does not have a merged front in the interaction zone. In this study, we compare the characteristics of the observed Mach interaction pattern with Tanaka's findings and simulate the other three observed interaction patterns using the KP model.

4.3 Satellite observations

The SW06 experiment took place on the continental shelf off the coast of New Jersey. Many satellite images, including ENVISAT ASAR, ERS-2 SAR, RADARSAT-1 SAR, SPOT-2/4 HRV-PAN images, were received and processed at the CSTARS. The SAR images have a resolution of 25 m and the SPOT HRV-PAN images have a resolution of 10 m. The internal wave interaction signatures in satellite images are sometimes too vague to study due to high wind speeds or other atmospheric effects. However, we observed 14 clear two internal wave packets interaction patterns in the satellite images from the SW06 experiment. In this study, we analyze one interaction pattern from each category. The other 10 images of interaction patterns and the corresponding sketches of the interaction patterns of the two leading solitons are listed by the dates in the Appendix C. Figure 4.1 shows the locations of four interaction patterns cut from the original images over the bathymetry. The rectangle (a) outlines the location of the case of Mach interaction shown in Figure 4.2; The rectangle (b) the case of regular interaction with prominent positive phase shifts and an amplitude decrease in the interaction zone shown in Figure 4.5; The rectangle (c) the case of regular interaction with prominent negative

phase shifts and an amplitude increase in the interaction zone shown in Figure 4.7; The rectangle (d) the case of interaction without phase shifts shown in Figure 4.11.

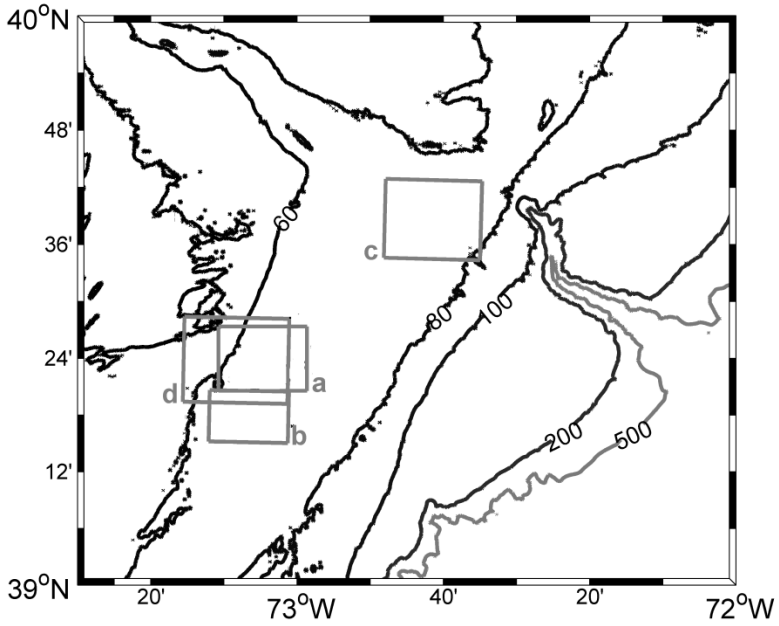

Figure 4.1. Locations of four observed interaction patterns over the bathymetry of the MAB. The rectangles (a), (b), (c), and (d) outline the locations of the cases shown in Figures 4.2, 4.5, 4.7, and 4.11, respectively.

4.4 Internal wave interaction patterns

4.4.1 Mach interaction

We can see two internal wave packets propagating in different directions in Figure 4.2. When such two packets interact with each other for a period of time, merged fronts are generated in the interaction zone. This results in an interlocked, zipper-like interaction pattern observed in the SPOT-4 HRV-PAN image taken on August 05, 2006. Although satellite images are snapshots only, the information from the spatial domain can be transferred to the temporal domain of the interaction process. Intuitively, the pattern

implies the first waves in both packets interact first, and then the second waves in both packets interact. Starting from the third waves, interactions become more complicated. The post-interaction wave from the second wave-wave interaction interacts with the third wave in the right packet, and then the resulting post-interaction wave interacts with the third wave in the left packet. Here we make the simplification that the third waves in both packets directly interact with each other. Moreover, since the interactions in the rear are not as strong as in the front, we only focus on the interactions of the first three waves in both packets.

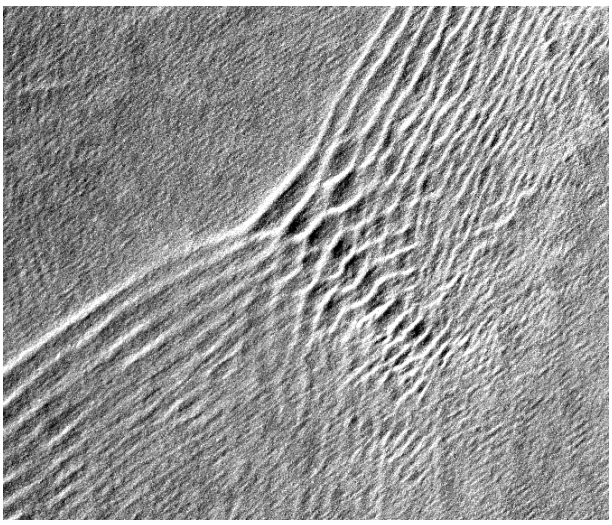

Figure 4.2. An interlocked, zipper-like internal wave interaction pattern observed in the SPOT-4 HRV-PAN image (17.6 km × 12.1 km) taken on August 05, 2006 (the rectangle (a) in Figure 4.1).

Figure 4.3(a) shows a sketch of the interaction pattern of the first three waves in both packets. Packet A stands for the wave packet on the left and packet B stands for the wave packet on the right. The pre-interaction waves in packet A are marked as A1, A2, and A3 orderly, and the corresponding post-interaction waves are labeled a1, a2, and a3. In the

same way, the pre-interaction waves in packet B are marked as B1, B2, and B3 orderly and the corresponding post-interaction waves are labeled b1, b2, and b3. The merged front generated due to the interaction of A1 and B1 is marked as AB1. The interaction sketch of the first waves is shown in Figure 4.3(b). The angles between A1 and AB1, B1 and AB1 are approximately 27° and 18°, respectively. The interaction angle between packets A and B is approximately 45°. Wave crests after the interaction are not parallel to their pre-interaction orientations. The angle between a1 and AB1 is approximately 38°, and the angle between b1 and AB1 is approximately 40°. The post-interaction angle between a1 and b1 is approximately 78°. The lengths of the first three merged fronts are 2.80 km, 1.43 km, and 0.98 km. The length increases with time, which is an unsteady interaction, indicating a Mach interaction (Miles 1977 a, b; Porubov et al., 2005; Wang and Pawlowicz, 2012). The merged front in a Mach interaction is named Mach stem. Assuming the amplitude difference of the first and the second waves in the packet is very small, we can retrieve the temporal development of the first Mach stem from the spatial snapshot of the first two Mach stems. This is accomplished by connecting the edge points of the first two Mach stems on both sides and extending the lines backward, yielding the cross point, which is estimated to be the generation location of the Mach stems (Figure 4.4). The step angle is estimated to be approximately 37° on the left side and 40° on the right side. The distance from the first Mach stem to the original point is 1.80 km. Similarly, the step angle calculated based on the second and third Mach stem is approximately 20° on the left and 23° on the right. The travel distance is 1.73 km.

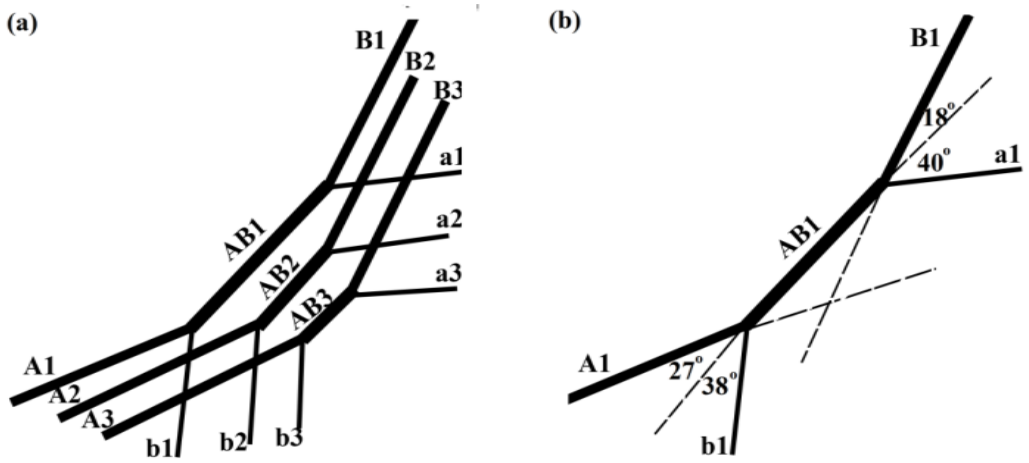

Figure 4.3. (a) Sketch of the interactions of the first three waves in both packets shown in Figure 4.2. (b) Sketch of the interaction of the first waves in both packets (ψ=45°, ψ_p=78°), the extended dashed lines of A1 and B1 are the approximate wave crest locations without interaction.

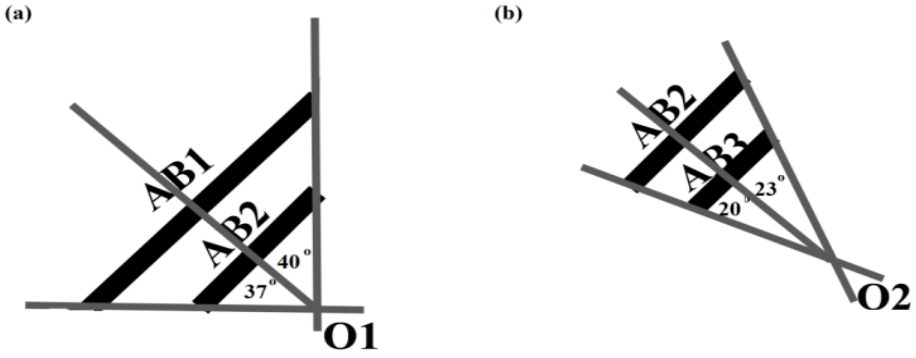

Figure 4.4. The lines connect the edges of the merged fronts on both sides to get the generation point for (a) the first and second merged fronts and (b) the second and third merged fronts.

Most internal waves observed in the SW06 experiment have amplitudes between 4 and 10 m and wave speeds between 0.62 and 0.80 m/s (Shroyer et al., 2011). For satellite-observed ISWs, we can determine their phase speeds accurately if *in situ*

measurements are nearby or two successive internal wave groups from the same origin are observed in a single image. Unfortunately, internal waves in the observed interaction patterns satisfy neither of these two conditions. However, since the satellite images were collected during the SW06 experiment, it is highly likely that the satellite-observed internal waves lie in the same phase speed range. As a result, the time of developing the first Mach stem is estimated between 37 and 48 min. Similarly, the time of developing the second one is between 36 and 46 min. In our study area, the upper layer depth is about 15 m at the time the image was taken. As a result, the normalized wave amplitude is between 0.27 and 0.67. According to Miles' theory, the post-interaction angle should be between 102° and 162°, which is much larger than the observed 78°. The post-interaction normalized amplitude is 0.05. The step angle is between 10° and 20°. Obviously, the internal wave amplitudes in the MAB do not satisfy the small amplitude requirement for Miles' theory. Tanaka (1993) studied Mach interaction at a normalized wave amplitude of 0.3, which lies within our amplitude range in the MAB. The post-interaction angle and normalized amplitude in Tanaka's simulation is found to be 85° and 0.09, respectively. The step angle is 6°. By looking at the image brightness, we can qualitatively say that the post-interaction amplitude is much smaller and the Mach stem amplitude is larger than the pre-interaction wave amplitude. Our observation agrees more with Tanaka's numerical results except for the step angle. Since internal wave amplitudes usually rank in order, the length of the first Mach stem at the location of the

second Mach stem may have been longer than we measure from the image, which would result in the step angle being larger than our estimate.

Based on Tanaka's numerical results and Wang and Pawlowicz (2012)'s finding that the likelihood of Mach interaction is overestimated by Miles' theory, we think that the large amplitudes in the MAB tend to prevent the Mach interaction from occurring. Therefore, if the post-interaction angle and amplitudes are very close to the pre-interaction ones in an observed interaction pattern in our study area, we treat it as a regular interaction.

4.4.2 Regular interactions

During the SW06 experiment, another clear interaction pattern is observed in the SPOT-2 HRV-PAN image taken on August 17, 2006 (Figure 4.5). The brightness signatures of the internal waves decrease in the interaction zone, which indicates that the wave amplitude also decreases. Figure 4.6(a) shows a sketch of the interaction pattern of the first three waves in both packets. Packet C stands for the wave packet on the left, and packet D stands for the wave packet on the right. The naming rules for the pre- and post-interaction as well as wave crests in the interaction zone are the same as in Figure 4.3. The interaction process is illustrated in Figure 4.6(b) using the first waves in both packets. The pre-interaction angle, between C1 and D1, is approximately 37°, and the post-interaction angle, between c1 and d1, is approximately 42°. The two angles are very close to each other so the waves C1 and D1 have a regular interaction. The post-interaction wave c1 continues to interact with the second wave D2 in the right

packet. The resulting post-interaction wave cc1 then interacts with the third wave D3, which results in the post-interaction wave ccc1. Similarly, the post-interaction wave d1 continues to interact with the second wave C2 in the left group, which results in the post-interaction wave dd1. The hexagonal pattern resulting from the interaction is shown in Figure 4.6(c), which agrees with the pattern found from periodic solutions to the KP equation (Hammack et al., 1995).

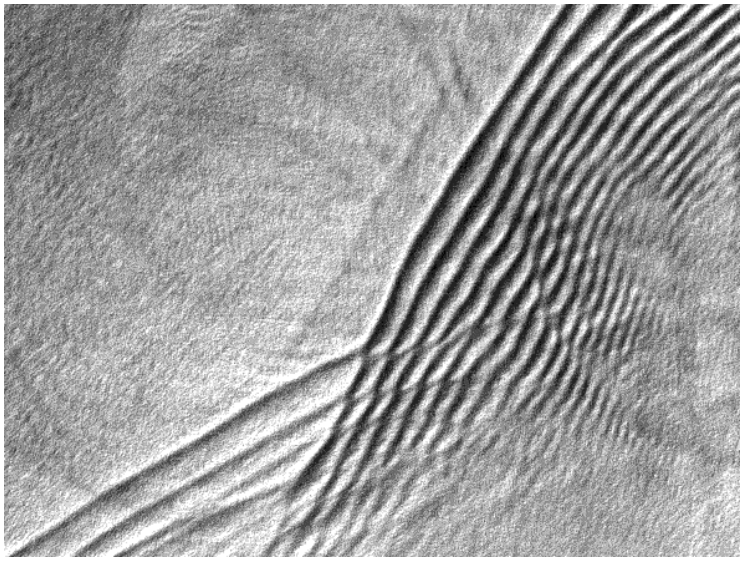

Figure 4.5. Internal wave interaction pattern observed in the SPOT-2 HRV-PAN image taken on August 17, 2006 (15.5 km × 10.0 km) in the MAB (the rectangle (b) in Figure 4.1).

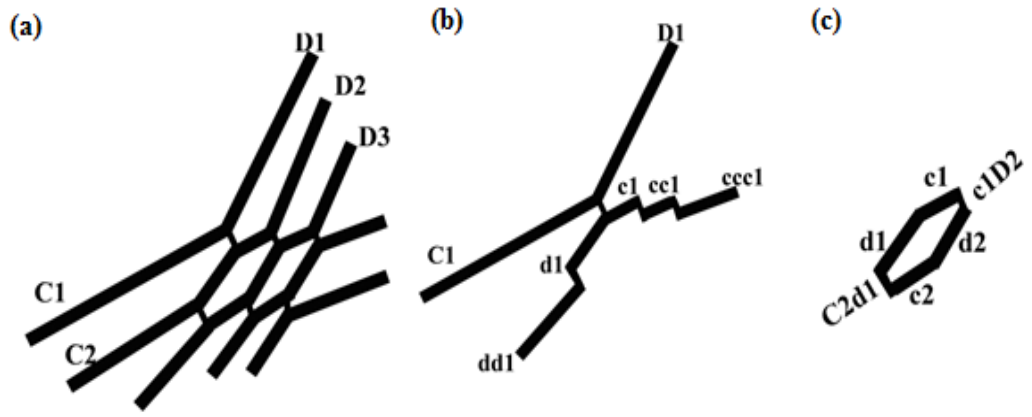

Figure 4.6. (a) Sketch of the interaction pattern of the first three waves in Figure 4.5. (b) Sketch of the interaction of the first waves in both packets (ψ=37°, ψ_p=42°). (c) The hexagonal pattern resulting from the wave interactions.

In Figure 4.7, another regular interaction pattern with an amplitude increase in the interaction zone is observed in the RADARSAT-1 image taken on August 01, 2006. The image intensity increases in the interaction zone, which indicates that the wave amplitude also increases. The interaction pattern looks similar to Mach interaction, having a merged front in the interaction zone. A sketch of the interaction of the first waves is shown in Figure 4.8. The pre-interaction angle, between E1 and F1, is approximately 49° and the post-interaction angle, between e1 and f1, is approximately 47°.

Different amplitudes of the incoming internal waves and different angles between their propagation directions will result in different interaction patterns. In the following, the two-soliton solution (4.9)-(4.11) is applied to simulate the two interaction patterns in Figures 4.5 and 4.7. In order to simulate the internal wave interaction pattern by the KP model, we need to know the amplitudes and the interaction angles of the incoming waves.

The angles for the two cases are approximately 37° and 49° measured from the images; however, only relative amplitudes of the two incoming waves are used because no *in situ* measurements are available near the observed interaction patterns. As a result, this study mainly focuses on the qualitative aspects of the interaction characteristics. All parameters needed to simulate the two observed interaction patterns are listed in Table 4.1.

Table 4.1. Parameters for the simulation of the patterns in Figures 4.5, 4.7, and 4.11.

	k_1	l_1	k_2	l_2	A_{12}
Figure 4.5	1.650	1.870	2.450	0.930	0.0044
Figure 4.7	0.579	0.238	0.579	-0.438	56.1716
Figure 4.11	0.458	0.195	0.638	-0.991	1.4519

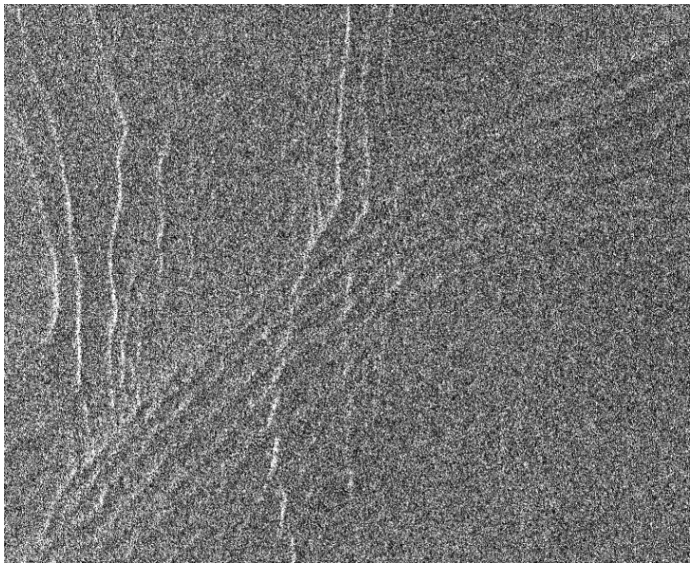

Figure 4.7. Internal wave interaction pattern observed in the RADARSAT-1 image taken on August 01, 2006 (18.8 km $\times$ 15.3 km) in the MAB (the rectangle (c) in Figure 4.1).

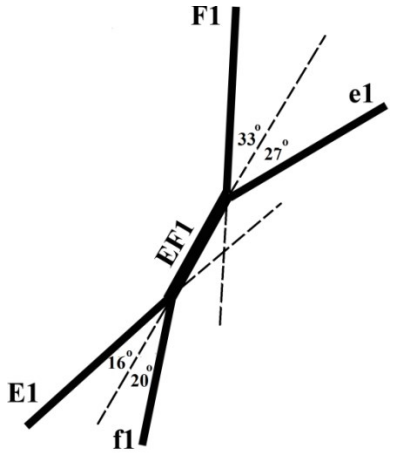

Figure 4.8. Sketch of the interaction of the first waves in Figure 4.7 (ψ=47°, ψ_p=49°), the extended dashed lines of E1 and F1 are the approximate wave crest locations without interaction.

The interaction pattern in Figure 4.5 is very clear and strong. This is partly due to the 10 m resolution of the SPOT-2 image. Figure 4.9 shows the 3-D and 2-D simulations of the two-soliton interaction pattern in Figure 4.5. For a clear view, $-u$ is used instead of u. We can see that the amplitude in the interaction zone decreases significantly when $A_{12} < 1$, a positive phase shift, which fits well with the pattern we observed in Figure 4.5. This pattern looks similar to case C discussed by Wang and Pawlowicz (2012). The case C pattern lies in Miles' Mach interaction category like the other cases in their study, but does not show any merged front in the interaction zone. Wang and Pawlowicz (2012) give two possible explanations. The first possibility is that it is a reflection problem because the wave parameters such as post-interaction amplitudes and angle are not dramatically different from those cases with merged fronts. A second possibility is that the wave amplitude or the difference in wave amplitudes may be large enough to be

above Miles' criteria of phase conservation and the case is fundamentally an oblique overtaking. Based on the KP model, we can see that this pattern is actually due to a regular interaction with an amplitude decrease in the interaction zone.

The internal wave signatures in the SAR image of Figure 4.7 are not as clear as in the optical images, but the leading solitons still show a clear interaction pattern. In Figure 4.10, we can see that the amplitude increases significantly in the interaction zone and the interaction has a negative phase shift ($A_{12} > 1$), which fits well with the pattern we observed in Figure 4.7. The two simulations shed some light on future studies of regular internal wave interaction patterns in satellite images. If we observe clear two-soliton interaction patterns in a satellite image, even if we do not know the amplitudes of the incoming solitons, we can deduce how the amplitudes change in the interaction zone, just based on the patterns themselves.

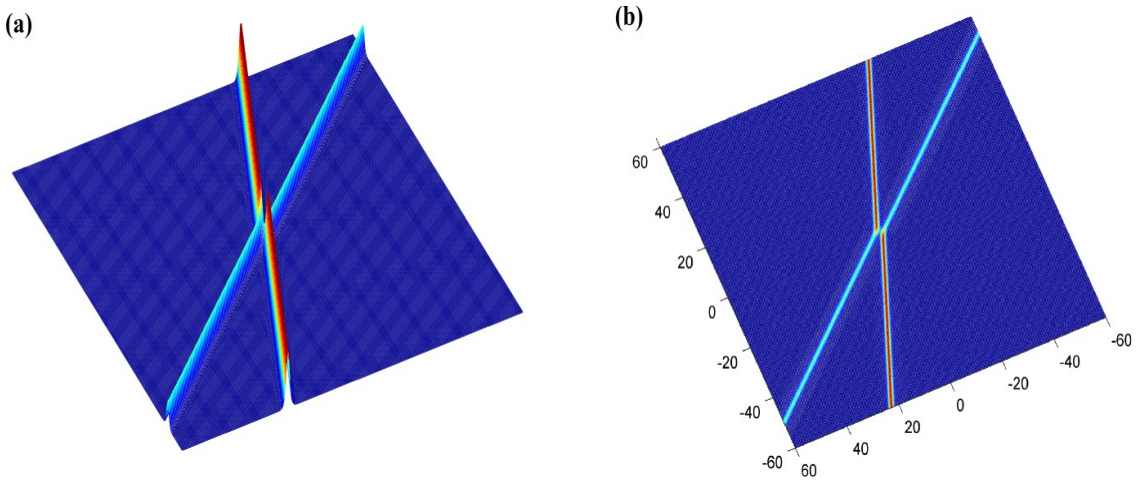

Figure 4.9. (a) Snapshot of the two-soliton solution ($-u$) for the KP equation at t=0 with the parameters for Figure 4.5 from Table 4.1. (b) Corresponding 2-D phase shift pattern.

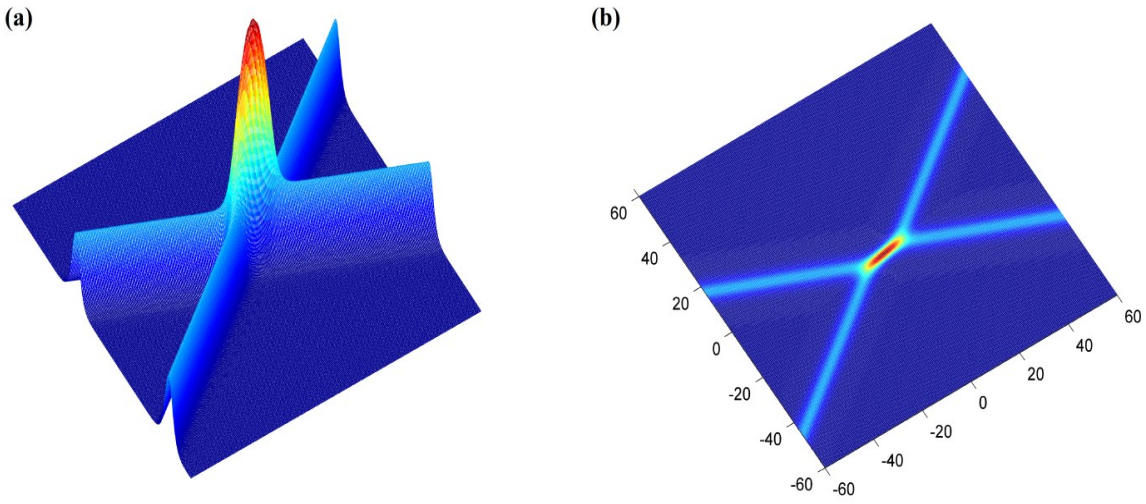

Figure 4.10. (a) Snapshot of the two-soliton solution $(-u)$ for the KP equation at t=0 with the parameters for Figure 4.7 from Table 4.1. (b) Corresponding 2-D phase shift pattern.

4.4.3 Interactions without phase shifts

Aside from all the interaction patterns with clear phase shifts that we discussed above, we also observed several interaction patterns without phase shifts. One example is found in a RADARSAT-1 image from August 13, 2006 (Figure 4.11). The interaction angle is approximately 63°. A possible reason for such pattern may be very small phase shifts at certain wave amplitudes and interaction angles, which results in the narrow width of the hump in the interaction zone that our image cannot resolve. The simulation by the KP model is illustrated in Figure 4.12. We can see that the hump in the interaction zone has a very narrow width in the 3-D interaction pattern in Figure 4.12(a) and we can barely see any phase shifts in the 2-D interaction pattern in Figure 4.12(b). Another possible reason is that the observed interaction pattern is still in the development stage and has not

reached the stable stage with clear phase shifts described by the two-soliton solution for the KP equation.

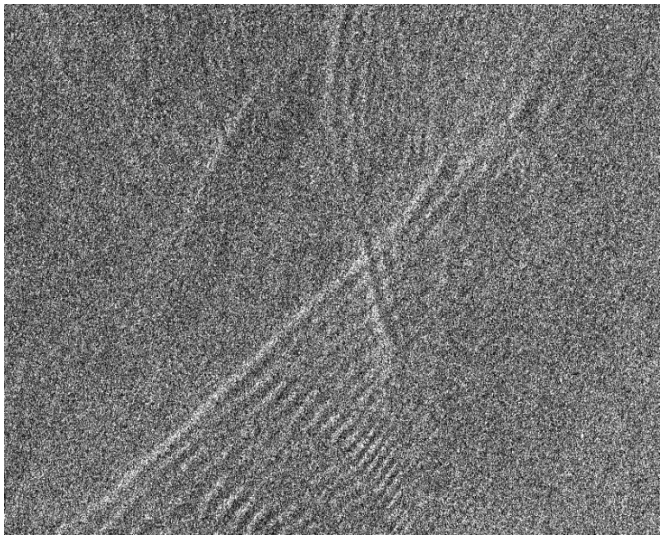

Figure 4.11. Internal wave interaction pattern without phase shifts observed on the RADARSAT-1 image taken on August 13, 2006 (20.5 km × 16.6 km) in the MAB (the rectangle (d) in Figure 4.1).

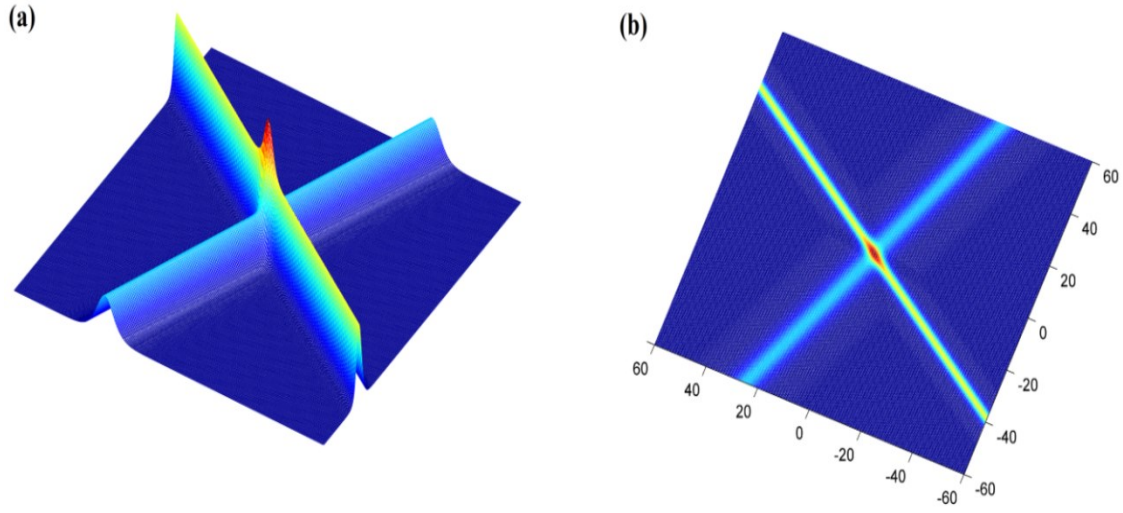

Figure 4.12. (a) Snapshot of the two-soliton solution $(-u)$ for the KP equation at t=0 with the parameters for Figure 4.11 from Table 4.1. (b) Corresponding 2-D phase shift pattern.

4.5 Conclusions

High resolution satellite images provide a useful and efficient means to study internal wave interaction patterns. Some interaction characteristics can be directly observed, such as pre-interaction and post-interaction angles, phase shifts, and qualitative amplitude changes in the interaction zone. In this study, we have observed and studied four types of internal wave interactions in the MAB. We can determine the interaction type by just examining the patterns in the images. If the post-interaction angle is much larger than the pre-interaction angle, we have a case of Mach interaction. The length of the stem increases linearly with the propagation distance. The Mach stem amplitude is larger and the post-interaction wave amplitudes are much smaller than the incoming internal wave amplitudes. If the post-interaction angle is very close to the pre-interaction angle, we have a case of regular interaction. There are two different types. One type results in a merged front in the interaction zone and looks similar to Mach interaction. The amplitude in the interaction zone is always larger than the incoming wave amplitudes. However, the post-interaction amplitudes are close to the incoming wave amplitudes and the length of the merged front is constant and does not increase with propagation distance. The other type does not result in a merged front in the interaction zone. The amplitude in the interaction zone is much smaller than the incoming wave amplitudes and the post-interaction amplitudes are close to the incoming wave amplitudes. All three types above show clear phase shifts due to the interaction. We also observe interaction patterns without prominent phase shifts. A possible explanation is that the phase shifts are very

close to zero at certain incoming wave amplitudes and interaction angles. In other words, the width of the hump in the interaction zone is too small to resolve. Another possible reason is that the observed interaction pattern is still in the development stage and has not reached the stable stage with clear phase shifts.

Much attention goes to the interactions that result in higher amplitude in the interaction zone. In Miles' theory, the maximum wave amplitude is four times that of the incoming wave. Internal waves with such high amplitudes are hazardous to underwater structures and carry large mass, momentum, and energy over a long distance.

4.6 Discussion

The analysis by Miles (1977 a, b) and Tanaka (1993) were carried out for surface solitary waves. The two-soliton solution of the canonical form of the KP equation also basically describes surface solitary wave interactions. For internal wave interactions, it is plausible that the interactions can be treated like surface solitary wave interactions since most observed ISWs are mode-1 depression waves (Grimshaw and Zhu, 1994). The patterns of surface solitary wave interactions and internal wave interaction should be qualitatively same although the dependence of phase shift on the interaction angle and incoming wave amplitudes are slightly different.

As discussed in chapter 3, ISWs can be described by the weakly nonlinear models of the KdV, ILW, and BO equations for the shallow water, intermediate water, and deep water cases respectively. For large amplitude ISWs, the higher-order KdV equation with cubic nonlinearity term is more suitable. Similarly, we should also consider deep water

internal wave interactions described by the two-dimensional BO equation and large amplitude internal wave interaction described by the higher-order KP equation. The soliton solution of the BO equation is algebraic while the soliton solution of the KdV equation is hyperbolic. They are fundamentally different; however the interaction patterns described by the BO and KdV equations are very similar (Oikawa, 1984; Matsuno, 1998; Grimshaw and Zhu, 1994). For the soliton interactions by the higher-order KP equation, Tsuji and Oikawa (2007) studied the numerical solutions for various values of the cubic nonlinearity term for the interaction patterns. The result showed the interaction property was very similar to that of the KP equation when the cubic nonlinearity term was small, however the existence of amplitude restriction for the soliton solution of the higher-order KdV equation prevented the generation of the Mach stem when the cubic nonlinearity term was large. Since some large amplitude ISWs in the MAB need to be described by the higher-order KdV equation, the regular interaction pattern without phase shifts studied in section 4.4.3 may owe its existence to the amplitude restriction discussed in Tsuji and Oikawa (2007).

In this chapter, we present a qualitative study of internal wave interactions and the patterns exhibited in the satellite images agree well with the existing theories. However, it is still a long way to get an accurate quantitative study of these interactions. First, we need to get the two-soliton solution of the KP equation describing nonlinear internal wave interaction through a coordinate transform. Second, either *in situ* measurements of amplitudes of pre-interaction waves, post-interaction waves, and the wave in the

interaction zone are needed to compare with the results of the KP model, or a method to estimate internal wave amplitudes from their signatures in satellite image needs to be developed (Xue et al., 2012). Xue et al. (2013a) developed a method based on the higher-order KdV equation to estimate large amplitude ISWs over 10 m in the MAB, but a method to estimate wave amplitude in the range of 4–10 m is still needed. For large amplitude ISWS, we need to use the higher-order KP equation instead of the KP equation. Moreover, numerical studies of internal wave interactions with different amplitudes are needed to get a better understanding of the interaction processes.

CHAPTER 5 CONCLUSIONS AND OUTLOOK

ISWs can be observed in SAR, optical, and marine X-band images. SAR and optical images are very useful to study ISW distribution, generation mechanisms, and wave-wave interaction patterns with the wide coverage while marine X-band radar images can be used to study individual ISWs evolution since the ship can follow the ISWs for some certain time period. Their signatures are all closely associated with variation of sea surface roughness despite the different imaging sensors.

During the SW06 experiment, many SAR, SPOT images, and marine X-band radar data were collected and many ISW packets and wave-wave interaction patterns were observed in the MAB. My thesis mainly addresses two things: (1) to develop a method to estimate amplitudes of large ISWs using SAR and marine X-band radar images; (2) to understand internal wave-wave interaction patterns observed in satellite images. The main conclusions are summarized as follows.

First, since some ISWs amplitudes are over 10 m in the MAB in a shallow water of 80 m depth or less, we use the higher-order KdV equation to describe such large amplitude ISWs. By adopting the method of estimating ISW amplitudes from observed p-p distances in radar signatures, proposed by Zheng et al. (2001), the results show a different pattern than those based on the KdV, ILW, or BO equation.

ISW amplitudes first increase and then decrease with decreasing p-p distances, which results in two possible amplitude solutions for a given p-p distance. I propose a selection rule to resolve the ambiguity of the resulting ISW amplitude estimations. If the p-p

distances of ISWs decrease across a wave group, we choose the larger amplitude estimation. Conversely, if the p-p distances of ISWs increase across the wave group, we choose the small amplitude estimation. This way we obtain the largest amplitude for the leading ISW, which is consistent with theory and observations. Our method breaks the understanding that a smaller p-p distance always corresponds to a larger ISW amplitude (based on the KdV equation) and establishes the new idea that a longer p-p distance can relate to a larger ISW amplitude when the amplitudes are large.

The sensitivity of the amplitude estimation to environmental parameters based on the higher-order KdV equation is also studied. The estimated amplitudes in the small amplitude category increase, while those in the large amplitude category decrease with increasing upper layer depth for a certain p-p distance. For an increasing water depth, the estimates increase both in the small and large amplitude category. The estimates donot change with the average density and the density difference. We can see the upper layer depth is the key parameter to get an accurate ISW amplitude estimation.

Second, high resolution satellite images provide a useful and efficient means to study internal wave-wave interaction patterns. We can directly observe some interaction characteristics such as pre-interaction and post-interaction angles, phase shifts, and qualitative amplitude changes in the interaction zone from the images. We can determine the interaction type by just examining the patterns in the images. If the post-interaction angle is much larger than the pre-interaction angle, we have a case of Mach interaction. The length of the stem increases linearly with the propagation distance. The Mach stem

amplitude is larger and the post-interaction wave amplitudes are much smaller than the incoming internal wave amplitudes. If the post-interaction angle is very close to the pre-interaction angle, we have a case of regular interaction. There are two different types. One type results in a merged front in the interaction zone and looks similar to Mach interaction. The amplitude in the interaction zone is always larger than the incoming wave amplitudes. However, the post-interaction amplitudes are close to the incoming wave amplitudes and the length of the merged front is constant and does not increase with propagation distance. The other type does not result in a merged front in the interaction zone. The amplitude in the interaction zone is much smaller than the incoming wave amplitudes and the post-interaction amplitudes are close to the incoming wave amplitudes. All three types above show clear phase shifts due to the interaction. We also observe interaction patterns without prominent phase shifts. A possible explanation is that the phase shifts are very close to zero at certain incoming wave amplitudes and interaction angles. In other words, the width of the hump in the interaction zone is too small to resolve. Another possible reason is that the observed interaction pattern is still in the development stage and has not reached the stable stage with clear phase shifts.

Generally speaking, internal wave-wave interaction can result either an amplitude increase or decrease in the interaction zone. When it is an amplitude increase case, the merged front is generated in the interaction zone. In Mile's theory, the maximum wave amplitude is 4 times that of the incoming wave. Since the ISW front with such large amplitude can travel for a long time, it is hazardous to underwater structures and carries

large mass, momentum, energy over a long distance. Understanding the interaction patterns can help us to know the complex dynamics involved and give some reference to underwater constructions such as the operational feasibility and safety for the offshore oil industry.

Regarding two topics studied in the thesis, future work can be done is listed as follows. First, a method to estimate amplitudes of ISWs in the range of 4 m to 10 m from their signatures in the satellite images needs to be developed. The ILW equation should be the appropriate model. If the p-p distances increase across the wave group, we can determine that this wave group has much smaller amplitudes and estimate their wave amplitudes using the ILW equation. If the p-p distances decrease across the wave group, we can determine that this wave group has much larger amplitudes and estimate their wave amplitudes using the higher-order KdV equation. In this way, a distribution map of ISW amplitudes in the MAB can be easily developed, if we know the bathymetric map and the historic upper layer depth distribution map from field experiments. It would be very useful for study ISW distribution and evolution processes. Second, a method to estimate ISW amplitudes from their signatures in SPOT images needs to be developed. Then we can estimate the pre-interaction and post-interaction ISW amplitudes of an interaction pattern based on the signatures in the images and compare with the existing analytical and numerical theory. In the other hand, numerical study of internal wave interactions with the known amplitude is needed to compare with the existing interaction

patterns observed in the satellite images and get a better understanding of the interaction processes.

APPENDIX A THE KdV-TYPE INTERNAL SOLITARY WAVE EQUATIONS IN A TWO-LAYER MODEL

A.1 The KdV equation

The KdV equation for shallow water ISWs in a two-layer flow is given by Osborne and Burch (1980) as

$$\eta_t + (c_0 + \alpha\eta)\eta_x + \beta\eta_{xxx} = 0. \tag{A.1}$$

where η is the vertical displacement of the interface between two layers of water. In two-layer stratified system, we have an upper layer thickness of h_1 and a lower layer thickness of h_2. h_1 is defined as the depth where the maximum buoyancy frequency (BF) is. ρ_1 and ρ_2 are the densities of the upper and lower layer, respectively. $\Delta\rho$ and ρ are the density difference and the average density of the two layers. The parameters α and β in (A.1) are given by

$$\alpha = \frac{3c_0(h_1-h_2)}{2h_1h_2} \tag{A.2a}$$

$$\beta = \frac{c_0h_1h_2}{6} \tag{A.2b}$$

where

$$c_0 = \sqrt{\frac{g\Delta\rho}{\rho}\frac{h_1h_2}{h_1+h_2}} \tag{A.3}$$

is linear wave speed of the ISWs

The KdV equation has a soliton solution:

$$\eta(x,t) = -\eta_0\text{sech}^2[(x-ct)/L] \tag{A.4}$$

with phase speed

$$c = c_0 - \alpha\eta_0/3 \tag{A.5}$$

and a soliton half width of

$$L = (-12\beta/\eta_0\alpha)^{1/2} \tag{A.6}$$

A.2 The ILW equation

The ILW equation for intermediate-depth ISWs in a two-layer fluid is given by Choi and Camassa (1999) as

$$\eta_t + (c_0 + \alpha\eta)\eta_x + \beta\Gamma_c[\eta_{xx}] = 0. \tag{A.7}$$

The parameters α and β in (A.7) are given by

$$\alpha = -\frac{3c_0}{2h_1} \tag{A.8a}$$

$$\beta = \frac{c_0\rho_2 h_1}{2\rho_1} \tag{A.8b}$$

where

$$c_0 = \sqrt{\frac{g\Delta\rho}{\rho}h_1} \tag{A.9}$$

with the operator Γ_c defined by

$$\Gamma_c[f] = \frac{1}{2h_2}\int_{-\infty}^{+\infty} f(x')\coth\frac{\pi}{2h_2}(x'-x)dx' \tag{A.10}$$

The solution of the ILW equation is one parameter (γ) family of solitary wave solutions:

$$\eta_{ILW}(x,t) = \frac{-\eta_0\cos^2\gamma}{\cos^2\gamma+\sinh^2((x-ct)/L_{ILW})} \tag{A.11}$$

with

$$\eta_0 = \frac{4\beta}{h_2\alpha}\gamma\tan\gamma \tag{A.12}$$

$$L_{ILW} = h_2/\gamma \tag{A.13}$$

$$c = c_0 - \frac{2\beta}{h_2}\gamma\cot(2\gamma) \tag{A.14}$$

where

$$0 \leq \gamma < \frac{\pi}{2} \tag{A.15}$$

A.3 The BO equation

The BO equation for deep water ISWs in a two-layer fluid is given by Benjamin (1967) and Ono (1975) as

$$\eta_t + (c_0 + \alpha\eta)\eta_x + \beta \frac{\partial^2}{\partial x^2}\mathcal{H}[\eta] = 0 \tag{A.16}$$

The parameters α and β in (A.16) are given by

$$\alpha = -\frac{3c_0}{2h_1} \tag{A.17a}$$

$$\beta = \frac{c_0\rho_2 h_1}{2\rho_1} \tag{A.17b}$$

where

$$c_0 = \sqrt{\frac{g\Delta\rho}{\rho} h_1} \tag{A.18}$$

with the Hilbert operator $\mathcal{H}$ defined by

$$\boldsymbol{\mathcal{H}}[f] = \frac{1}{\pi}\int_{-\infty}^{+\infty} \frac{f(x')}{x'-x}\,dx' \tag{A.19}$$

The BO equation has a soliton solution:

$$\eta_{BO}(x,t) = \frac{-\eta_0}{1+((x-ct)/L_{BO})^2} \tag{A.20}$$

where

$$L_{BO} = \frac{4\beta}{\eta_0\alpha} \tag{A.21}$$

$$c = c_0 - \alpha\eta_0/4 \tag{A.22}$$

APPENDIX B ANALYTICAL EXPRESSION FOR AN OCEAN ISW SIGNATURE IN THE SATELLITE IMAGES

The wave number spectral density of the high frequency capillary-gravity wave spectrum (Ψ) can be written in the form of (Yuan, 1997; Zheng et al., 2001; Zheng et al., 2004; Pan et al., 2007)

$$\Psi = {m_3}^{-1}\left[m\left(\frac{u_*}{c_{sw}}\right)^2 - 4\gamma^2 k_{sw}^2 \bar{\omega}^{-1} - S_{\alpha\beta}\frac{\partial U_\beta}{\partial x_\alpha}\bar{\omega}^{-1}\right]k_{sw}^{-4}, \tag{B.1}$$

Where m_3 and m are coefficients; u_* is the friction wind speed; $\bar{\omega}$, k_{sw}, and c_{sw} are the angular frequency, the wave number, and phase speed of surface waves, respectively; γ represents the viscosity. U_β denotes the velocity components of the large scale current field, and $S_{\alpha\beta}$ represents the excess momentum flux tensor. Subscripts α and β represent the horizontal coordinates (x or y).

Thus

$$S_{\alpha\beta}\frac{\partial U_\alpha}{\partial x_\beta} = \frac{1}{2}\left[\frac{\partial u}{\partial x}\cos^2\varphi + \left(\frac{\partial u}{\partial y} + \frac{\partial v}{\partial x}\right)\cos\varphi\sin\varphi + \frac{\partial v}{\partial y}\sin^2\varphi\right], \tag{B.2}$$

Where φ is the wave direction.

For the ocean surface, the radar backscatter cross section per unit area, σ_0, is given by (Plant, 1990)

$$\sigma_0(\theta)_{ij} = 16\pi k_0^2\left|g_{ij}(\theta)\right|^2\Psi(0, 2k_0\sin\theta), \tag{B.3}$$

Where θ and k_0 represent the incidence angle and wave number of radar waves, respectively; Ψ is the two-dimensional wave number spectral density of the ocean surface waves satisfying the Bragg resonant scatter condition; the indices i and j denote the polarizations of the incident and backscattered radiations, respectively; and

$g_{ij}(\theta)$ are the first-order scattering coefficients. Under HH and VV conditions, g_{ij} is in the form of

$$g_{HH}(\theta) = \frac{(\varepsilon_r - 1)\cos^2\theta}{\left[\cos\theta + (\varepsilon_r - \sin^2\theta)^{\frac{1}{2}}\right]^2}, \quad \text{(B.4)}$$

and

$$g_{VV}(\theta) = \frac{(\varepsilon_r - 1)\left[\varepsilon_r(1 - \sin^2\theta) - \sin^2\theta\right]\cos^2\theta}{\left[\varepsilon_r\cos\theta + (\varepsilon_r - \sin^2\theta)^{\frac{1}{2}}\right]^2}, \quad \text{(B.5)}$$

Respectively, where ε_r is the relative dielectric constant of seawater (Saxton and Lane, 1952; Klein and Swift, 1977).

Therefore we have

$$\sigma_0(\theta)_{ij} = 16\pi k_0^2 \left|g_{ij}(\theta)\right|^2 {m_3}^{-1} \left[m\left(\frac{u_*}{c_{sw}}\right)^2 - 4\gamma^2 k_{sw}^2 \bar{\omega}^{-1} - S_{\alpha\beta}\frac{\partial U_\beta}{\partial x_\alpha}\bar{\omega}^{-1}\right] k_{sw}^{-4} \quad \text{(B.6)}$$

where $k_{sw} = 2k_0 \sin\theta$. The first two terms of the right-hand side of (B6) represent wind inputs and viscosity dissipation, respectively. On the horizontal scale of an internal wave packet, these terms are supposed to be uniform, so they only contribute to the background of an internal wave SAR images (Zheng et al., 2001). The third term reflects effects of the internal wave. Considering the internal wave propagation direction is x, we have $\varphi = 0$, therefore the second and third terms of (B.2) are zero. Thus, taking into account the SAR look direction χ relative to the wave direction, the soliton induced radar backscatter cross section per unit area, $\sigma_{ISW}(\theta)_{ij}$, is

$$\sigma_{ISW}(\theta)_{ij} = 8\pi k_0^2 {m_3}^{-1} \left|g_{ij}(\theta)\right|^2 \cos\chi\, k_{sw}^{-4} \left[-\frac{\partial(u_{z=0})}{\partial x}\right], \quad \text{(B.7)}$$

The imaging mechanism for ISW signatures in optical images is sunglint and the signatures are also related to surface roughness. Jackson and Alpers (2010) derived the normalized sunglint radiance as

$$N_n(\vartheta, \vartheta_0, \phi, \sigma_0^2) = \frac{\rho(\tau)}{4} \frac{\left(1+\tan^2\delta\right)^2}{\cos\vartheta} \exp\left(\frac{-\tan^2\delta}{\sigma_0^2}\right), \quad \text{(B.8)}$$

where ϑ is the sensor zenith angle, ϑ_0 is the solar zenith angle, ϕ is the relative azimuth angle, σ_0 is the sea surface roughness, $\rho(\tau)$ is the Fresnel reflection coefficient of the water surface for unpolarized light, τ is the local reflection angle for specular reflection of sunlight into the sensor by a facet, and δ is the surface tilt of a facet on the surface. Equation (B.8) shows the sunglint radiance monotonically change with the sea surface roughness.

APPENDIX C INTERNAL WAVE-WAVE INTERACTION PATTERNS

There are ten internal wave-wave interaction patterns observed in satellite images but not discussed in details in Chapter 4. In this Appendix, we list these patterns and corresponding sketches by the order of imaging times and categorize them into four types of interactions in Table C.1.

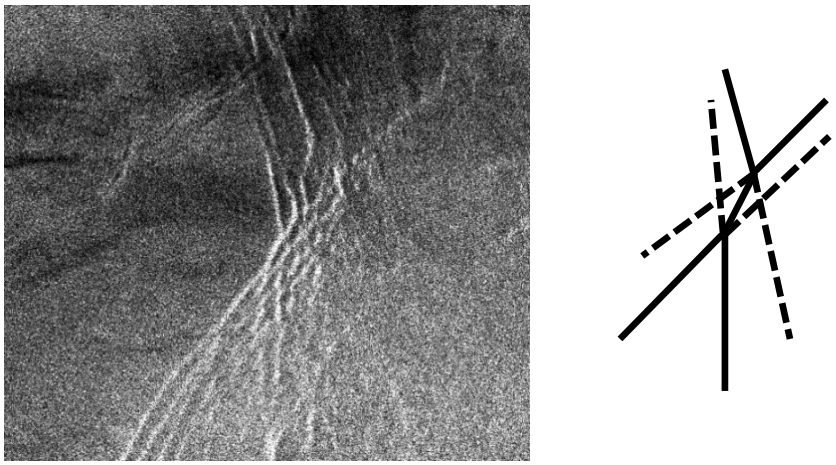

Figure C.1. An internal wave interaction pattern observed in the ENVISAT ASAR image taken on July 14, 2006 (left), and corresponding sketch of the pattern of the two leading solitons (right). Dashed lines show the approximate crest locations without interaction.

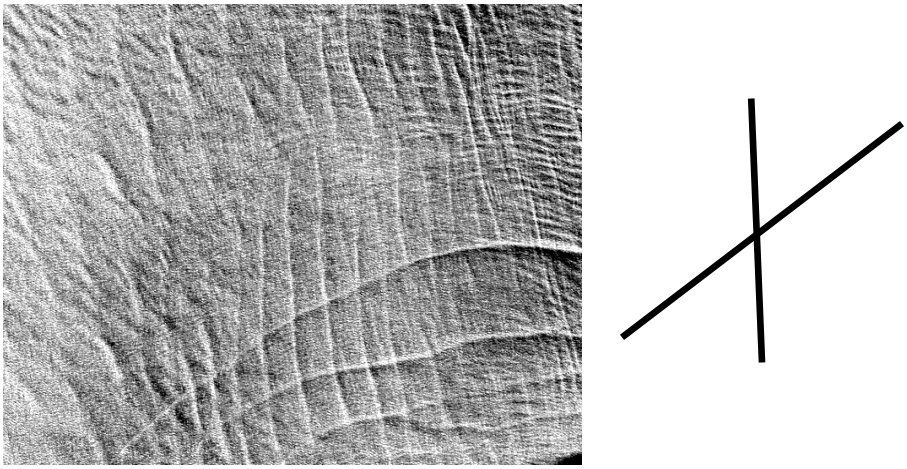

Figure C.2. Same as Figure C.1 for an internal wave interaction pattern observed in a SPOT-4 HRV-PAN image taken on July 30, 2006.

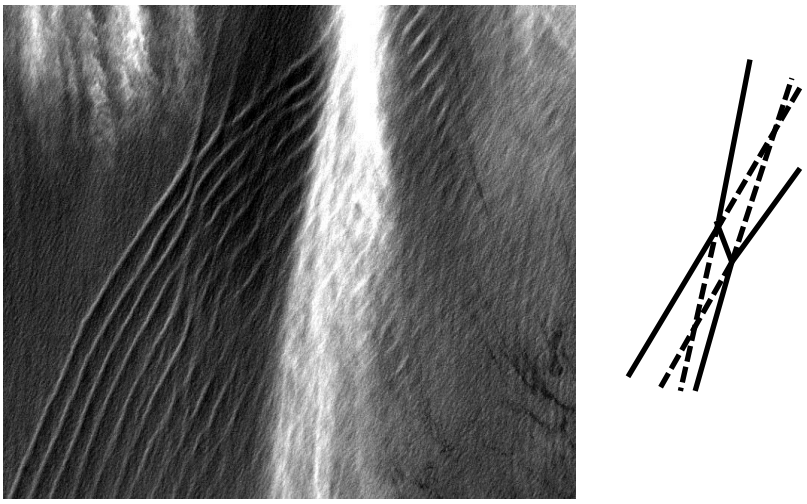

Figure C.3. Same as Figure C.1 for an internal wave interaction pattern observed in a SPOT-4 HRV-PAN image taken on July 31, 2006.

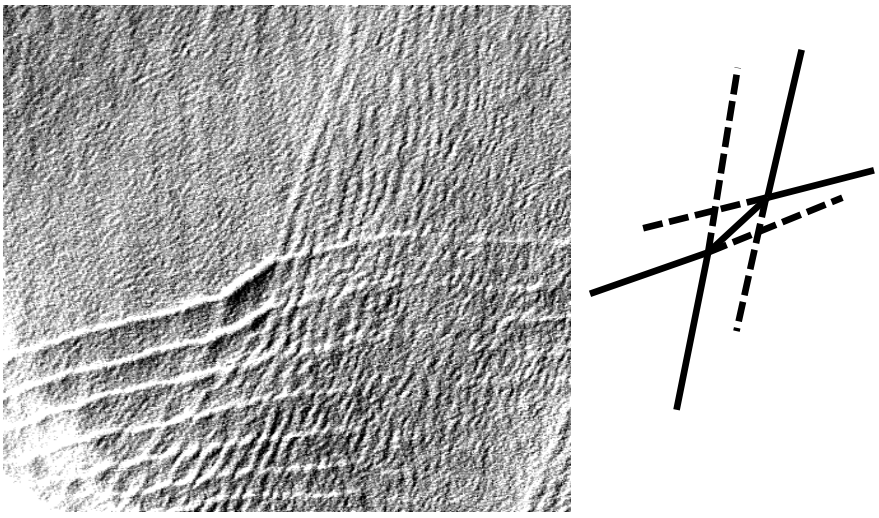

Figure C.4. Same as Figure C.1 for an internal wave interaction pattern observed in a SPOT-4 HRV-PAN image taken on July 31, 2006.

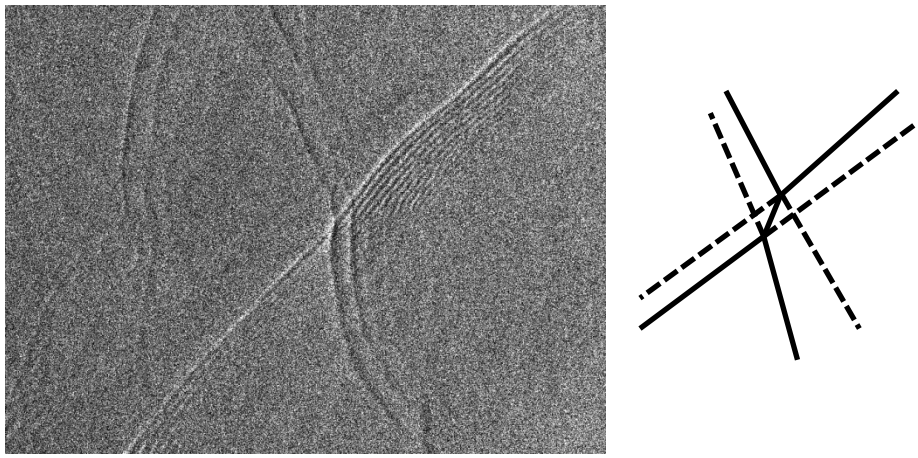

Figure C.5. Same as Figure C.1 for an internal wave interaction pattern observed in a RADARSAT-1 SAR image taken on August 08, 2006.

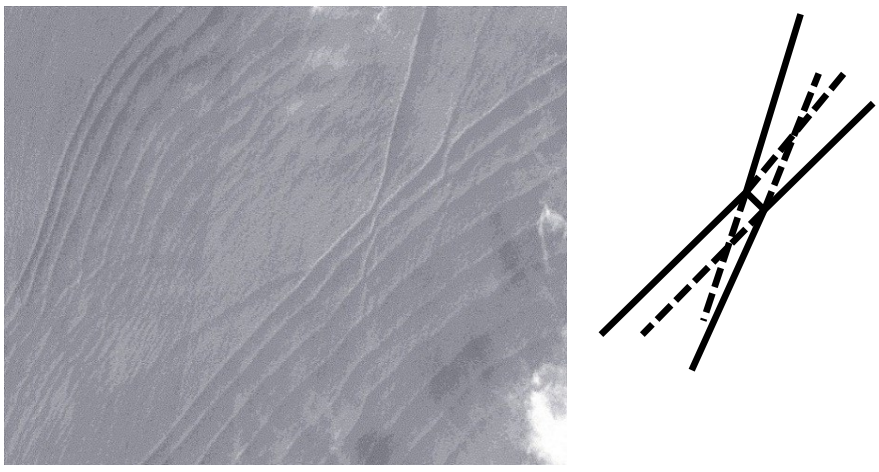

Figure C.6. Same as Figure C.1 for an internal wave interaction pattern observed in a SPOT-4 HRV-PAN image taken on August 16, 2006.

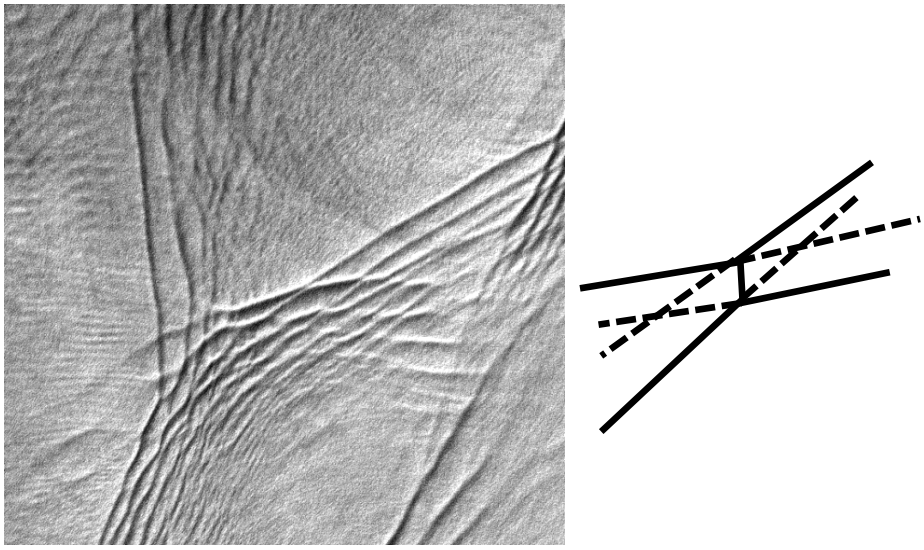

Figure C.7. Same as Figure C.1 for an internal wave interaction pattern observed in a SPOT-2 HRV-PAN image taken on August 17, 2006.

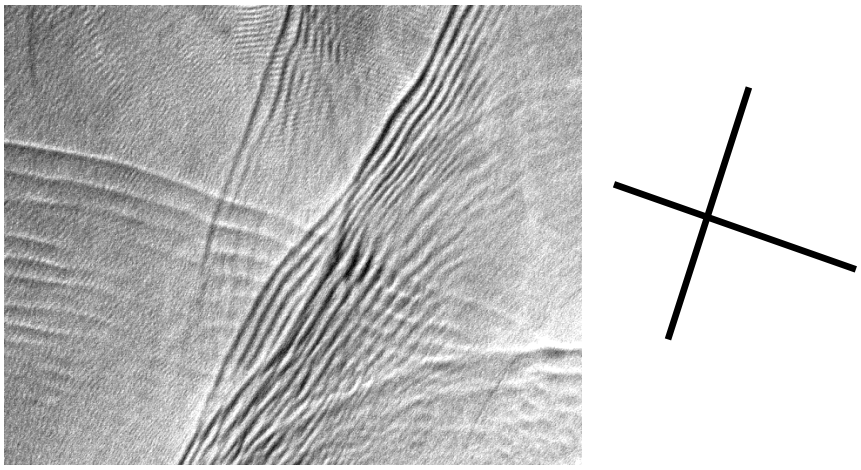

Figure C.8. Same as Figure C.1 for an internal wave interaction pattern observed in a SPOT-2 HRV-PAN image taken on August 17, 2006.

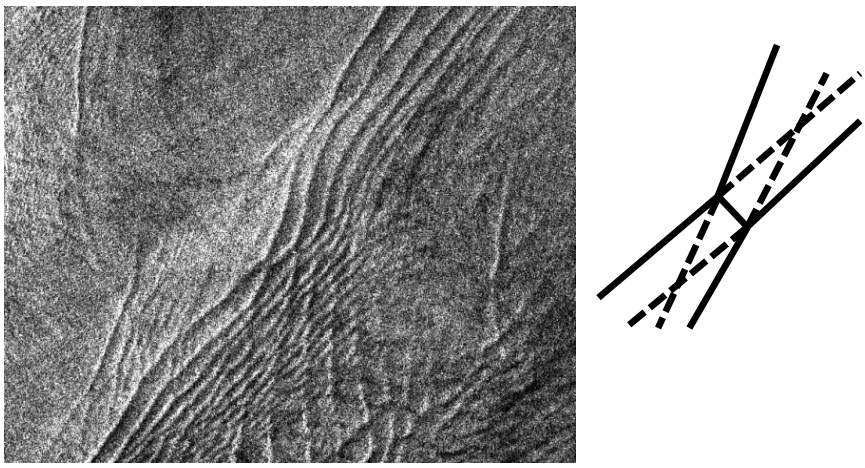

Figure C.9. Same as Figure C.1 for an internal wave interaction pattern observed in a RADARSAT-1 SAR image observed on August 22, 2006.

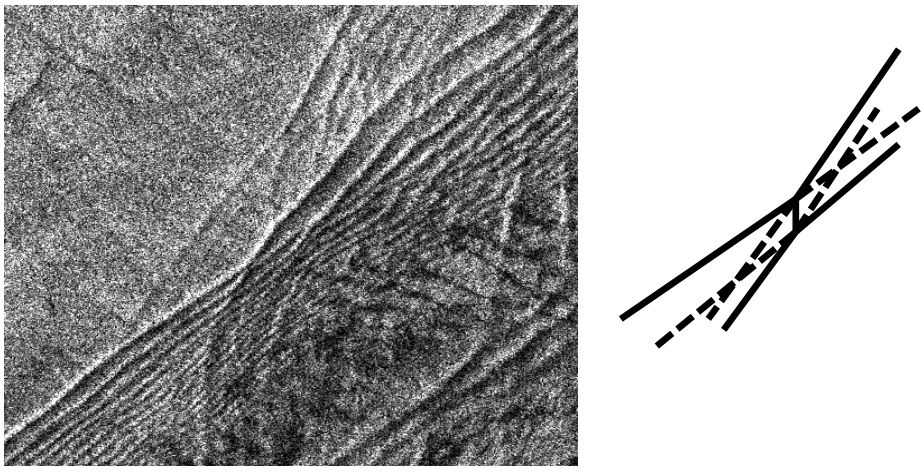

Figure C.10. Same as Figure C.1 for an internal wave interaction pattern observed in a RADARSAT-1 SAR image observed on August 22, 2006.

Table C.1. Interaction patterns observed with the characteristics listed fall into four types (1: Mach interaction; 2: Regular interaction with prominent positive phase shifts and an amplitude decrease in the interaction zone; 3: Regular interaction with prominent negative phase shifts and an amplitude increase in the interaction zone; 4: wave interaction without prominent phase shifts)

ID	Date	Image	Type	ψ	ψ_p	$\eta_{1,2p}$	η_i
Fig C.1	Jul 14	ENVISAT	3	53°	39°	same	stronger
Fig C.2	Jul 30	SPOT-4	4			same	na
Fig C.3	Jul 31	SPOT-4	3	62°	70°	same	stronger
Fig C.4	Jul 31	SPOT-4	2	27°	22°	same	weaker
Fig C.5	Aug 08	RADARSAT-1	3	68°	62°	same	stronger
Fig C.6	Aug 16	SPOT-4	2	32°	28°	same	weaker
Fig C.7	Aug 17	SPOT-2	2	15°	25°	same	weaker
Fig C.8	Aug 17	SPOT-2	4			same	na
Fig C.9	Aug 22	RADARSAT-1	2	25°	31°	same	weaker
Fig C.10	Aug 22	RADARSAT-1	2	18°	15°	same	weaker

REFERENCE

Alpers, W., 1985. Theory of radar imaging of internal waves. *Nature*, 314, 245–247.

Anctil, F., M. A. Donelan, W. M. Drennan, and H. C. Graber, 1994. Eddy correlations measurements of air-sea fluxes from a discus buoy. *J. Atmos. Oceanic Technol.*, 11, 1144–1150.

Apel, J. R., et al., 1997. An overview of the 1995 SWARM shallow water internal wave acoustic scattering experiment. *IEEE J. Oceanic Eng.*, 22, 465–500.

Apel, J. R., and C. R. Jackson, 2004. Synthetic Aperture Radar Marine Users Manual. Washington, DC: NOAA (2004) M.

Araujo, I. B., J. C. B. da Silva, S. A. Ermakov, and I. S. Robinson, 2002. On the role of wind direction in ERS SAR signatures of internal waves on the Iberian shelf. *J. Atmos. Ocean Sci.*, 8, (4), 269–281.

Azevedo, A., J. C. B. da Silva, and A. L. New, 2006. On the generation and propagation of internal solitary waves in the southern Bay of Biscay. *Deep-sea Res. I*, vol. 53, pp. 927–941.

Benjamin, T. B., 1966. Internal waves of finite amplitude and permanent form. *J. Fluid Mech.*, 25, 241–270.

Benney, D. J., 1966. Long non-linear waves in fluid flows. *J. Math. Phys.*, 45, 52–63.

Bogucki, D., T. Dickey, and L. G. Redekopp, 1997. Sediment resuspension and mixing by resonantly generated internal solitary waves. *J. Phys. Oceanogr.*, 27, 1181–1196.

Brandt, P., R. Romeiser, and A. Rubino, 1999. On the determination of characteristics of the interior ocean dynamics from radar signatures of internal solitary waves. *J. Geophys. Res.*, vol. 104, no. C12, pp. 30039–30047.

Caruso, C. M., and H. C. Graber, 2006. NLIWI Mid-Atlantic Bight Satellite Data Summary (unpublished).

Chang, M. H., R. C. Lien, Y. J. Yang, T. Y. Tang, and J. Wang, 2008. A composite view of surface signatures and interior properties of nonlinear internal waves: Observations and applications. *J. Atmos. Oceanic Technol.*, vol. 25, no. 7, pp. 1218–1227.

Chen, C. Y., and J. R. C. Hsu, 2005. Interaction between internal waves and a permeable seabed. *Ocean Eng.*, 32 (5–6), 587–621.

Chen, C. Y., J. R. Hsu, H. H. Chen, C. F. Kuo, and M. H. Cheng, 2007. Laboratory observations on internal solitary wave evolution on steep and inverse uniform slopes. *Ocean Eng.*, 34 (1), 157–170.

Chen, C. Y., 2007. An experimental study of stratified mixing caused by internal solitary waves in a two-layered fluid system over variable seabed topography. *Ocean Eng.*, 34 (14–15), 1995–2008.

Chen, G. Y., C. T. Liu, Y. H. Wang, and M. K. Hsu, 2011. Interaction and generation of long-crested internal solitary waves in the South China Sea. *J. Geophys. Res.*, 116, C06013, 2011.

Chin, T. M., R. F. Milliff, and W. G. Large, 1998. Basin-scale, high-wavenumber sea surface wind fields from a multiresolution analysis of scatterometer data. *J. Atmos. Oceanic Technol.*, 15, 741–763.

Choi, W. and R. Camassa, 1999. Fully nonlinear internal waves in two-fluid system. *J. Fluid Mech.*, 396, 1–36.

da Sliva, J. C. B., S. A. Ermakov, I. S. Robinson, D. R. G. Jeans, and S. V. Kijashko, 1998. Role of surface films in ERS SAR signatures of internal waves on the shelf, 1: Short-period internal waves. *J. Geophys. Res.*, vol. 103, pp. 8009–8031.

da Silva, J. C. B., A. L. New, and A. Azevedo, 2007. On the role of SAR for observing Local Generation of internal solitary waves off the Iberian Peninsula. *Can. J. Remote Sens.*, vol. 33, no. 5, pp. 388–403.

da Silva, J. C. B., and K. R. Helfrich, 2008. Synthetic aperture radar observations of resonantly generated internal solitary waves at Race Point Channel (Cape Cod). *J. Geophys. Res.*, vol. 113, C11016.

da Silva, J. C. B., A. L. New, and J. M. Magalhaes, 2009. Internal solitary waves in the Mozambique Channel: Observations and interpretation. *J. Geophys. Res.*, vol. 114, C05001.

da Silva, J. C. B., A. L. New, and J. M. Magalhaes. 2011. On the structure and propagation of internal solitary waves generated at the Mascarene Plateau in the Indian Ocean. *Deep-Sea Res. I*, 58:229–240.

Dokken, S. T., R. Olsen, T. Wahl, and M. V. Tantillo, 2001. Identification and characterization of internal waves in SAR images along the coast of Norway. *Geophys. Res. Lett.*, vol. 28, no. 14, pp. 2803–2806.

Grimshaw, R., 2002. Internal solitary waves. Proceedings of the International Conference dedicated to the 100th anniversary of A.A. Andronov; Progress in Nonlinear Science, Volume II, Frontiers of Nonlinear Physics, ed. A.G. Litvak, Inst. Applied Physics, Nizhny Novgorod, 139–153.

Grimshaw, R. and Y. Zhu, 1994. Oblique interactions between internal solitary waves. *Stud. Appl. Math.*, 92, 249–270.

Grue, J., A. Jensen, P. Rusas, and J. Sveen, 1999. Properties of large-amplitude internal waves. *J. Fluid Mech.*, 380, 257–278.

Hammack, J., D. Mccallister, N. Scheffner, and H. Segur, 1995. Two dimensional periodic waves in shallow water. Part 2. Asymmetric waves. *J. Fluid Mech.*, 285, 95–122.

Helfrich, K. R. and W. K. Melville, 2006. Long nonlinear internal waves. *Ann. Review Fluid Mech.*, 38, 395–425.

Holligan, P. M., R. D. Pingree, and G. T. Mardell, 1985. Oceanic solitons, nutrient pulses and phytoplankton growth. *Nature*, 314: 348–350.

Holloway, P. E., E. Pelinovsky, T. Talipova, and B. Barnes, 1997. A nonlinear model of internal tide transformation on the Australian North West Shelf. *J. Phys. Oceanogr.*, 27, 871–893.

Hsu, M. K., A. K. Liu, and C. Liu, 2000. A study of internal waves in the China Seas and Yellow Sea using SAR. *Cont. Shelf Res.*, 20, 389–410.

Irish, J.D., J. F. Lynch, J. N. Kemp, T. F. Duda, and A. E. Newhall, 2004. A moored array for measuring internal solitary waves during shallow water 06. *Oceans Conference Record (IEEE)*, art. no. 4449170.

Jackson, C., 2007. Internal wave detection using the Moderate Resolution Imaging Spectroradiometer (MODIS). *J. Geophys. Res.*, 112, C11012.

Jackson, C., and W. Alpers, 2010. The role of the critical angle in brightness reversals on sunglint images of the sea surface. *J. Geophys. Res.,* 115, C09019.

Joseph, R. J., 1977. Solitary waves in finite depth fluid. *J. Phys. A: Math. Gen.*, 10(12), L225–L227.

Killworth, P., 1998. Something stirs in the deep. *Nature*, 396(24/31), 720–721.

Klein, L. A., and C. T. Swift, 1977. An improved model for the dielectric constant of sea water at microwave frequencies. *IEEE Trans. Antennas Propag.*, 25, 105–111.

Kubota, T., D. R. S. Ko, and L. D. Dobbs, 1978. Weakly-nonlinear, long internal gravity waves in stratified fluids of finite depth. *J. Hydronautics*, 12, 157.

Li, H., Y. He, T. Du, and H. Shen, 2006. Effects of winds on internal wave synthetic aperture radar images. in *Proc. IGARSS*, pp. 1319–1322.

Li, X., P. Clemente-Colon, and K. Friedman, 2000. Estimating oceanic mixed layer depth from internal wave evolution observed from RADARSAT-1 SAR. *Johns Hopkins University Applied Physics Lab Technical Digest*, 21(1), 130–135.

Li, X., Z. Zhao, and W. G. Pichel, 2008. Internal solitary waves in the northwestern South China Sea inferred from satellite images. *Geophys. Res. Lett.*, vol. 35, L13605.

Liu, A. K., 1988. Analysis of nonlinear internal waves in the New York Bight. *J. Geophys. Res.*, 93, 12317–12329.

Liu, A. K., Y. S. Chang, M. K. Hsu, and N. K. Liang, 1998. Evolution of nonlinear internal waves in the East and South China Seas. *J. Geophys. Res.*, vol. 103, no. C4, pp. 7995–8008.

Lund, B., H. C. Graber, J. Xue, and R. Romeiser, 2013. Analysis of internal wave signatures in marine radar data. *IEEE Trans. Geosci. Remote Sens.*, to be published.

Matsuno, Y., 1998. Oblique interaction of interfacial solitary waves in a two-layer deep fluid. *Proc. R. Soc. London A*, 454, 835–856.

Michallet, H., E. Barthelemy, 1998. Experimental study of interfacial solitary waves. *J. Fluid Mech*., 366:159–77.

Miles, J. W., 1977a. Obliquely interacting solitary waves. *J. Fluid Mech.*, 79, pp. 157–169.

Miles, J. W., 1977b. Resonantly interacting solitary waves. *J. Fluid Mech.*, 79, pp. 171–179.

Mitnik, L., W. Alpers, K. S. Chen, and A. J. Chen, 2000. Manifestation of internal solitary waves on ERS SAR and SPOT images: similarities and differences. in *Proc. IGARSS,* pp. 1857–1859.

Mitnik, L. M., and V. A. Dubina, 2007. Spatial-temporal distribution and characteristics of internal waves in the Okhotsk and Japan seas studied by ERS-1/2 SAR and ENVISAT ASAR. *European Space Agency*, SP-636.

Miyata, M., 1985. An internal solitary wave of large amplitude. *La Mer*, 23:43–48.

Miyata, M., 1988. Long internal waves of large amplitude. In *Nonlinear Water Waves*, *IUTAM Symp.*, *Tokyo 1987*, ed. K Horikawa, H Maruo, pp. 399–406. Berlin: Springer-Verlag. 466 pp.

New, A. L., and J. C. B. da Silva, 2002. Remote sensing evidence for the local generation of internal soliton packets in the Central Bay of Biscay. *Deep-Sea Res. I*, 49:915–34.

Newhall, A. E., T. F. Duda, K. Von der Heydt, J. D. Irish, J. N. Kempt, S. A. Lerner, S. P. Liberatore, Y. T. Lin, J. F. Lynch, A. R. Maffei, A. K. Morozov, A. Shmelev, C. J. Sellers, and W. E. Witzell, 2007. Acoustic and oceanographic observations and configuration information for the WHOI moorings from the SW06 experiment. Woods Hole Oceanographic Institution Technical Report WHOI-2007-04, pp. 117.

Oikawa, M., 1984. On the weak interactions of the Benjamin-Ono solitons. *Bull. Res. Inst. Appl. Mech. Kyushu Univ.*, 60, 467–472.

Ono, H., 1975. Algebraic solitary waves in stratified fluids. *J. Phys. Soc. Japan.*, 39, 1082–1091.

Orr, M. H., and P. C. Mignerey, 2003. Nonlinear internal waves in the South China Sea: Observation of the conversion of depression internal waves to elevation internal waves. *J. Geophys. Res.*108 (C3):3064.

Osborne, A. R., and T. L. Burch, 1980. Internal solitons in the Andaman Sea. *Science*, 208, 451–460.

Ouyang, Y., J. S. Chong, Y. R. Wu, and M. H. Zhu, 2011. Simulation studies of internal waves in SAR images under different SAR and wind field conditions. *IEEE Trans. Geosci. Remote Sens.*, vol. 49, no. 5, pp. 1734–1743.

Pan, J., D. A. Jay, and P. M. Orton, 2007. Analyses of internal solitary waves generated at the Columbia River plume front using SAR imagery. *J. Geophys. Res.,* 112, C07014.

Pan, J., and D. A. Jay, 2008. Dynamic characteristics and horizontal transports of internal solitons generated at the Columbia River plume front. *Cont. Shelf Res.*, vol. 29, no. 1, pp. 252–262.

Pan, J., and D. A. Jay, 2009. Effects of ambient velocity shear on nonlinear internal wave associated mixing at the Columbia River plume front. *J. Geophys. Res.*, 114, C00B07.

Peterson, P., and E. van Groesen, 2000. A direct and inverse problem for wave crests modeled by interactions of two solitons. *Physica D*, 141, 316–332.

Peterson, P., and E. van Groesen, 2001. Sensitivity of the inverse wave crest problem. *Wave Motion*, 34, 391–399.

Peterson, P., T. Soomere, J. Engelbrecht, and E. van Groesen, 2003. Soliton interaction as a possible model for extreme waves in shallow water. *Nonlin. Processes in Geophys.*, 10, pp. 503–510.

Porter, D. L., and D. R. Thomson, 1999. Continental shelf parameters inferred from SAR internal wave observations *J. Atmos. Oceanic Technol.*, 16, 475–487.

Porubov, A. V., H. Tsuji, I. V. Lavrenov, and M. Oikawa, 2005. Formation of the rogue wave due to non-linear two-dimensional waves interaction. *Wave Motion*, 42(3), 202–210.

Ramos, R. J., B. Lund, and H. C. Graber, 2009. Determination of internal wave properties from X-band radar observations. *Ocean Eng.*, vol. 36, no. 14, pp. 1039–1047.

Romeiser, R., W. Alpers, and V. Wismann, 1997. An improved composite surface model for the radar backscattering cross section of the ocean surface, 1. Theory of the model and optimization/validation by scatterometer data. *J. Geophys. Res.*, vol. 102, pp. 25237–25250.

Romeiser, R., and W. Alpers, 1997. An improved composite surface model for the radar backscattering cross section of the ocean surface, 2. Model response to surface roughness variations and the radar imaging of underwater bottom topography. *J. Geophys. Res.*, vol. 102, pp. 25251–25267.

Saxton, J. A., and J. A. Lane, 1952. Electrical properties of sea water. *Wirel. Eng.*, 291, 269–275.

Shroyer, E. L., J. N. Moum, and J. D. Nash, 2009. Observations of polarity reversal in shoaling nonlinear internal waves. *J. Phys. Oceanogr.*, vol. 39, pp. 691–701.

Shroyer, E. L., J. N. Moum, and J. D. Nash, 2011. Nonlinear internal waves over New Jersey's continental shelf. *J. Geophys. Res.*, vol. 116, C03022.

Small, J., Z. Hallock, G. Pavey, and J. Scott, 1999. Observations of large amplitude internal waves at the Malin shelf-edge during SESAME 1995. *Cont. Shelf Res.*, 19, 1389–1436.

Stanton, T. P., and L. A. Ostrovsky, 1998. Observations of highly nonlinear internal solitons over the continental shelf. *Geophys. Res. Lett.*, vol. 25, no. 14, pp. 2695–2698.

Tanaka, M., 1993. Mach reflection of a large-amplitude solitary wave. *J. Fluid Mech.*, 248, pp. 637–661.

Tsuji, H and M. Oikawa, 2007. Oblique interaction of solitons in an extended Kadomtsev-Petviashvili equation. *J. Phys. Soc. Japan*, 76, 84401–8.

Valenzuela, G. R, 1978. Theories for the interaction of electromagnetic and oceanic waves- A review. *Bound.-Layer Meteor.*, 13:61–85.

Vlasenko, V., P. Brandt, and A. Rubino, 2000. Structure of large-amplitude internal solitary waves. *J. Phys. Oceanogr.*, 30, pp. 2172–2185.

Wang, C., and R. Pawlowicz, 2011. Propagation speeds of strongly nonlinear near surface internal waves in the Strait of Georgia. *J. Geophys. Res.*, 116, C10021.

Wang, C., and R. Pawlowicz, 2012. Oblique wave-wave interactions of nonlinear near-surface internal waves in the Strait of Georgia. *J. Geophys. Res.*, 117, C06031.

Watson, G., and I. S. Robinson, 1990. A study of internal wave propagation in the Strait of Gibraltar using shore-based marine radar images. *J. Phys. Oceanogr.*, 20(3):374–395.

Xue, J, 2010. Internal Wave Signature Analyses with Synthetic Aperture Radar Images in the Mid-Atlantic Bight. M.S. Thesis, University of Miami, Miami, FL.

Xue, J., B. Lund, H. C. Graber, and R. Romeiser, 2012. A case study of internal wave-wave interaction during the shallow water 2006 experiment. in *Proc. IGARSS*, pp. 2845–2848.

Xue**,** J., H. C. Graber, B. Lund, and R. Romeiser, 2013a. Amplitudes estimation of large internal solitary waves in the Mid-Atlantic Bight using synthetic aperture radar and marine X-band radar images. *IEEE Trans. Geosci. Remote Sens.*, vol. 51, no. 6, pp. 3250–3258.

Xue**,** J., H. C. Graber, R. Romeiser, and B. Lund, 2013b. Understanding internal wave-wave interaction patterns observed in satellite images of the Mid-Atlantic Bight. *IEEE Trans. Geosci. Remote Sens.*, to be published.

Yang, J. S., W. G. Huang, C. B. Zhou, and Q. M. Xiao, 2001. Simulation study on optimal conditions for internal wave observation by SAR. in *Proc. IGARSS*, pp. 3288–3290.

Yang, j. S., W. G. Huang, C. B. Zhou, M. K. Hsu, and Q. M. Xiao, 2003. Nonlinear internal wave amplitude remote sensing from SAR imagery. in *Proc. SPIE*, 4892, 450.

Yuan, Y., 1997. Representation of high frequency spectra of ocean waves and the basis for analyzing SAR images. *Chin. J. Oceanol. Limnol.*, 28, suppl., 1–5.

Zha, G., Y. He, T. Yu, Q. He, and H. Shen, 2012. The force exerted on a cylindrical pile by ocean internal waves derived from nautical X-band radar observations and in-situ buoyancy frequency data. *Ocean Eng.*, vol. 41, no. 0, pp. 13–20.

Zhao, Z., V. Klemas, Q. Zheng, and X. H. Yan, 2004. Remote sensing evidence for baroclinic tide origin of internal solitary waves in the northeastern South China Sea. *Geophys. Res. Lett.*, vol. 31, L06302.

Zhao, Z., V. Klemas, Q. Zheng, X. Li, and X. H. Yan, 2004. Estimating parameters of a two-layer stratified ocean from polarity conversion of internal solitary waves observed in satellite SAR images. *Remote Sens. Environ.*, 92, 276–287.

Zheng, Q., R. D. Susanto, C. R. Ho, Y. T. Song, and Q. Xu, 2007. Statistical and dynamical analyses of generation mechanisms of solitary internal waves in the northern South China Sea. *J. Geophys. Res.*, vol. 112, C03021.

Zheng, Q., Y. Yuan, V. Klemas, and X. H. Yan, 2001. Theoretical expression for an ocean internal soliton synthetic aperture radar image and determination of the soliton characteristic half width. *J. Geophys. Res.*, vol. 106, no. C11, pp. 31415–31423.

Zheng, Q., X. H., Yan, and V. Klemas, 1993. Statistical and dynamical analysis of internal waves on the continental shelf of the Middle Atlantic Bight from space shuttle photographs. *J. Geophys. Res.*, 98, 8495–8504.